

Fiber Amplifiers at $1.5\ \mu\text{m}$ for Gravitational Wave Detectors

Power Scaling, Gain Dynamics, and Pump Sources

Von der Fakultät für Mathematik und Physik
der Gottfried Wilhelm Leibniz Universität Hannover
zur Erlangung des Grades

Doktor der Naturwissenschaften
Dr. rer. nat.

genehmigte Dissertation

von
Dipl.-Phys. Michael Steinke
geboren am 08.03.1985 in Gehrden

2015

Referent: Prof. Dr. Uwe Morgner, Leibniz Universität Hannover
Korreferent: Prof. Dr. Karsten Danzmann, Leibniz Universität Hannover
Tag der Promotion: 10.12.2015

Kurzzusammenfassung

Im Rahmen der vorliegenden Arbeit wurden verschiedene Aspekte von Er^{3+} -dotierten und $\text{Er}^{3+}:\text{Yb}^{3+}$ -kodotierten Faserverstärkern untersucht, insbesondere in Hinblick auf einen Einsatz in der nächsten Generation von interferometrischen Gravitationswellendetektoren (*engl.*: gravitational wave detectors, GWDs). In Bezug auf zukünftige GWDs wird der Einsatz von kryogen gekühltem kristallinen Silizium als Substrat für die optischen Elemente diskutiert, da hierdurch das thermische Rauschen verringert bzw. die Empfindlichkeit der Detektoren gesteigert werden kann. Dies erfordert jedoch die Entwicklung von Hochleistungslasern bei einer Wellenlänge von $1,5\ \mu\text{m}$ mit einer Linienbreite von einigen Kilohertz und einer sehr guten Strahlqualität bzw. einem hohen Überlapp mit einer TEM_{00} Mode.

$\text{Er}^{3+}:\text{Yb}^{3+}$ -kodotierte Fasern mit einem großen Modenfelddurchmesser (*engl.*: large mode-area, LMA) waren bisher entweder limitiert in Bezug auf die zu erreichende Ausgangsleistung oder in Bezug auf die Strahlqualität. Im Rahmen dieser Arbeit wurde eine neuartige $\text{Er}^{3+}:\text{Yb}^{3+}$ -kodotierte LMA-Faser untersucht und es konnte gezeigt werden, dass sich diese Faser sehr gut für den Einsatz in einrequenten Faserverstärkern eignet, da ein TEM_{00} Anteil von über 90 % und eine maximale Ausgangsleistung von 61 W erreicht werden konnte. Des Weiteren konnte gezeigt werden, dass auch bei solch hohen Ausgangsleistungen eine zweite Laserquelle bei einer Wellenlänge von $1,0\ \mu\text{m}$ genutzt werden kann, um parasitäre Laserprozesse zu unterdrücken. Zusätzlich wurde gezeigt, dass das Strahlprofil einer neuartigen passiven leakage channel fiber (LCF) mit einem Kerndurchmesser von ca. $50\ \mu\text{m}$ einen TEM_{00} Anteil von mehr als 97,5 % aufweist. Somit eignen sich LCFs hervorragend als passive Übertragungsfasern in GWDs.

Aus verschiedensten Gründen muss das dynamische Verhalten von Laserquellen in GWDs verstanden sein. Im Rahmen dieser Arbeit wurde erstmals die frequenzabhängige Verstärkung von Signal- und Pumpleistungsrauschen eines $\text{Er}^{3+}:\text{Yb}^{3+}$ -kodotierten Faserverstärkers mit einer numerischen Simulation detailliert untersucht. Die entsprechenden Ergebnisse weisen eine gute qualitative Übereinstimmung mit experimentell bestimmten Übertragungsfunktionen auf. Des Weiteren wurden erstmals die durch Pumpleistungsfuktuationen induzierten Änderungen des Brechungsindex eines $\text{Er}^{3+}:\text{Yb}^{3+}$ -kodotierten Faserverstärkers mit Hilfe eines faserbasierten Mach-Zehnder-Interferometers untersucht.

Insbesondere mit Hinblick auf die speziellen Anforderungen von GWDs an die Laserquelle sind kaskadierte Raman-Faserlaser (*engl.*: cascaded Raman fiber lasers, CRFLs) bei 1480 nm vielversprechende Pump Laser für Er^{3+} -dotierte Faserverstärker. Deshalb wurden einige wichtige Aspekte von solchen CRFLs näher untersucht und Optimierungen erarbeitet. Des Weiteren konnte erstmals experimentell gezeigt werden, dass eine zusätzliche Stokes-Ordnung genutzt werden kann, um eine passive Rauschunterdrückung von Pumpe zu Signal zu erreichen. Aufgrund von numerischen Ergebnissen sollte diese passive Rauschunterdrückung auch in CRFLs bei 1480 nm realisierbar sein, so dass solche Lasersysteme als Pumpquellen für rauscharme Er^{3+} -dotierte Faserverstärker in zukünftigen GWDs genutzt werden könnten.

Schlagwörter: Erbium Faserverstärker, einrequent, Gravitationswellendetektoren

Abstract

The main topic of this thesis was the investigation of several important aspects related to Er^{3+} -doped and $\text{Er}^{3+}:\text{Yb}^{3+}$ -codoped fiber amplifiers at $1.5\ \mu\text{m}$ for applications in the next generation of interferometric gravitational wave detectors (GWDs). In the context of these future GWDs it is discussed to utilize crystalline silicon as substrate material for the optical elements within the interferometer since this will allow for cryogenic cooling schemes and a corresponding reduction of the thermal noise level, i.e. an increased detector sensitivity. However, this will also require high power laser sources at $1.5\ \mu\text{m}$ with a linewidth in the order of some kilohertz, i.e. single-frequency operation, and an excellent beam quality, i.e. a high TEM_{00} mode content.

Large mode-area (LMA) fibers allow to increase the threshold of nonlinear effects in fiber amplifiers. So far, $\text{Er}^{3+}:\text{Yb}^{3+}$ -codoped LMA fibers were lacking either a good beam quality or a sufficient power handling capability. In the frame of this thesis a novel $\text{Er}^{3+}:\text{Yb}^{3+}$ -codoped triple-clad LMA fiber was investigated and it was shown that this fiber is a promising candidate for single-frequency fiber amplifiers at $1.5\ \mu\text{m}$ as it provided a good TEM_{00} mode content of more than 90% and a maximum output power of 61 W. Furthermore, it was proven that the co-seeding method is a viable approach to suppress parasitic lasing at $1.0\ \mu\text{m}$, even at such high output power levels. In addition, it was shown that a particular passive leakage channel fiber (LCF) with a core diameter of around $50\ \mu\text{m}$ provides an excellent TEM_{00} mode content of more than 97.5%. Thus, the LCF concept is a promising candidate for passive delivery fibers in GWDs.

Understanding the temporal dynamics of the laser source in a GWD is important for several reasons. Thus, the gain dynamics of $\text{Er}^{3+}:\text{Yb}^{3+}$ -codoped fiber amplifiers were studied in the frame of this thesis for the first time. As a complete analytical solution of the problem does not exist, a simulation was developed and the transfer functions of an exemplary $\text{Er}^{3+}:\text{Yb}^{3+}$ -codoped fiber amplifier were studied numerically in detail. Furthermore, the corresponding results provide good qualitative agreement with experimentally obtained transfer functions. In addition, the pump power modulation induced refractive index changes in an exemplary $\text{Er}^{3+}:\text{Yb}^{3+}$ -codoped fiber amplifier were analyzed with a fiber-based Mach-Zehnder interferometer for the first time.

Cascaded Raman fiber lasers (CRFLs) at 1480 nm are promising pump sources for Er^{3+} -doped fiber amplifiers, in particular with respect to the special requirements of GWDs. Some important aspects of such CRFLs were studied in the frame of this thesis and optimization strategies were investigated. Furthermore, it was proven experimentally that an additional Stokes order can be used to achieve a passive pump-to-Stokes noise transfer suppression. As a numerical simulation predicts that the passive noise suppression scheme can also be applied in CRFLs at 1480 nm, such laser systems could act as low-noise pump sources for low-noise Er^{3+} -doped fiber amplifiers in next-generation GWDs.

Key words: erbium fiber amplifier, single-frequency, gravitational wave detectors

Contents

1	Introduction	1
2	Laser Sources for Gravitational Wave Detectors	3
3	Fundamentals of Fiber Lasers and Amplifiers	7
3.1	Waveguide Characteristics of Optical Fibers	7
3.2	Active Rare-Earth Doped Fibers	10
3.2.1	Er ³⁺ -Doping	12
3.2.2	Er ³⁺ :Yb ³⁺ -Codoping	14
3.3	Nonlinear Processes in Fibers	15
3.3.1	Stimulated Raman Scattering	16
3.3.2	Stimulated Brillouin Scattering	18
3.3.3	Four-Wave Mixing	19
4	Power Scaling of Er³⁺:Yb³⁺-Codoped Fiber Amplifiers	21
4.1	Co-Seeded Large Mode-Area Er ³⁺ :Yb ³⁺ -Codoped Fiber Amplifier	22
4.1.1	Fiber Design and Experimental Setup	25
4.1.2	Influence of the Co-Seeding Parameters	27
4.1.3	Power Scaling Experiments	29
4.1.4	Beam Quality Measurements	30
4.1.5	Comparison and Conclusion	32
4.2	Passive Leakage Channel Fiber	33
4.2.1	Fiber Design	35
4.2.2	Beam Quality Measurements at 1.0 μm and 1.5 μm	36
4.2.3	Conclusion	38
4.3	Beam Quality Measurements on Few-Mode Large Mode Area Fibers	38

5 Gain Dynamics of Er³⁺:Yb³⁺-Codoped Fiber Amplifiers	41
5.1 Transfer Functions of Pump and Seed Power Noise	42
5.1.1 Analytical Model	45
5.1.2 Numerical Investigations	50
5.1.3 Experimental Results	54
5.1.4 Conclusion	58
5.2 Optical Phase Shift	59
5.2.1 Experimental Setup	62
5.2.2 Results	63
5.2.3 Conclusion	65
6 Single-Mode Pump Source for Er³⁺-Doped Fiber Amplifiers	67
6.1 Cascaded Raman Fiber Laser at 1480 nm	69
6.1.1 Numerical Investigations	70
6.1.2 Experimental Results	75
6.1.3 Conclusion	78
6.2 Passive Pump-to-Stokes Noise-Transfer Suppression	79
6.2.1 Gain Dynamics in Raman Fiber Lasers	81
6.2.2 Raman Fiber Lasers with Parasitic Stokes Order	86
6.2.3 Conclusion	92
7 Conclusion	95
8 Outlook	99
Bibliography	103
Publications in Peer-Reviewed Journals	119
Publications in Conference Proceedings	121
Curriculum Vitae	123

Acronyms

Notation	Description
AOM	acousto-optic modulator
ASE	amplified spontaneous emission
BVP	boundary value problem
CBC	coherent beam combining
CCC	chirally-coupled-core
CRFL	cascaded Raman fiber laser
CW	continuous wave
DFB	distributed feedback
ET	Einstein Telescope
FBG	fiber Bragg grating
FWM	four-wave mixing
GWD	gravitational wave detector
KKR	Kramers–Kronig relation
LCF	leakage channel fiber
LMA	large mode-area
MCVD	modified chemical vapor deposition
MFC	multifilament core
MOPA	master oscillator power amplifier
NA	numerical aperture
NPRO	non-planar ring oscillator
PCF	photonic crystal fiber

Notation	Description
PDE	partial differential equation
PID	proportional-integral-derivative
RBW	resolution bandwidth
Re-LCF	resonantly enhanced leakage channel fiber
RIN	relative intensity noise
SBS	stimulated Brillouin scattering
SRS	stimulated Raman scattering
UV	ultraviolet
WDM	wavelength division multiplexer

CHAPTER 1

Introduction

Gravitational waves, i.e. wavelike ripples in the curvature of the spacetime, are a direct consequence of Einstein's theory of general relativity. In 1974 it was discovered that the specific variations of radio emissions from a pulsar, which is in a binary orbit with another neutron star, are indirectly related to gravitational waves that are emitted by the binary neutron star pair [Tay79]. Since then, comparable investigations of other binary pairs, e.g. a pair of black holes in a quasar [Val08], confirmed independently but still indirectly the existence of gravitational waves. However, as it is explained in detail in the following, direct measurements of gravitational waves will revolutionize the astronomy and our understanding of how the universe has evolved directly after the Big Bang.

A broad variety of antennas has been invented during the last centuries to study the universe throughout the electromagnetic spectrum, from radio telescopes such as the Atacama Large Millimeter/submillimeter Array (ALMA) in the Atacama desert of northern Chile to gamma-ray observatories in space, e.g. the Fermi Gamma-ray Space Telescope (FGST, formerly GLAST). However, as only around 5% of the matter in the universe is baryonic [Hin09], only an unsatisfying small amount of the universe can be studied by using these more or less traditional instruments. On the contrary, all matter in the universe interacts through the gravitational field. Therefore, gravitational waves are for example the only possible way to make direct observations of black holes or other hidden regions such as the interior of a supernova [Sch99]. In addition, as the early universe was opaque to electromagnetic radiation, the detection of primordial gravitational waves will allow to test inflationary models [Kra10]. Thus, once a reliable direct detection of gravitational waves is feasible, it will provide a new and amazing tool to probe the universe even back to its earliest moments.

As early as in the 1970s it was proposed to use laser-based large-scale Michelson

interferometers to directly detect gravitational waves because they induce a strain of the spacetime in one of the interferometer arms relative to the other that imprints via a phase shift between the laser fields a unique signature on the interferometer signal [Wei72]. Since then, corresponding technologies have evolved significantly and sufficiently sensitive detectors are technically feasible today. Therefore, amongst other detection concepts interferometric gravitational wave detectors (GWDs) are promising candidates for the first direct detection of gravitational waves as they provide the desired sensitivity in a relatively broad frequency band. Currently, interferometric GWDs operate at five different sites around the world: TAMA in Japan, GEO600 in Germany, LIGO at two sites in the USA, and Virgo in Italy [Rap10]. Most likely, the Japanese KAGRA detector will join this global network in the future [Aso13]. In particular the LIGO detectors and the Virgo detector are currently upgraded to their second generation by implementing some advanced techniques such as signal recycling or better seismic isolation [Aas15; Ace15]. Once finished, the detectors should be sensitive enough to detect the first gravitational waves. However, theoretical investigations predict that only a few massive astronomical events per year, e.g. merging pairs of black holes or neutron stars, will produce signals strong enough to be detected by the current generation of detectors [Pun10].

Therefore, an advanced third generation of interferometric GWDs is required in order to systematically probe the universe by a more sensitive detection of gravitational waves. The actual requirements for these next-generation GWDs with respect to the laser systems are not yet defined, but conceptual studies have been compiled. The Einstein Telescope (ET) assumes a xylophone configuration that incorporates two individual detectors with different sensitivity bands [Abe11]. In order to increase the sensitivity at low frequencies by a reduction of thermal noise, one of the detectors will utilize crystalline silicon as substrate material for the optical elements since it provides superior thermo-optical properties if cryogenically cooled. Currently, all GWDs operate at a laser wavelength of 1064 nm, but crystalline silicon is not transparent at this wavelength. Therefore, a change of the operation wavelength will be necessary. As the absorption, which leads to thermal noise, of crystalline silicon is minimal at around 1550 nm, corresponding laser sources at 1.5 μm are required. Note that ET's second detector will rely on conventional techniques, e.g. a laser source at 1.0 μm , and will be more sensitive at higher frequencies. Following a similar argumentation, further upgrades of the LIGO detectors are discussed and cryogenically cooled crystalline silicon substrates in combination with laser sources at 1.5 μm are one of the possible major features to increase the sensitivity of the detectors [LIG13]. Therefore, the development of suitable laser sources at a wavelength of 1.5 μm as well as 1.0 μm is a main concern regarding next-generation interferometric GWDs.

CHAPTER 2

Laser Sources for Gravitational Wave Detectors

As argued in the previous chapter, the spacetime strain induced by a gravitational wave is measured in an interferometric GWD as a differential phase shift between the laser fields in the arms of the interferometer. This detection method leads to some unique and sophisticated requirements on the laser source. As the current generation of GWDs is limited to the detection of quite rare astrophysical events, long-term data collection is necessary and a very stable and reliable laser source is required. In particular the frequency stability of the laser source can only be achieved with external locking schemes that require single-frequency operation, i.e. a laser linewidth in the order of some kilohertz. In addition, the sensitivity of GWDs is commonly increased by using resonant cavities in the interferometer arms. These cavities are designed such that they are resonant for a TEM_{00} mode and an external mode cleaner is used to filter out any higher order modes of the laser source. Therefore, a laser source with an excellent beam quality, i.e. a high TEM_{00} mode content, is required. Furthermore, the uncertainty of the arrival times of the individual photons at the detector, which is due to Heisenberg's uncertainty principle, imprints a corresponding noise on the interferometer signal. As this shot-noise scales inversely with the square root of the power of the laser source, high output power levels are required. In addition, as the accumulated phase shift, i.e. the sensitivity, in the interferometer scales inversely with the wavelength of the laser source, a short laser wavelength is preferred. At the time when the first generation of GWDs was proposed and designed, Nd^{3+} -doped solid-state lasers at 1064 nm were selected as laser sources because of the well understood solid-state laser technology that allowed for a satisfying trade-off between the aforementioned requirements.

So far, all laser sources that have been developed for GWDs utilize a single-frequency non-planar ring oscillator (NPRO) at 1064 nm with a good initial noise performance as

a master laser that is either amplified in a single-pass amplifier chain (master oscillator power amplifier (MOPA) approach) or injected to a high-power oscillator, i.e. the slave. The latter concept is denoted as injection locking and most commonly a Pound-Drever-Hall locking scheme is used to keep the slave resonant with the master. As the slave maintains the frequency stability of the master and because the power stability can be achieved with external stabilization techniques, these concepts are very attractive for laser systems in the context of GWDs. The state of the art laser system for GWDs is the laser system for the current advanced generation of LIGO [Win11]. It consists of an intermediate $\text{Nd}^{3+}:\text{YVO}_4$ amplifier in MOPA configuration [Fre07] that is seeded by a NPRO and then injection locked to a $\text{Nd}^{3+}:\text{YAG}$ ring oscillator. This system achieves a total continuous wave (CW) output power of 220 W (168 W in the TEM_{00} mode) and is externally stabilized to make the system suitable for advanced LIGO [Kwe12].

Theoretically, the injection locking scheme can be scaled further by increasing the number of crystals to achieve even higher output power levels. However, corresponding systems would become quite complex and most probably intolerably difficult to align. Indeed, single-pass amplifier systems in MOPA configuration might be easier to handle and it has been shown that a solid-state amplifier chain consisting of $\text{Nd}^{3+}:\text{YVO}_4$ and $\text{Nd}^{3+}:\text{YAG}$ can provide a performance similar to the advanced LIGO laser system [Bas12]. However, the complexity of such a system also grows with every amplifier stage and it is at least questionable if it would be suitable for next-generation GWDs.

Over the last decade the concept of single-frequency fiber amplifiers in MOPA configuration as laser sources for GWDs has gained a lot of attention as they are for example very compact and most basically alignment-free, in particular if compared to solid-state laser systems. Furthermore, the large surface-to-volume ratio of fibers allows for a quite simple thermal management and the beam quality is almost exclusively determined by the fiber geometry. In particular at 1064 nm it has been shown that an all-fiber Yb^{3+} -doped single-frequency fiber amplifier can provide a comparable performance as the advanced LIGO laser system, but with a reduced size and complexity [The12a]. Furthermore, a lot of work has been contributed to the power scaling of the TEM_{00} mode content in specialty Yb^{3+} -doped fibers [Kar12a; Kar13b], novel fiber components [The12b], the gain dynamics of Yb^{3+} -doped fiber amplifiers [Tün12b; Tün12c], and coherent beam combining schemes at 1064 nm [Tün12a; Tün11]. Thus, single-frequency Yb^{3+} -doped fiber amplifiers are actually very promising candidates as laser sources at 1.0 μm for next-generation GWDs. However, they also provide several challenges such as the recently heavily discussed and investigated modal instabilities [Zer14], which represent nowadays the most fundamental limitation regarding the power scaling of fiber amplifiers at 1.0 μm . Thus, quite some work

remains to be carried out before Yb^{3+} -doped single-frequency fiber amplifiers can fulfill the specifications that will be required by next-generation GWDs.

As mentioned in the previous chapter, the next generation of GWDs will most probably also require laser sources at $1.5\ \mu\text{m}$. Like Yb^{3+} -doped fiber amplifiers at $1.0\ \mu\text{m}$, Er^{3+} -doped and $\text{Er}^{3+}:\text{Yb}^{3+}$ -codoped fiber amplifiers in MOPA configuration provide some extraordinary advantages, in particular with respect to the special requirements of GWDs. Therefore, some promising work has been contributed to single-frequency Er^{3+} -doped and $\text{Er}^{3+}:\text{Yb}^{3+}$ -codoped fiber amplifiers at $1.5\ \mu\text{m}$ in the context of next-generation GWDs. In particular the maximum output power of single-frequency Er^{3+} -doped fiber amplifiers has been scaled significantly in recent years to output power levels of some tens of watts [Kuh11a; Kuh11b]. In addition, the beam quality of several special fiber designs has been investigated [Kuh10b] and a very promising method to suppress parasitic processes at $1.0\ \mu\text{m}$ in $\text{Er}^{3+}:\text{Yb}^{3+}$ -codoped fiber amplifiers has been developed [Kuh10a; Kuh09]. In the frame of this thesis this work has been continued and new aspects have been investigated, in particular with respect to the power scaling of single-frequency $\text{Er}^{3+}:\text{Yb}^{3+}$ -codoped fiber amplifiers (see chapter 4), the gain dynamics of $\text{Er}^{3+}:\text{Yb}^{3+}$ -codoped fiber amplifiers (see chapter 5), and novel pump sources for Er^{3+} -doped fiber amplifiers (see chapter 6).

CHAPTER 3

Fundamentals of Fiber Lasers and Amplifiers

This chapter provides a basic overview of the most important properties of optical fibers with respect to their application in fiber laser systems. First, an explanation of wave guidance in conventional step-index fibers is given and other important facts are highlighted. Then, active rare-earth doped fibers are introduced and their main properties are discussed, in particular as a substantial part of fiber lasers and amplifiers. The second part of this chapter gives an overview of those nonlinear effects in fiber lasers and amplifiers that are of relevance for this thesis and the presented results.

3.1 Waveguide Characteristics of Optical Fibers

In a conventional step-index fiber, as it is depicted schematically in Fig. 3.1, light is guided in the core of the fiber, i.e. a region with an increased index of refraction [Mar91]. From the principles of geometrical optics the actual guidance can be understood as a consequence of total internal reflections of plane waves at the boundary from the core to

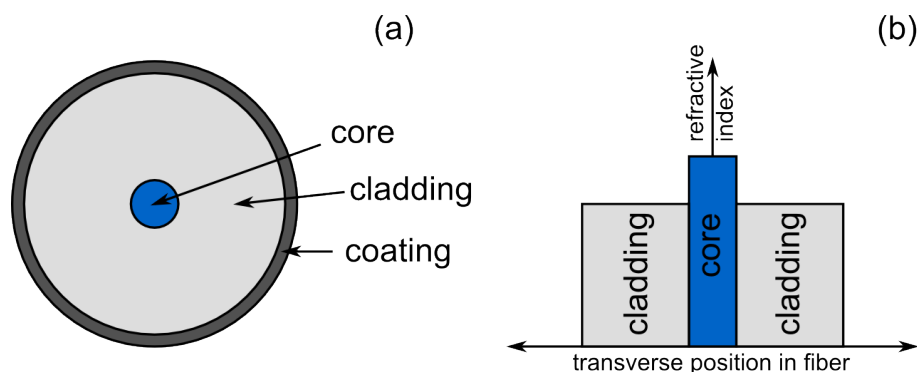


Figure 3.1: (a): Transverse profile of a standard step-index fiber. (b): Corresponding transverse refractive index profile.

the cladding. Since the typical core diameters are in the order of several micrometers, plane waves that propagate at a small angle through the fiber are predominant and the paraxial approximation can be applied. This approach leads to discrete transverse profiles $u_l(r)$ of the electric field amplitude that are determined by the radial Helmholtz equation

$$\frac{du_l^2(r)}{dr^2} + \frac{1}{r} \frac{du_l(r)}{dr} + \left(n^2(r)k_0^2 - \beta^2 - \frac{l}{r} \right) u_l(r) = 0 \quad (3.1)$$

where r is the distance from the center of the fiber core in transverse cylindrical coordinates, $n(r)$ the radial refractive index profile, β the propagation constant, k_0 the vacuum wavenumber of the signal wavelength, and l an integer that labels the transverse intensity profiles u_l . Mathematically, reasonable solutions of Eq. (3.1) only exist for discrete values β_{lm} of the propagation constant and are compositions of Bessel functions $J_l(r)$ in the fiber core and modified Bessel functions $K_l(r)$ in the cladding. Thus, the discrete profiles of the electric field amplitude, i.e. the modes that are guided by the fiber, are typically denoted as the LP_{lm} modes. The integer m characterizes the electric field amplitude in the radial direction and the integer l defines the symmetry, i.e. the number of nodes, in the azimuthal direction. As each of the modes has a different propagation constant β_{lm} , they have different effective refractive indices and guidance of a specific mode in the core is only possible if the effective refractive index lies between that of the core and the cladding.

An important parameter of step-index fibers is the numerical aperture (NA) of the core

$$NA = \sqrt{n_{\text{core}}^2 - n_{\text{clad}}^2} = \sin(\Theta_{NA}) \quad (3.2)$$

where n_{core} and n_{clad} are the refractive indices of the core and the cladding. Note that Θ_{NA} corresponds to the maximum angle at which light, thought of as rays, can be coupled into the core. In combination with the radius of the core r_c and the signal wavelength λ the NA also defines the V-parameter

$$V = \frac{2\pi}{\lambda} r_c NA. \quad (3.3)$$

The V-parameter is a figure of merit for the number of modes guided by the core of the fiber. For a V-parameter of less than 2.405 an ideal step-index fiber supports only one mode, which is typically denoted as the fundamental LP_{01} mode, and with increasing V-parameter more and more modes are guided by the fiber.

A lot of applications, e.g. interferometric GWDs, require single-mode operation, i.e. fiber laser systems that emit power almost exclusively in the LP_{01} mode. Thus, pumping

schemes of rare-earth doped single-mode fibers, which are introduced in the following section, would require pump sources with single-mode beam quality, so that they can be coupled efficiently into the fiber core. In particular diode lasers, which are most commonly used as pump sources for rare-earth doped fiber laser systems, are limited to output power levels of some watts if single-mode operation is required. However, stacked and arrayed diode lasers can provide output power levels of some kilowatts, but due to a comparably bad beam quality they can only be coupled into multimode fibers with core sizes of some hundreds of micrometers. Therefore, double-clad fibers have been developed, which utilize a special polymer as coating material. As the polymer has a well-defined refractive index below that of the cladding, multimode pump light can be guided within the cladding of the fiber. Indeed, the overlap of the pump light with the core decreases as the cladding size increases. Therefore, the pump light absorption per unit length in corresponding rare-earth doped double-clad fibers is also decreased to a certain extent. Another drawback of the double-clad design are helical cladding modes, i.e. modes that are guided by the cladding such that they do not overlap with the core. This can lead to a substantial amount of unabsorbed pump light [Kou02; Kou01]. In order to avoid this effect, non-circular shaped claddings can be used to obtain mode-mixing effects in the cladding, which prevent guidance of the helical modes [Po89]. Another drawback of double-clad fibers is the quite low thermal robustness of the polymer coating as the temperature of the coating should not exceed 80 °C [Lap09].

A particular enhancement of the double-clad design are fibers that utilize an additional pedestal between the core and the cladding as it allows to maintain small core NAs even for comparably large cores. These triple-clad fibers are for example very attractive regarding a potential application in GWDs, as it is discussed in more detail in chapter 4.

The most common glass to fabricate fibers is fused silica, i.e. high-purity silica (SiO_2). The actual fiber fabrication consists of two steps, the fiber preform production and the drawing of the fiber [Buc04]. Most commonly, the preform, i.e. a cylindrical fused silica rod that already contains the relative dimensions of the core and the cladding, is fabricated by the modified chemical vapor deposition (MCVD) method [Nag82]. In a first step, a hollow fused silica glass tube is heated up, while it is rotated around its axis of symmetry. Then, gaseous reactants are injected into the tube and the products of corresponding chemical reactions are accelerated towards the walls of the rod by thermophoresis, i.e. the effect that the temperature gradient between the center of the tube and the wall results in a net momentum transfer to the wall by particle collisions [Tan06a]. With this technique, different layers can be manufactured and each of the layers can contain only pure fused silica or can be doped with additional elements such as germanium, phosphorous

or aluminum to control the refractive index [Bal14]. Most commonly, the refractive index of the fiber core is increased by doping it with GeO_2 molecules and corresponding fibers are denoted as germanosilicate fibers. Doping with P_2O_5 molecules also increases the refractive index, but commonly only minor concentrations of this molecule are used as it allows to control the viscosity of the preform and as it yields a higher uniformity of the refractive index. Nevertheless, highly P_2O_5 -doped fibers, i.e. phosphosilicate fibers, are also commercially available, but they are not that common in comparison with germanosilicate fibers. Furthermore, also the doping with alumina, i.e. Al_2O_3 , can be used to increase the refractive index of the core and corresponding aluminosilicate glasses are mainly used as hosts for Er^{3+} -doped fibers.

Rare-earth doped fibers, which are introduced in the following section, are not fabricated by the MCVD method but with the solution doping technique [Tow87]. First, the cladding of the fiber is fabricated by the standard MCVD process and subsequently a porous fused silica layer is deposited at lower temperatures on the inner side of the cladding. Then, the whole tube is dipped into an aqueous and alcoholic solution that contains the dissolved rare-earth ions and the solution diffuses into the porous layer. Afterwards, the tube is dried, sintered, and finally collapsed into a solid preform.

The actual drawing of the fiber is performed in vertical drawing towers, in which the preform is molten locally and then drawn [Buc04]. The resulting fiber diameter can be controlled by regulating the actual temperature and the drawing rate.

3.2 Active Rare-Earth Doped Fibers

As already mentioned, optical fibers can also be doped with laser-active materials and used in fiber-based amplifiers and lasers. The most important dopants are the trivalent rare-earth cations Yb^{3+} (Ytterbium), Er^{3+} (Erbium) and Ho^{3+} (Holmium) as well as Tm^{3+} (Thulium) with emission wavelengths at around 1.0 μm , 1.5 μm , and 2.0 μm .

In particular high-power Yb^{3+} -doped fiber laser systems have experienced a lot of attention during the last decade, especially driven by the commercial interests of the material processing community. As a consequence, corresponding fiber technology, i.e. the actual Yb^{3+} -doped fibers and passive components, became quite mature and Yb^{3+} -doped fiber laser systems are well-known nowadays to be reliable, efficient, and cost-effective systems. The highest commercially available output power of a single-mode Yb^{3+} -doped laser system is 10 kW [Sti09] and theoretical investigations indicate that output power levels in excess of 70 kW should be feasible [Zhu11]. Furthermore, the highest reported output power of a single-frequency Yb^{3+} -doped amplifier is 800 W [Rob14]. Today, the most fundamental power scaling limitation of Yb^{3+} -doped fiber laser systems is the effect

of modal instabilities, i.e. a rapid deterioration of the output beam profile above a certain output power threshold, see [Zer14] for a detailed review on this topic. So far, it has been observed for different types of Yb^{3+} -doped fibers such as standard step index fibers or advanced fiber designs, e.g. photonic crystal fibers (PCFs). Several models to explain this effect have been developed and most of them assume a thermo-optically induced refractive index grating that leads to a coupling of the fundamental fiber mode with higher order modes. Although not yet observed, it is likely that the same effect will occur above a certain power threshold in Er^{3+} -, Tm^{3+} - and Ho^{3+} -doped systems.

Tm^{3+} - and Ho^{3+} -doped fiber laser systems at $2.0\ \mu\text{m}$ are very popular since they are more or less eye-safe, that means the laser power is absorbed to some extent in the human eye before it reaches the retina. In addition, they can act as seed or pump sources for nonlinear conversion schemes in order to reach the wavelength regime above $2.0\ \mu\text{m}$, where for example molecular fingerprints are very strong [Kub14]. Tm^{3+} -doped fibers can be pumped at $792\ \text{nm}$, where mature laser diodes are available at low costs. In addition, the obtainable efficiencies can exceed the quantum efficiency due to a cross-relaxation process in which one excited Tm^{3+} -ion decays to the upper laser state and excites a neighboring Tm^{3+} -ion from the ground state to the upper laser state [Jac04]. This 2-for-1 process makes Tm^{3+} -doped fiber lasers and amplifiers very attractive for commercial applications. The highest reported output power level of a Tm^{3+} -doped fiber laser is $1\ \text{kW}$ [Ehr10] and more than $600\ \text{W}$ have been achieved with a free-space pumped single-frequency Tm^{3+} -doped fiber amplifier [Goo09]. The record output power of a monolithic single-frequency Tm^{3+} -doped fiber amplifier is $210\ \text{W}$ [Liu14]. In addition, the output power of Ho^{3+} -doped fiber lasers has been scaled to more than $400\ \text{W}$ [Hem14].

Historically, the main motivation for the development of Er^{3+} -doped fibers and amplifiers has been the propagation loss minimum of fused silica at around $1550\ \text{nm}$ [Miy79], which allows to operate long distance fiber links with extremely low losses. Therefore, sophisticated Er^{3+} -doped fibers and corresponding technologies have been developed in the past by the telecommunication industry [Des02]. However, if high output power levels are required, Yb^{3+} - and Tm^{3+} -doped systems are more attractive, in particular due to the higher feasible efficiencies that are important for industrial applications. As a consequence, corresponding technology at $1.5\ \mu\text{m}$ is far less evolved and in particular the power scaling of single-frequency single-mode fiber amplifiers at $1.5\ \mu\text{m}$ for next-generation GWDs is very challenging. In the following sections, a basic introduction to Er^{3+} -doped and $\text{Er}^{3+}:\text{Yb}^{3+}$ -codoped fibers is given.

3.2.1 Er³⁺-Doping

A schematic overview of the most important electronic energy states of an Er³⁺ doped fiber is presented in Fig. 3.2 (a). As indicated by the zoom to the ground state $^4I_{15/2}$, the individual energy states are manifolds of different Stark levels, whose degeneration is abolished by the electric field of the glass host [Bec99]. Due to the structure of the individual energy states, one might expect discrete peaks in the absorption and emission spectra. However, as presented in Fig. 3.2 (b), typical absorption and emission cross sections for the $^4I_{15/2} \leftrightarrow ^4I_{13/2}$ transitions at around 1.5 μm are quite broad. Note that the details and the actual magnitude of the cross sections depend on the exact composition of the glass host and the Er³⁺-doping concentration. Reasons for the mentioned broadening are quite diverse, e.g. the finite lifetime of the excited state leads via the energy-time-uncertainty to a homogeneous broadening. Furthermore, the electric field of the glass host varies from site to site and contributes via corresponding perturbations of the Er³⁺ energy states to an inhomogeneous broadening.

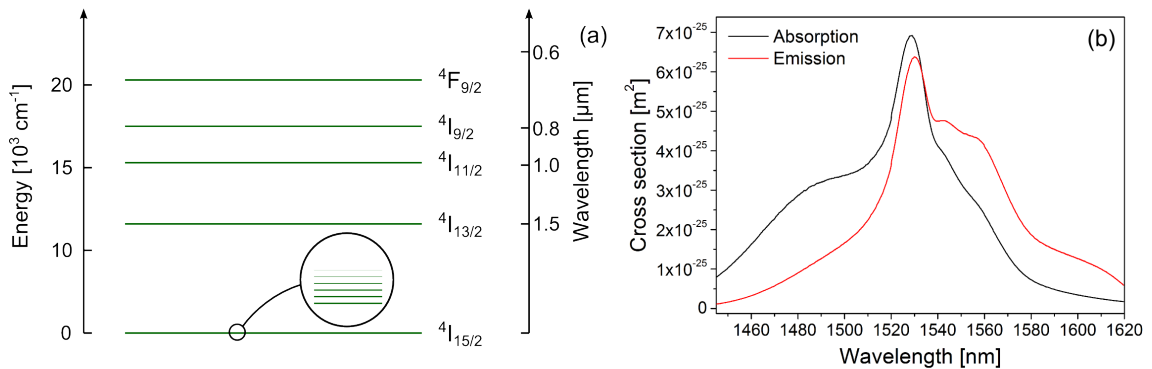


Figure 3.2: (a): Schematic overview of the most important energy states of an Er³⁺ doped fiber. Note that the wavelength and the energy is defined relative to the ground state $^4I_{15/2}$. (b): Exemplary emission and absorption cross sections of an Er³⁺-doped fiber at around 1.5 μm . The data were taken from a commercially available software (Liekki Application Designer) and have been originally determined by Liekki (now nLight (Vancouver, WA, USA)) from an Er³⁺-doped aluminosilicate fiber.

Most commonly, Er³⁺-doped fibers are pumped from the ground state $^4I_{15/2}$ to the upper state $^4I_{11/2}$ at a wavelength around 976 nm because the absorption at this wavelength is quite large. In fused silica, the lifetime of the upper Er³⁺ state $^4I_{11/2}$ is in the order of some microseconds, so that it quickly relaxes via non-radiative multi-phonon transitions to the metastable state $^4I_{13/2}$ [Lay77]. A potential seed signal at 1.5 μm can be amplified by stimulated transitions between the metastable state $^4I_{13/2}$ and the ground state $^4I_{15/2}$.

One of the most detrimental effects in Er³⁺-doped fibers is the homogeneous up-conversion, i.e. a dipole-dipole interaction of pairs of excited Er³⁺-ions in the metastable

$^4I_{13/2}$ state [Bec99]. While one of the Er^{3+} -ions is de-excited to the ground state, the other Er^{3+} -ion is excited to the $^4I_{9/2}$ state from where it relaxes via non-radiative multi-phonon transitions back to the $^4I_{13/2}$ state. Thus, this process leads to a reduction of excited Er^{3+} -ions and it limits the obtainable gain, i.e. the efficiency, of a corresponding fiber amplifier. Furthermore, the higher the doping concentration, the shorter the average distance between the individual Er^{3+} -ions and the stronger the detrimental impact of homogeneous up-conversion [Mys97].

Another detrimental effect in Er^{3+} -doped fibers is the clustering of the Er^{3+} -ions during the fiber manufacturing [Ain91]. Within the clusters, the average distance between the individual Er^{3+} -ions is quite small. Thus, if one of the Er^{3+} -ions is already excited and another Er^{3+} -ions gets also excited, up-conversion occurs immediately. This effect decreases the number of Er^{3+} -ions that can be actually excited drastically and is independent of the actual level of excitation, i.e. the population inversion. Most commonly, it is denoted as pair-induced quenching (or inhomogeneous up-conversion) and advanced models of up-conversion effects in Er^{3+} -doped fibers consider pair-induced quenching as well as homogeneous up-conversion [Mys97].

By codoping fused silica with alumina, i.e. Al_2O_3 , the solubility of the Er^{3+} -ions can be increased and the formation of clusters is suppressed to a certain extent [Min91]. In particular compared to germanosilicate fibers the feasible doping concentration is increased roughly by an order of magnitude [Bec99]. This is the reason why almost exclusively aluminosilicate glasses are used as hosts for Er^{3+} -doped fibers. However, as the Al_2O_3 -codoping also increases the refractive index of the core, Er^{3+} -doped fibers with core NAs of less than 0.1 are barely commercially available [Tan06b]. In addition, although the solubility is increased by the Al_2O_3 -codoping, if compared to Yb^{3+} - or Tm^{3+} -doped fibers, the feasible pump light absorption of Er^{3+} -doped fibers is still about two orders of magnitude lower.

The low pump light absorption and the clustering in combination with the up-conversion are essentially the reasons why cladding-pumped Er^{3+} -doped fiber lasers systems that are pumped at 976 nm are lacking high output power levels and decent efficiencies. With fiber amplifier setups the maximum output power has been scaled in recent years to 67 W (30 % slope efficiency) with a multimode fiber [Kuh11a], to 54 W (24 % slope efficiency) with a few-mode fiber that provided almost single-mode operation [Kuh11c], and to 70 W (18.5 % slope efficiency) with a specially designed Er^{3+} -doped PCF [Kuh11b]. Furthermore, a specially designed and optimized Er^{3+} -doped single-mode fiber has been used in a fiber laser setup and an output power of 75 W with a record efficiency of 40 % has been obtained [Kot13].

Er^{3+} -doped fiber laser systems can also be pumped efficiently at around 1480 nm or in-band (resonantly) at around 1.53 μm . With a high-power cascaded Raman fiber laser (CRFL) at 1480 nm the output power of a core-pumped Er^{3+} -doped single-mode fiber laser was scaled to more than 100 W (71 % slope efficiency) [Sup12a]. Furthermore, with multiple fiber coupled multimode laser diodes at 1.53 μm , which cladding-pumped an Er^{3+} -doped fiber laser, an output power of 88 W (69 % slope efficiency) has been obtained [Zha11]. However, compared to these more or less custom and complex configurations, diode lasers at 976 nm are still the most promising pump sources, in particular as they allow for very cost-effective and simple setups. Nevertheless, some important properties of CRFLs at 1480 nm are investigated in chapter 6 of this thesis because core-pumped Er^{3+} -doped fiber amplifiers are of particular interest for next-generation GWDs for several reasons.

3.2.2 $\text{Er}^{3+}:\text{Yb}^{3+}$ -Codoping

In order to increase the pump light absorption of Er^{3+} -doped fibers at 976 nm they can be codoped with Yb^{3+} [Sni65]. The most important electronic energy states of a corresponding $\text{Er}^{3+}:\text{Yb}^{3+}$ -codoped fiber are presented in Fig. 3.3. As the typical Yb^{3+} -doping concentration is about one order of magnitude higher than that of Er^{3+} and because the absorption cross section at 976 nm is also significantly higher, the pump light is absorbed mainly by the Yb^{3+} -ions. Subsequently, the excitation energy is transferred to the Er^{3+} -ions by a dipole-dipole interaction. The actual magnitude, i.e. the probability, of this energy transfer is determined by the overlap integral of the Yb^{3+} emission and the Er^{3+} absorption cross section. Without further efforts, the lifetime of the upper Er^{3+} state $^4\text{I}_{11/2}$ is too large and energy can be transferred back from the Er^{3+} -ions to the Yb^{3+} -ions, so that the energy transfer is not efficient. However, it was discovered that the lifetime is decreased in P_2O_5 -codoped aluminosilicate fibers so much, that the back-transfer of

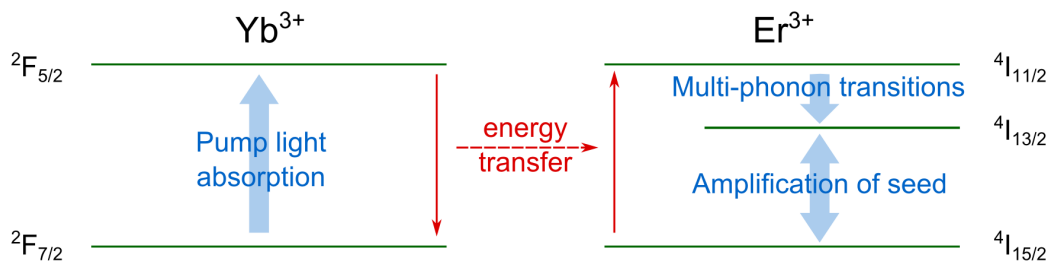


Figure 3.3: Illustration of the most important energy states of an $\text{Er}^{3+}:\text{Yb}^{3+}$ -codoped fiber. The energy transfer process corresponds to the de-excitation of an excited Yb^{3+} -ion and the subsequent excitation of an Er^{3+} -ion.

energy is significantly suppressed [Tow91]. The physical reason for this is a quite large Raman shift of the phosphoaluminosilicate glass, i.e. only a comparably low number of phonons is necessary to drive the multi-phonon transition from the upper Er^{3+} state $^4\text{I}_{11/2}$ to the metastable state $^4\text{I}_{13/2}$. Thereby, the probability of this transition is increased and the corresponding lifetime is decreased. However, the P_2O_5 -codoping also increases the refractive index of the fiber core and limits without further efforts the feasible core NA of $\text{Er}^{3+}:\text{Yb}^{3+}$ -codoped fibers to 0.2 [Tan06b]. Another drawback of the P_2O_5 -codoping is the formation of a refractive index dip in the middle of the fiber core [Can07], which can have a negative impact on the beam quality [Can06]. On the other hand, the Yb^{3+} -codoping increases the solubility of the Er^{3+} -ions during the fiber fabrication, i.e. it suppresses the formation of Er^{3+} -ion clusters to a certain extent [Kir15].

The most fundamental limitation regarding the power scaling of $\text{Er}^{3+}:\text{Yb}^{3+}$ -codoped fiber lasers and amplifiers is the excess generation of Yb^{3+} -amplified spontaneous emission (ASE), i.e. unsaturated gain at around $1.0\ \mu\text{m}$, which makes the corresponding system very prone to parasitic self-lasing processes. The record output power of an $\text{Er}^{3+}:\text{Yb}^{3+}$ -codoped fiber laser is 297 W [Jeo07]. However, this result is also exemplary for the detrimental effect of the self-lasing as the slope efficiency of the laser was 40 % at lower output power levels and decreased to around 20 % at higher output power levels due to parasitic lasing at $1.0\ \mu\text{m}$. Moreover, the highest reported output power of a single-frequency $\text{Er}^{3+}:\text{Yb}^{3+}$ -codoped fiber amplifier of 150 W was limited by the excess generation of Yb^{3+} -ASE and a corresponding significant reduction of the slope efficiency [Jeo05]. Note that the utilized fiber was also highly multimode. More recently, the output power of an $\text{Er}^{3+}:\text{Yb}^{3+}$ -codoped fiber laser that was resonantly cladding-pumped at 1535 nm has been scaled up to 264 W [Jeb14]. This approach is very attractive as it allows to avoid the generation of Yb^{3+} -ASE but benefits from the increased solubility, i.e. the comparably high absorption, of the Er^{3+} -ions in $\text{Er}^{3+}:\text{Yb}^{3+}$ -codoped fibers. However, as argued earlier, diode lasers at 976 nm are still the most promising pump sources as they allow for very cost-effective and simple setups. Therefore, techniques to suppress the excessive generation of Yb^{3+} -ASE and corresponding parasitic processes at $1.0\ \mu\text{m}$ are necessary and one of the most promising approaches, namely the co-seeding method, has been used in the frame of this thesis and is introduced in detail in chapter 4.

3.3 Nonlinear Processes in Fibers

As an electromagnetic wave propagates through a fiber, the electric field component \mathbf{E} induces by interactions with the glass host elementary electric dipoles, i.e. a polarization \mathbf{P} . In general, the relation between the induced polarization and the electric field is nonlinear

and anisotropic [Boy03]

$$\mathbf{P} = \varepsilon \left(\chi^{(1)} \mathbf{E} + \chi^{(2)} \mathbf{E}^2 + \chi^{(3)} \mathbf{E}^3 + \dots \right) \quad (3.4)$$

where $\chi^{(n)}$ is a tensor of rank $n+1$. $\chi^{(1)}$ is the linear susceptibility, $\chi^{(2)}$ the second order susceptibility, $\chi^{(3)}$ the third order susceptibility, and ε the permittivity. As the temporal and spatial evolution of the electric field is also coupled to the polarization via Maxwell's equations, strong electric fields, i.e. high intensities, can cause nonlinear effects. In fibers the light is confined to small areas in the size of the fiber core, so that high intensities per unit area are common and nonlinear effects exhibit comparably low thresholds. However, as glasses are centrosymmetric materials, they do not exhibit second order nonlinearities ($\chi^{(2)} = 0$) [Agr01]. The third order nonlinearities are either effects related to delayed responses of the glass host such as the Raman or Brillouin Scattering (these effects are introduced in the following two sections) or effects based on the Kerr effect. The Kerr effect is the instantaneous change of the refractive index n induced by the intensity I

$$\Delta n = n_2 I \quad (3.5)$$

where

$$n_2 = \frac{3}{8n_{\text{lin}}} \text{Re}(\chi^{(3)}) \quad (3.6)$$

is the nonlinear and n_{lin} the linear index of refraction. Thus, as the intensity increases, the Kerr effect causes a larger refractive index and imprints a corresponding phase shift on the electric field. One of the nonlinear effects related to the Kerr effect is the four-wave mixing (FWM), which leads to a spectral broadening of intense signals due to temporal modulations of the index of refraction. This effect is described in more detail at the end of this chapter.

3.3.1 Stimulated Raman Scattering

From a quantum mechanical point of view, light with a frequency ω_0 that propagates through a fiber can also be described as photons with energy $\hbar\omega_0$, where \hbar is the reduced Planck constant. These photons can scatter inelastically on phonons, i.e. fundamental vibrations of the SiO_2 molecules. The scattering on optical phonons, i.e. vibrations with frequencies in the optical domain, is denoted as Raman Scattering. As the scattering occurs, part of the energy is either transferred from the phonon to the photon or vice versa. Hence, as depicted in Fig. 3.4, after the scattering process the light has either

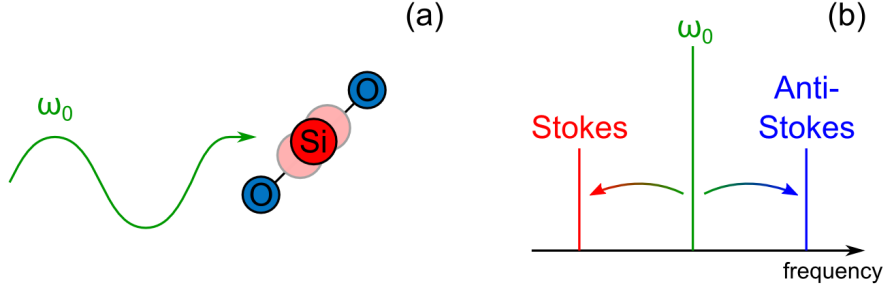


Figure 3.4: Illustration of the spontaneous Raman scattering. (a): An incoming light wave (a photon) with frequency ω_0 (energy $\hbar\omega_0$) is scattered inelastically on a molecular SiO₂ vibration, i.e. a phonon. Thereby, part of the energy is transferred from the phonon to the photon or vice versa. (b): After the scattering process the light wave has either a higher (Anti-Stokes shifted) or a lower (Stokes shifted) frequency.

a higher (Anti-Stokes shifted) or a lower (Stokes shifted) frequency. This spontaneous Raman scattering is weak and isotropic, but it can become quite efficient as a result of the stimulated Raman scattering (SRS). To understand the physical mechanisms behind the SRS process it is convenient to use a classical point of view [Boy03]. If the SiO₂ molecules vibrate with a frequency ω_{mol} , they induce, under the assumption that the molecular dipole moment depends on the internuclear distance, an oscillating polarization. Thus, the refractive index is modulated with frequency ω_{mol} and imprints via a corresponding phase modulation sidebands at $\omega_0 - \omega_{\text{mol}}$ (Stokes component) and $\omega_0 + \omega_{\text{mol}}$ (Anti-Stokes component) on some incident laser field with frequency ω_0 . These sidebands can then beat with the original laser field, which leads to a total intensity that is also modulated with frequency ω_{mol} . This modulated intensity resonantly drives the molecular vibration and, as the oscillation becomes stronger, the generated Stokes and Anti-Stokes sidebands also increase. The evolution of the amplitudes of the Stokes and the Anti-Sokes wave along the fiber is given in the slowly-varying amplitude approximation by [Boy03]

$$\frac{A_{s,a}}{dz} = \alpha_{s,a} A_{s,a} \quad (3.7)$$

where

$$\alpha_{s,a} = 12\pi i \frac{\omega_{s,a}}{nc} \chi_R(\omega_{s,a}) |A_L|^2 \quad (3.8)$$

is in principle an absorption or gain coefficient. Note that no phase matching condition must be fulfilled for the SRS process because $\alpha_{s,a}$ depends only on the modulus $|A_L|^2$ of

the complex amplitude A_L of the incident laser field. The Raman susceptibility

$$\chi_R(\omega) \propto (\omega_{\text{mol}}^2 - (\omega_0 - \omega)^2 + 2i(\omega_0 - \omega)\gamma)^{-1} \quad (3.9)$$

depends on the attenuation γ of the molecular oscillation and is negative imaginary for the Stokes component and positive imaginary for the Anti-Stokes component. Thus, the Stokes component experiences an amplification, whereas the Anti-Stokes component is attenuated, see Eq. (3.7).

A more convenient way to describe the amplification of the Stokes wave and the absorption of the pump wave along the fiber is given by [Agr01]

$$\frac{P_s}{dz} = g_R P_p P_s \quad (3.10)$$

where P_p is the pump power, P_s the power of the Stokes field, and g_R the Raman gain coefficient, which depends on the actual glass host. Standard germanosilicate fibers provide a quite broad (up to 40 THz) SRS gain spectrum with a maximum at around 13.2 THz with respect to the frequency of the pump source. Eq. (3.10) can be further expanded by terms that correspond to the spontaneous Raman scattering, background losses, and scattering to the next Stokes order, as it is discussed in more detail in chapter 6 in the context of CRFLs.

3.3.2 Stimulated Brillouin Scattering

The photons of some laser field can also scatter inelastically on acoustic phonons, i.e. vibrations of the SiO_2 molecules with frequencies in the acoustic domain. This process is called Brillouin Scattering and similar to the Raman process, it can become very efficient for the Stokes component as a result of the stimulated Brillouin scattering (SBS) [Agr01]. As a consequence of energy and momentum conservation, SBS occurs only in the backward direction with respect to the propagation direction of the signal and leads to an attenuation of the signal power. Similar to SRS, the interaction of the signal power P_{signal} and the power of the Stokes wave P_{Stokes} , i.e. the attenuation of the signal along the fiber, can be described as

$$\frac{P_{\text{signal}}}{dz} = -g_B P_{\text{signal}} P_{\text{Stokes}}. \quad (3.11)$$

The SBS gain spectrum g_B is Lorentzian shaped, has a maximum at around 11 GHz for a signal wavelength of 1550 nm and the full width at half maximum is less than 100 MHz in fused silica fibers. As the effective Brillouin gain peak scales to a certain extent inversely

with the linewidth of the signal, SBS is the most dominant nonlinear effect for single-frequency signals. It can be very harmful for the whole laser system as it generates for example giant self-pulses that can destroy optical components. Thus, although it was not explicitly observed in the frame of this thesis, SBS is one of the most fundamental power scaling limitations of single-frequency fiber amplifiers in the context of GWDs. This is also the reason why almost exclusively fiber designs with large core diameters, i.e. large mode-area (LMA) fibers, are considered as being suitable for single-frequency fiber amplifiers in next-generation GWDs. As a large core diameter reduces the intensity per unit area, it also decreases the threshold of nonlinear effects, in particular SBS. Furthermore, as Eq. (3.11) indicates that the power of the backward propagating Stokes wave depends on the actual length of the fiber, a long fiber yields a comparably low SBS threshold. Thus, short fiber lengths are preferred in the context of single-frequency fiber amplifiers.

3.3.3 Four-Wave Mixing

Even in single-frequency lasers with a linewidth in the order of some kilohertz several longitudinal cavity modes actually resonate and the total electric field is a superposition of these individual modes. In order to understand the FWM process, it is useful to assume an initial laser field that consists only of two modes with frequencies ω_1 and ω_2 and that propagates through a fiber, see Fig. 3.5 (a). In addition, chromatic dispersion, i.e. the dependency of the refractive index on the actual frequency, is neglected in the following, so that the differential phase between the modes is constant. While the two modes propagate through the fiber, the intensity is modulated with a frequency $\omega_2 - \omega_1$, which corresponds to the beating of the two modes. As depicted in Fig. 3.5 (b), this modulation of the intensity leads via the Kerr effect to a modulation of the refractive index of the fiber that

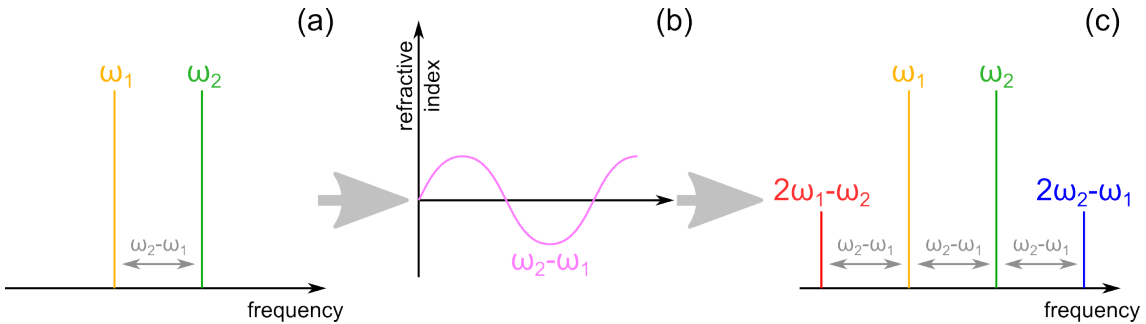


Figure 3.5: Illustration of the four-wave mixing effect. (a): Two modes with different frequencies propagate through a fiber. (b): The intensity and, via the Kerr effect, the refractive index is modulated with the beat frequency of the two modes. (c): The modulation of the refractive index generates via a corresponding phase modulation sidebands, i.e. new frequency components.

imprints a corresponding phase modulation on each of the two modes. Thereby, frequency side bands, i.e. new frequency components, are generated. These sidebands are located at $\pm(\omega_2 - \omega_1)$ with respect to the initial frequencies of the two modes, see Fig. 3.5 (c). Indeed, as this simple model does not include dispersion, the phase relation between the individual modes is constant and the beating of the two initial modes resonantly drives the generation of the sidebands. Furthermore, other pairs of modes will also start to create new beat frequencies that will resonantly generate corresponding new sidebands. However, in every real system the dispersion counteracts these processes to a certain extent. Nevertheless, if an intense laser beam with a substantial number of modes propagates through a fiber with a sufficiently large nonlinear refractive index, the beating of the individual modes will constantly generate new frequency sidebands that can broaden the spectrum of the laser to a certain extent. This effect can be very harmful for fiber lasers as it leads to additional losses, e.g. by power that leaks out of the cavity at spectrally narrow components. A corresponding example are CRFLs, see chapter 6.

CHAPTER 4

Power Scaling of Er³⁺:Yb³⁺-Codoped Fiber Amplifiers

As argued in the previous chapters of this thesis, Er³⁺-doped and Er³⁺:Yb³⁺-codoped single-frequency fiber amplifiers in MOPA configuration are promising candidates as laser sources at 1.5 μm for next-generation GWDs. However, if pumped at 976 nm and with respect to the special requirements of GWDs, Er³⁺:Yb³⁺-codoped fiber amplifiers provide some advantages compared to Er³⁺-doped fiber amplifiers, as it is discussed in detail in the following section.

Er³⁺:Yb³⁺-codoped LMA fibers were lacking either a good beam quality or a sufficient power handling capability, so far. Therefore, a novel Er³⁺:Yb³⁺-codoped triple-clad LMA fiber has been investigated in the frame of this thesis. The results, which are presented in the first part of this chapter, reveal the potential of this fiber to deliver high output power levels as part of a single-frequency MOPA setup in combination with an excellent beam quality, i.e. a high TEM₀₀ mode content of more than 90 %. In order to suppress the parasitic processes related to the excessive generation of Yb³⁺-ASE, the co-seeding method was used. Although theoretical studies predict that high output power levels should be feasible with this approach [Han10], experimental investigations were limited to output power levels of less than 10 W, so far [Kuh10a; Kuh09; Sli13]. Within the frame of this thesis, the output power of the co-seeded single-frequency Er³⁺:Yb³⁺ triple-clad LMA fiber amplifier was scaled to 61 W.

The second part of this chapter is dedicated to another novel LMA fiber concept, namely leakage channel fibers (LCFs) [Won05] and their possible application as passive delivery fibers in GWDs at 1.0 μm and 1.5 μm . For this thesis, the TEM₀₀ mode content of a particular passive LCF with a core diameter of around 50 μm was measured at both wavelengths for the first time. In addition, the influence of different bending diameters and launching conditions on the beam quality has been investigated experimentally.

At the end of this chapter it is discussed how the TEM₀₀ mode content of beam profiles that contain higher order modes can be determined consistently. A similar investigation has already been performed for M²-measurements on few-mode LMA fibers, i.e. LMA fibers that support some higher order modes [Wie07]. However, for the commonly used method to determine the TEM₀₀ mode content by a non-confocal scanning ring cavity, see for example [Kar12a] or [Kuh10b], such an analysis was missing, so far. The presented results confirm that some serious care has to be taken when the TEM₀₀ mode content of a few-mode LMA fiber is determined by this method.

Part of the work and the results presented in this chapter have been published beforehand in [Ste14] and [Ste15c].

4.1 Co-Seeded Large Mode-Area Er³⁺:Yb³⁺-Codoped Fiber Amplifier

As GWDs require high output power levels and single-frequency operation, corresponding fiber amplifiers are prone to SBS. However, the actual threshold for the onset of SBS can be influenced by several approaches related to the fiber and amplifier design.

For example, by keeping the utilized fiber short the SBS threshold can be increased to a certain extent. However, the actual length of the active fiber also determines the pump light absorption and therefore the overall efficiency of the amplifier. Hence, a sufficiently strong pump light absorption per unit length is required, but in particular Er³⁺-doped fibers suffer from a low absorption if pumped at 976 nm. As mentioned earlier, this is due to the quite small absorption cross section of the Er³⁺-ions at 976 nm and the comparably low feasible doping concentration, which is limited by the clustering of the Er³⁺-ions in combination with up-conversion effects.

The common codoping with Yb³⁺-ions increases the pump light absorption [Sni65]. However, incorporated in high-power fiber amplifiers or lasers, Er³⁺:Yb³⁺-codoped fibers are prone to parasitic processes at 1.0 μm, in particular due to significant amounts of Yb³⁺-ASE at high pump power levels [Jeo05; Jeo07]. To overcome this limitation, several approaches have been proposed and investigated. For example, specially designed fibers such as short-wavelength filtered PCFs [Shi08] or photonic bandgap fibers with Yb³⁺-band suppression [Ouy14] were studied. It was also shown that a specially doped standard step-index fiber in a counter-propagating pumping scheme in combination with a substantial amount of seed power leads to efficient amplification at 1.5 μm and significant suppression of the Yb³⁺-ASE [Mor07]. Furthermore, the incorporation of long-period fiber Bragg gratings (FBGs) between several amplifier stages has proven to be a reliable approach to filter the Yb³⁺-ASE in an all-fiber setup [Yus05]. However, all these approaches only focus on avoiding parasitic effects, e.g. by decreasing the gain at 1.0 μm, but they do not address the origin

and take advantage of it. In contrast, during the last years theoretical [Han11; Han10] and experimental [Kuh10a; Kuh09; Sli13] investigations have revealed great potential of a method that is called co-seeding. Basically, the idea is to utilize a second seed laser at 1.0 μm to achieve stable amplification and to suppress by this any parasitic processes related to the Yb³⁺-ASE. However, this method has another great advantage that sets itself apart from all other approaches. If the absorption cross-section for the co-seeding wavelength is non-zero, if the fiber is long enough, and if the co-seed is co-propagating with the pump, the co-seed can extract excess energy mainly from the pump launch end of the fiber and can act as a second pump source mainly towards the other end of the fiber, where it is reabsorbed by the Yb³⁺-ions. Thus, the co-seeding approach does not only suppress parasitic processes at 1.0 μm , but it can also increase the efficiency of the amplifier at 1.5 μm significantly, as it has already been confirmed experimentally [Kuh10a]. A slightly modified co-seeding approach is presented in [Sob12a; Sob11; Sob12b] and [Sob14]. Here, the 1.0 μm signal is generated by a loop resonator, e.g. by feeding the 1.0 μm signal from the output end of the amplifier back to the input. It was proven experimentally that the generated signal at 1.0 μm acts again as an additional pump source and increases the efficiency at 1.5 μm . However, although the actual wavelength of the loop resonator can be controlled by incorporating for example FBGs, the modified approach is lacking flexibility with respect to the actual co-seed wavelength. In addition, theoretical studies are missing for the modified approach, e.g. strategies to maximize the suppression of the Yb³⁺-ASE as well as the increase of efficiency at 1.5 μm . So far, experimental investigations regarding the co-seed approach have been limited to output power levels below 10 W. However, as theoretical investigations did not reveal any limitations regarding the obtainable output power levels [Han10], this approach is very promising for the power scaling of single-frequency Er³⁺:Yb³⁺-codoped fiber amplifiers at 1.5 μm for next-generation GWDs.

The SBS threshold of single-frequency fiber amplifiers can also be increased by using a LMA fiber with a large core diameter as this approach decreases the intensity per unit area. However, increasing the core size of a conventional double-clad fiber while maintaining single-mode operation requires to decrease the NA of the core, i.e. the refractive index step from the core to the cladding. The necessary P₂O₅-codoping in Er³⁺:Yb³⁺-codoped fibers, which suppresses the energy back-transfer from the Er³⁺-ions to the Yb³⁺-ions, leads to a very pronounced difference of the index of refraction of the core and the cladding. Thus, conventional Er³⁺:Yb³⁺-codoped double-clad fibers with core diameters of more than 20 μm and single-mode operation are not technically feasible.

In particular with respect to single-frequency fiber amplifiers for GWDs, a different LMA fiber design, namely an Er³⁺:Yb³⁺-codoped multifilament core (MFC) fiber with

a hexagonal core size of 31/28 μm was studied [Kuh10b]. The core region of this fiber consisted of different Er³⁺:Yb³⁺-codoped filaments, i.e. multiple equally-spaced small single-mode cores, each with a high NA. The transversal dimension of the filaments was in the order of some micrometers. Corresponding refractive index averaging effects led to a comparably low effective NA of the core region and allowed for propagation of only one supermode. The TEM₀₀ content, i.e. the overlap of the supermode with a TEM₀₀ mode, was between 90 % and 95 %, depending on the actual output power. However, the maximum output power of 8.5 W at 1.5 μm was limited by a thermal failure of the silicone rubber coating. In addition, the possibility to splice MFC fibers to each other or to conventional step-index fibers remains to be investigated in detail. Thus, with respect to the current level of technology, the MFC fiber design provides good prospect, but it requires further refinements to be really suitable for all-fiber Er³⁺:Yb³⁺-codoped LMA single-frequency fiber amplifiers with significant output power levels.

As also pointed out in [Kuh10b], triple-clad LMA fibers with an additional refractive-index pedestal between the core and the cladding are a promising enhancement of the double-clad design. By codoping part of the cladding that surrounds the core with germanium, i.e. GeO₂, the refractive index of this pedestal is increased and the core NA is decreased. Note that typically not the whole cladding is codoped with germanium as this would increase the costs during manufacturing and most probably alter the mechanical stability of the fiber. Most commonly, the pedestal is round and supports stable helical modes that marginally overlap with the core. Hence, part of the pump light in a corresponding amplifier setup is trapped in the pedestal and is not absorbed. Indeed, decreasing the diameter of the pedestal potentially lessens the amount of unabsorbed pump light, but it also decreases the beam quality as core light couples more likely to pedestal modes. Nevertheless, it has been shown that in Er³⁺:Yb³⁺-codoped LMA fibers the core NA can be decreased to 0.1 by the triple-clad design [Tan06b]. However, even with such a low core NA corresponding fibers with core sizes larger than 20 μm still support higher order modes due to a V-parameter of more than 4 at 1.55 μm . Although it is well-known that bending of the fiber can lead to a significant suppression of the higher order modes [Kop00], this approach becomes less effective with increasing core size [Gal04]. Thus, the commercially available triple-clad fibers that have been analyzed in [Kuh10b] had core sizes of 23 μm (NA of 0.11) and 25 μm (NA of 0.1) but measured TEM₀₀ mode contents as low as 80 %.

The bend induced filtering of the higher order modes in triple-clad LMA fibers can be enhanced by adding a refractive index dip at the transition from the core to the pedestal, as it has been confirmed with Yb³⁺-doped LMA fibers [Dro10; Lap07]. The pedestal, i.e. the inner cladding, is then typically denoted as being depressed. In addition, the

resulting refractive index profile of the core and the depressed pedestal is said to have a W-profile because a symmetrical plot of the profile resembles the letter W. Such refractive index profiles were originally studied because they allow to control the dispersion of the fiber [Kaw74]. Technically, such a depressed pedestal and a corresponding enhanced bend-induced suppression of the higher order modes is very challenging to achieve. Thus, $\text{Er}^{3+}:\text{Yb}^{3+}$ -codoped LMA fibers with this feature were not available, so far. The novel $\text{Er}^{3+}:\text{Yb}^{3+}$ -codoped triple-clad LMA fiber that is introduced and analyzed in the following incorporates this feature for the first time.

4.1.1 Fiber Design and Experimental Setup

The $\text{Er}^{3+}:\text{Yb}^{3+}$ -codoped triple-clad LMA fiber was designed, developed, and drawn at INO (Québec City, QC, Canada). A schematic of the geometry and the refractive index profile of the fiber is presented in Fig. 4.1. First, an interim preform that consisted of the depressed inner cladding and the $\text{Er}^{3+}:\text{Yb}^{3+}$ -codoped phosphosilicate core was fabricated by the MCVD process and solution doping. During the MCVD process the inner cladding was deposited out of GeO_2 - and P_2O_5 -doped fused silica [Lap07]. The well-known formation of an index dip caused by the P_2O_5 -codoping of the core was suppressed by taking special measures during the preform fabrication. The final preform was obtained by sleeving a pure fused silica substrate tube over the interim preform. Subsequently, this tube, i.e. the second cladding, was etched to obtain the desired pump guide to core diameters ratio and then hexagonally-shaped to ensure efficient optical pumping of the core. During the actual fiber drawing the third cladding, i.e. a low refractive index polymer, was applied on-line.

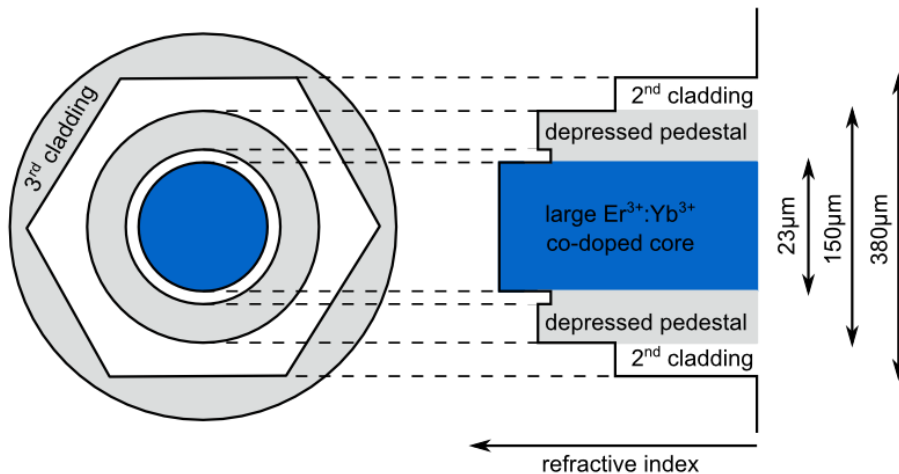


Figure 4.1: Schematic overview of the geometry and the refractive index profile of the $\text{Er}^{3+}:\text{Yb}^{3+}$ -codoped triple-clad LMA fiber.

In addition, a secondary coating, designed to ensure robustness of the fiber, was applied over the third cladding, i.e. the first coating layer.

A measured refractive index profile of the $\text{Er}^{3+}:\text{Yb}^{3+}$ -codoped triple-clad LMA fiber at 1000 nm relative to the secondary cladding is presented in Fig. 4.2 (a). The core NA, defined with respect to the depressed index level of the inner cladding, was determined to be 0.09. With a measured core diameter of around 23 μm the core would normally support higher-order modes. However, as explained, the W-index profile makes it effectively single-mode if coiled. The optimal coiling diameter was calculated by INO to be 30 cm. Indeed, higher-order modes can still propagate within the pedestal, but with a pedestal-to-core ratio of over 6 in diameters, these cladding modes extend largely out of the core and their overlap with the $\text{Er}^{3+}:\text{Yb}^{3+}$ -codoped core is very small. In Fig. 4.2 (b) the amplitude distribution of the fundamental LP_{01} mode, calculated from the measured refractive index distribution of Fig. 4.2 (a), is presented. The calculated effective mode area is around 290 μm^2 and by fitting a TEM_{00} mode to the calculated LP_{01} amplitude distribution the overlap factor of the LP_{01} mode with the TEM_{00} mode was determined to be 99.7%. In addition, the absorption at 976 nm was measured by INO to be around 1.5 dB/m.

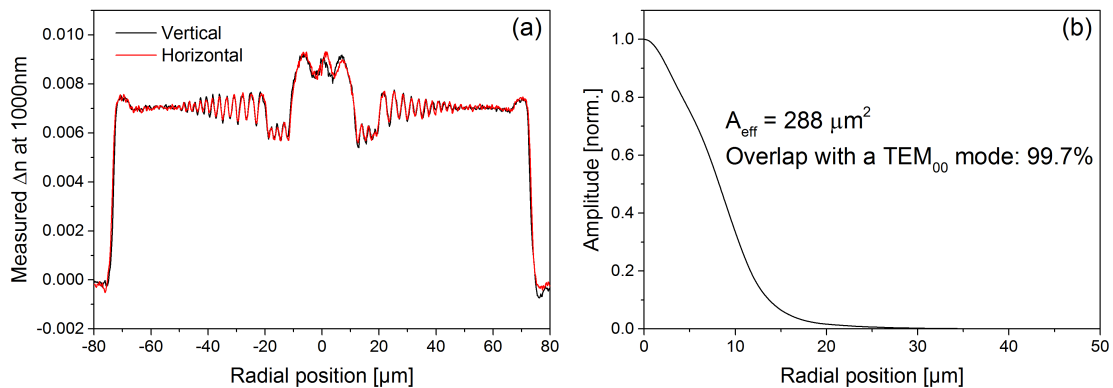


Figure 4.2: (a): Measured refractive index profile of the $\text{Er}^{3+}:\text{Yb}^{3+}$ -codoped triple-clad LMA fiber at 1000 nm relative to the secondary cladding. Note that the oscillations are real and correspond to evaporation of dopants during the MCVD process (b): Corresponding simulated LP_{01} amplitude distribution.

The experimental setup used for all experiments is presented in Fig. 4.3. A 22 m long piece of the $\text{Er}^{3+}:\text{Yb}^{3+}$ -codoped triple-clad LMA fiber was used in a counter pumped MOPA setup. Both fiber ends were angle cleaved in order to suppress back reflections at 1.0 μm and 1.5 μm . The 976 nm pump source (LDM500, Laserline (Mülheim-Kärlich, Germany)) provided a power of up to 500 W out of a fiber with a core diameter of 200 μm and a NA of 0.22. The corresponding multimode light was launched after collimation into

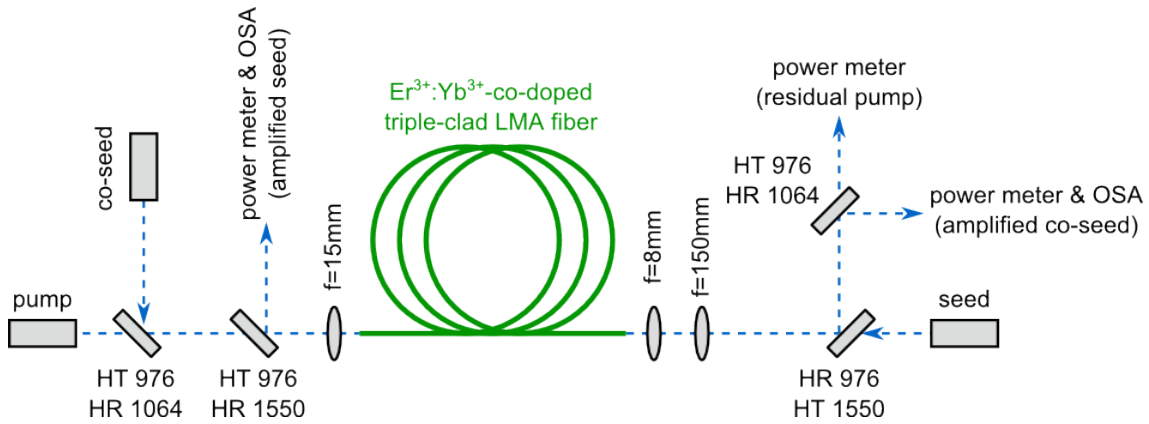


Figure 4.3: Schematic of the experimental setup for the power scaling of the single-frequency $\text{Er}^{3+}:\text{Yb}^{3+}$ -codoped triple-clad LMA fiber amplifier. OSA: optical spectrum analyzer.

the pump cladding of the triple-clad fiber with an aspherical $f=15$ mm lens. The $1.5\ \mu\text{m}$ seed source was a commercially available pre-amplified single-frequency fiber laser (TheRock, NP Photonics (Tucson, AZ, USA)) with a kHz linewidth, a center wavelength of $1556\ \text{nm}$, and an output power of $2\ \text{W}$. The seed light was mode matched to the fundamental mode of the triple-clad fiber with a spherical $f=150$ mm lens and an aspherical $f=8$ mm lens. The co-seed source was a self-made tunable Yb^{3+} -doped fiber ring laser, which was tunable from $1030\ \text{nm}$ to $1060\ \text{nm}$ and provided a power of up to $2\ \text{W}$ at all wavelengths. The co-seed light was launched into the triple-clad fiber with the same $f=15$ mm lens that was used for pump light coupling. Therefore, the mode matching of the co-seed into the fiber core was not perfect, but by beam walking and monitoring the output power at $1.0\ \mu\text{m}$ it was ensured that as much power as possible was launched into the core. Measurements without any pump light revealed that the coupling efficiency for the co-seed light into the fiber core was around 80% . Dichroic mirrors at both ends of the fiber were used to combine and separate the pump, seed, and co-seed light. In order to minimize problems with any heating of the fiber, the whole fiber was coiled on a conductive heatsink, which had a diameter of $30\ \text{cm}$. In addition, the pump launch end of the fiber was held by a water cooled copper block, which was connected directly to the heatsink.

4.1.2 Influence of the Co-Seeding Parameters

As mentioned, the co-seeding method can not only be used to suppress parasitic processes at $1.0\ \mu\text{m}$, but it also potentially increases the efficiency at $1.5\ \mu\text{m}$ by reabsorption of the amplified co-seed. Thus, to investigate which co-seeding parameters are the best to get the maximum benefit from both advantages, some preliminary measurements have been performed prior to the power scaling experiments.

First, a fraction of the power of the (with respect to the pump light direction) backward propagating Yb^{3+} -ASE was measured in dependency of the co-seeding wavelength and power for a fixed pump power of 25 W. Because parasitic processes at $1.0\ \mu\text{m}$ are directly related to the actual power of the Yb^{3+} -ASE, the possibility of parasitic processes is minimized for a maximized suppression of the Yb^{3+} -ASE. The corresponding results are presented in Figs. 4.4 (a) and 4.4 (b). As indicated by Fig. 4.4 (a), the best suppression of the Yb^{3+} -ASE was achieved for a co-seeding wavelength between 1045 nm and 1060 nm, depending on the actual power of the co-seed. At a maximum co-seeding power of 2 W the best suppression of the Yb^{3+} -ASE was achieved for a co-seeding wavelength of 1050 nm, see Fig. 4.4 (b).

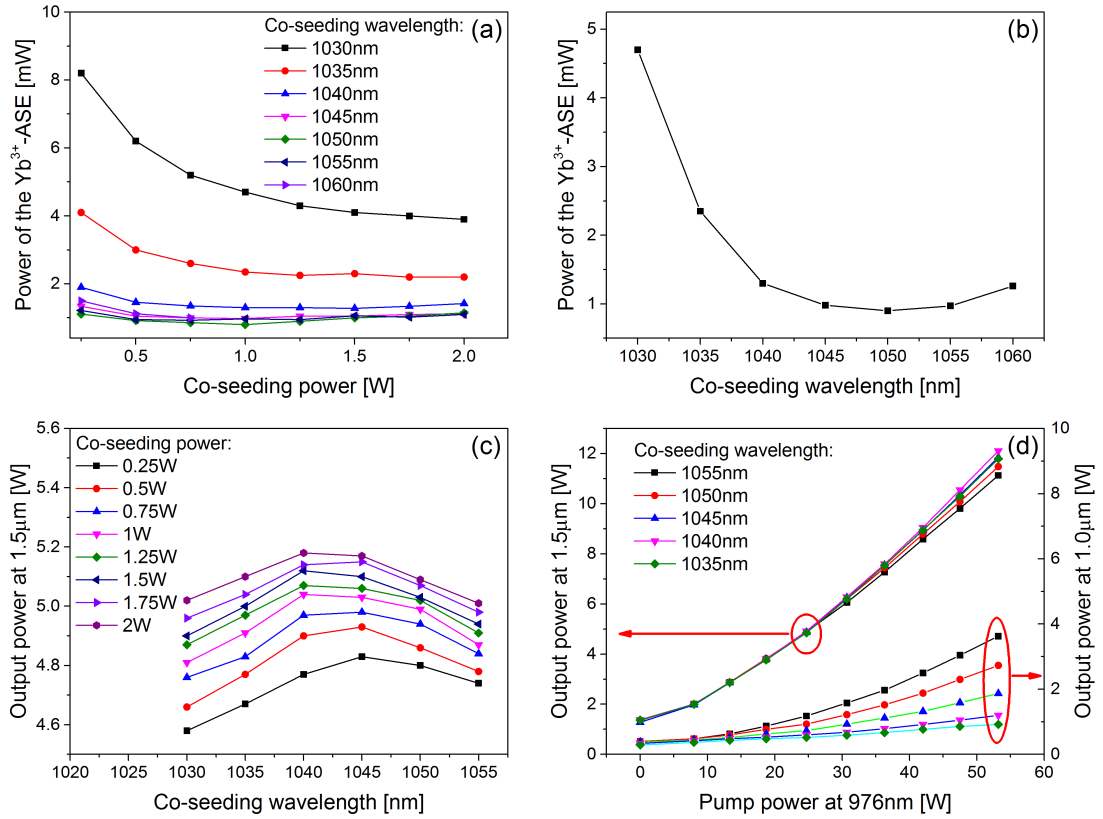


Figure 4.4: (a): Power of the backward propagating Yb^{3+} -ASE of the single-frequency $\text{Er}^{3+}:\text{Yb}^{3+}$ -codoped triple-clad LMA fiber amplifier in dependency of the co-seeding power and wavelength (25 W pump power). (b): Power of the Yb^{3+} -ASE in dependency of the co-seeding wavelength for a fixed co-seeding power of 2 W and a pump power of 25 W. (c): Output power at $1.5\ \mu\text{m}$ at 25 W of pump power for different co-seeding power levels and wavelengths. (d): Amplifier slopes at $1.0\ \mu\text{m}$ and $1.5\ \mu\text{m}$ for different co-seeding wavelengths with a co-seeding power of 2 W.

Next, the dependency of the amplifier efficiency at 1.5 μm on the co-seeding wavelength and power was analyzed. For this, the amplified output power at 1.5 μm at a given pump power of 25 W was monitored for different co-seeding parameters, see Fig. 4.4 (c). The optimal co-seeding wavelength was around 1040 nm with a corresponding power of 2 W. The slopes of the amplified 1.5 μm seed and 1.0 μm co-seed for a fixed co-seeding power of 2 W, see Fig. 4.4 (d), also suggested that a co-seeding wavelength around 1040 nm was the best to achieve as much efficiency as possible at 1.5 μm .

Although the influence of the co-seeding wavelength on the output power and slope efficiency at 1.5 μm was studied in detail [Han11; Kuh10a; Sli13], only in [Sli13] it was also studied experimentally how the actual co-seeding power influences the 1.5 μm signal. The authors observed only a small influence of the co-seeding power on the output power at 1.5 μm and they also reported that for some co-seeding wavelengths an increase in co-seeding power led to a decrease of power at 1.5 μm . Such a behavior was not observed in the present experiments. In addition, a quite significant dependency of the power at 1.5 μm on the co-seeding power was observed, see Fig. 4.4 (c). Most probably, this is explained by the fact that the present experiments were performed at significantly higher co-seeding and output power levels.

As mentioned, the highest increase of output power at 1.5 μm was achieved with a co-seeding wavelength of 1040 nm. However, for all experiments presented in the following, the co-seed laser was tuned to 1050 nm with an output power of 2 W in order to achieve the highest possible suppression of the Yb³⁺-ASE, i.e. parasitic processes at 1.0 μm .

4.1.3 Power Scaling Experiments

The final results of the power scaling experiments, i.e. the amplifier slopes at 1.0 μm and 1.5 μm , are presented in Fig. 4.5 (a). At a maximum absorbed pump power of 210 W a maximum output power of 61 W at 1.5 μm was obtained. The corresponding slope efficiency with respect to the absorbed pump power was around 30 %. In addition, no decrease of the slope efficiency at high pump power levels was observed like it normally occurs in experiments without a co-seed due to an excessively increasing Yb³⁺-ASE [Jeo05; Jeo07]. At 1.0 μm a maximum output power of 40 W with a slope efficiency of around 23% was measured. Thus, the Er³⁺:Yb³⁺-codoped triple-clad fiber was still not long enough to reabsorb all the amplified co-seed power, whereas more than 98 % of the pump light was absorbed. The optical spectrum of the amplified 1.5 μm signal at the highest obtained output power, see Fig. 4.5 (b), reveals a peak-to-ASE suppression of around 50 dB (0.5 nm resolution bandwidth (RBW)). In addition, the inset in Fig. 4.5 (b) shows the spectrum of the amplified co-seed at an absorbed pump power of 200 W and reveals a corresponding

peak-to-ASE suppression of 40 dB (0.5 nm RBW).

Unfortunately, during all power scaling experiments and especially at pump power levels of more than 150 W, problems regarding the stability of the in-coupling of the co-seed light into the fiber occurred randomly from time to time. Most probably, this behavior was induced by thermal misalignments of the fiber tip at the pump and co-seed launch end. This effect could not be avoided completely, although the mounting of the fiber was carefully designed. Consequently, each individual attempt to scale the output power was finally limited by the onset of spiking and self-lasing at 1.0 μm . Indeed, the results presented above were also limited by this effect and represent the best result that was achieved in a series of attempts to scale the output power of the $\text{Er}^{3+}:\text{Yb}^{3+}$ -codoped triple-clad LMA fiber amplifier. However, as this behavior was certainly only induced by thermal misalignments, it does not represent a general limitation of the co-seeding approach and in an all-fiber system, for example, such problems can be avoided, most probably.

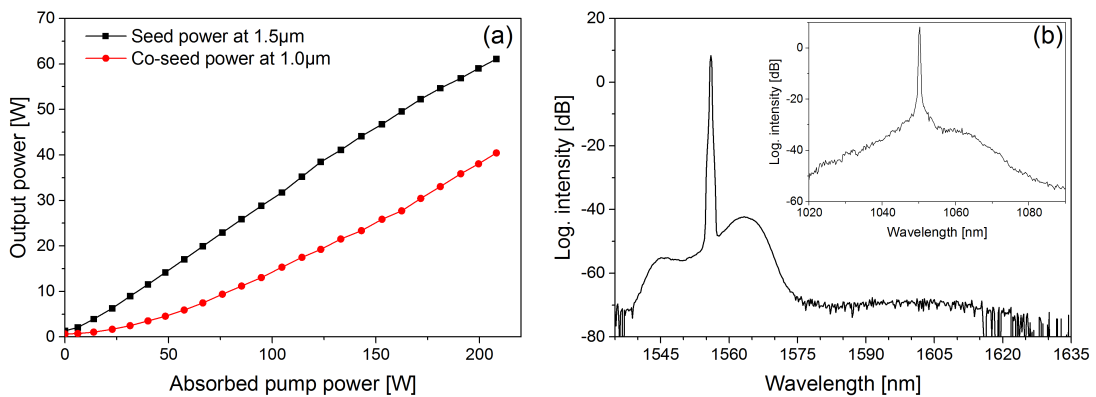


Figure 4.5: (a): Amplifier slopes at 1.0 μm and 1.5 μm of the single-frequency $\text{Er}^{3+}:\text{Yb}^{3+}$ -codoped triple-clad LMA fiber amplifier. (b): Spectrum at 1.5 μm at the highest amplifier output power. Inset: Spectrum at 1.0 μm at an absorbed pump power of 200 W.

4.1.4 Beam Quality Measurements

Because interferometric GWDs require a pure TEM_{00} mode, the common technique of measuring the M^2 -value as a characterization of the beam quality is not sufficient. For example, even an M^2 -value of < 1.1 can correspond to a higher order mode content of 30% [Wie07]. Instead, the beam quality in terms of the TEM_{00} mode content, i.e. the overlap with a pure TEM_{00} mode, is typically measured with a non-confocal scanning ring cavity as it is depicted schematically in Fig. 4.6. By design, the eigenmodes of such a cavity are TEM modes. Thus, a decomposition into a set of TEM modes can be achieved by scanning the cavity length and monitoring the transmitted signal. Then, by fitting a TEM

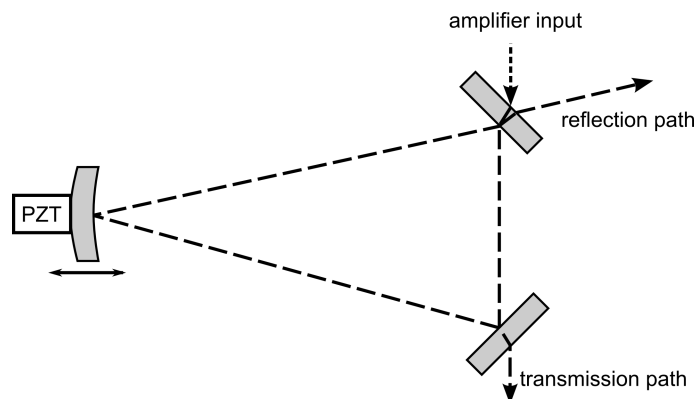


Figure 4.6: Schematic overview of the non-confocal scanning ring cavity that was used for the TEM_{00} mode content measurements on the single-frequency $\text{Er}^{3+}:\text{Yb}^{3+}$ -codoped triple-clad LMA fiber amplifier. PZT: piezoelectric transducer.

mode set to the transmitted signal, the TEM_{00} mode content can be calculated. A more detailed description of the mode of operation of such a non-confocal scanning ring cavity can be found in [Kwe07]. The cavity used for all experiments presented in the following had a free spectral range of 714 MHz. Since the actual finesse of such cavities always depend on the polarization, the maximum finesse of about 285 (specified at 1535 nm) was obtained with a linearly p-polarized input beam. Scanning of the cavity was achieved by injecting a ramp signal to the piezoelectric transducer that acted as a mount for one of the mirrors. As the photodiode behind the cavity required an input power level of around 100 mW, an optical wedge was used to sample a fraction of the amplified seed signal. Subsequently, the polarization was controlled by a quarter-wave plate, a half-wave plate, and a polarizing beamsplitter cube. Then, the power was adjusted with an additional half-wave plate and a second polarizing beamsplitter cube.

The actual beam quality measurements, i.e. the measurements of the TEM_{00} mode content, were performed at different output power levels of the $\text{Er}^{3+}:\text{Yb}^{3+}$ -codoped triple-clad fiber amplifier. The corresponding results are presented in Fig. 4.7 (a). In addition, the actual mode scan, i.e. the normalized cavity transmission at the highest obtained output power of 61 W, is presented in Fig. 4.7 (b). The fundamental TEM_{00} mode content was more than 90 % at all amplifier output power levels and 91 % at the maximum output power. Note that the alignment to the scanning ring cavity had to be optimized for each measurement, although the analysis presented in the last section of this chapter indicates that this is a problematic approach. This was necessary as the mentioned random thermal misalignment also led to a quite significant misalignment of the input beam to the cavity that was most probably not related to a corresponding change of beam quality.

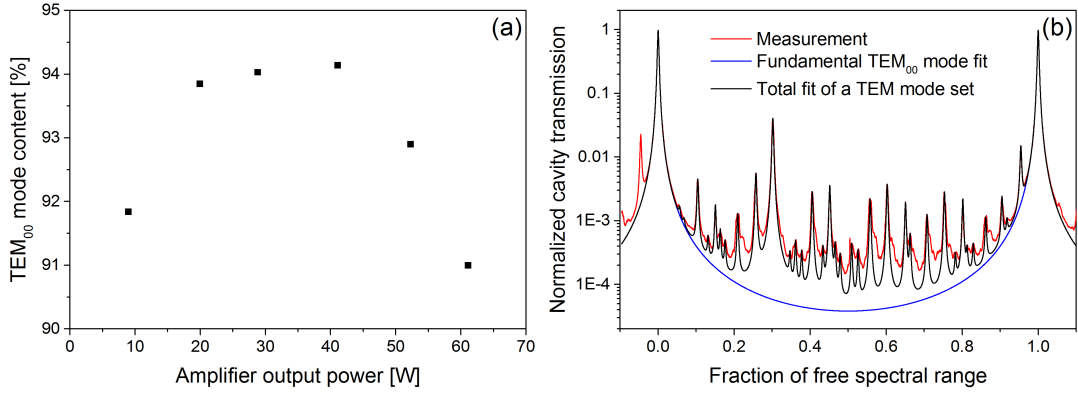


Figure 4.7: (a): Fundamental TEM_{00} mode content of the single-frequency $\text{Er}^{3+}:\text{Yb}^{3+}$ -codoped triple-clad LMA fiber amplifier at different output power levels. (b): Transmitted signal of the non-confocal scanning ring cavity at the highest obtained amplifier output power of 61 W with a corresponding fit of a TEM mode set.

4.1.5 Comparison and Conclusion

As mentioned, the theoretical overlap of this fiber's LP_{01} mode with a TEM_{00} mode is 99.7%. Thus, the measured TEM_{00} mode contents of more than 90% indicate a strong tendency towards but not pure single-mode operation of the $\text{Er}^{3+}:\text{Yb}^{3+}$ -codoped triple-clad LMA fiber. However, in particular compared to previous similar investigations of $\text{Er}^{3+}:\text{Yb}^{3+}$ -codoped [Kuh10b] and Er^{3+} -doped single-frequency LMA fiber amplifiers [Kuh11b], the performance of the novel $\text{Er}^{3+}:\text{Yb}^{3+}$ -codoped triple-clad fiber with respect to the power scaling experiments and beam quality measurements was excellent. As mentioned earlier, the $\text{Er}^{3+}:\text{Yb}^{3+}$ -codoped MFC fiber that was analyzed in [Kuh10b] provided a TEM_{00} mode content of more than 90%, but the maximum output power of 8.5 W at 1.5 μm was limited by a thermal failure of the silicone rubber coating. The commercially available $\text{Er}^{3+}:\text{Yb}^{3+}$ -codoped triple-clad LMA fibers that have been also analyzed in [Kuh10b] provided output power levels of more than 20 W but TEM_{00} mode contents as low as 80%. The Er^{3+} -doped PCF with a core diameter of 40 μm and a NA smaller than 0.04 that was analyzed in [Kuh11b] provided a high output power of 70 W, comparable to the maximum output power of 61 W obtained in the experiments with the novel $\text{Er}^{3+}:\text{Yb}^{3+}$ -codoped triple-clad LMA fiber. However, due to pointing instabilities the beam quality measurements with the Er^{3+} -doped PCF could only be performed up to an output power of 50 W and the corresponding fundamental mode content was as low as 80%.

In conclusion, the presented $\text{Er}^{3+}:\text{Yb}^{3+}$ -codoped triple-clad fiber is a promising candidate for single-frequency LMA fiber amplifiers at 1.5 μm because it provided an excellent beam

quality and good power scaling capabilities. In addition, the presented power scaling experiments and results indicate that the co-seeding method is very suitable to scale the output power of single-frequency $\text{Er}^{3+}:\text{Yb}^{3+}$ -codoped fiber amplifiers towards the 100 W level by suppressing parasitic processes at 1.0 μm and by increasing the efficiency at 1.5 μm due to reabsorption of the co-seed.

4.2 Passive Leakage Channel Fiber

Due to the typical infrastructure of GWDs the laser source, e.g. a high-power fiber amplifier like it was studied in the last section, and the actual interferometer are separated spatially. However, the laser beam can be delivered to the interferometer for example by a passive delivery fiber. Obviously, such a passive delivery fiber must maintain an excellent beam quality, i.e. a high TEM_{00} mode content. In addition, as high power levels are propagating in the fiber core, the passive delivery fiber is prone to SBS. As the SBS process imprints additional broadband relative intensity noise (RIN) on the laser signal [Hor97], it potentially affects the sensitivity of the interferometer. Thus, the onset of SBS not only in the laser source but especially in the passive delivery fiber must be avoided under all circumstances. Hence, a passive delivery fiber is required that offers single-mode operation with a corresponding high TEM_{00} mode content and a large core, i.e. a large mode-field diameter, to suppress SBS. In addition, if the passive delivery fiber relies on the same fiber design as the actual high-power fiber amplifier, it can be spliced directly to the output of the fiber amplifier and lossy free-space couplings can be avoided, most probably. Furthermore, as next-generation GWDs will most probably utilize laser sources at 1.0 μm and 1.5 μm , a single fiber design for both wavelengths would be advantageous.

If single-mode operation is required, the core size of a conventional passive step-index fiber cannot be increased arbitrarily because the smallest adjustable core NA during the MCVD preform fabrication is ~ 0.06 . In addition, as mentioned in the last section, the bend-induced filtering of higher order modes in few-mode step-index fibers becomes more and more inefficient with increasing core size. A well-studied concept to overcome these limitations are microstructured fibers, i.e. photonic crystal fibers (PCFs) [Kni96]. In such fibers the core is surrounded and formed by an array of air holes, typically arranged in a triangular pattern. Wave-guidance in PCFs can be understood by an effective index model as the array of air holes has a lower refractive index than the core area. Corresponding single-mode LMA PCFs allow for core sizes that are not feasible with the step-index design. However, with increasing core size single-mode PCFs are more and more challenging to fabricate as the index of the core must be controlled very precisely and the bending loss for the fundamental mode also increases more and more. The latter is for example the reason

why active Yb^{3+} -doped single-mode LMA PCFs are limited to a maximum core diameter of around $40\ \mu\text{m}$ [Lim04]. PCFs with larger core diameters are typically only produced as rigid and inflexible rods [Lim05].

In recent years different novel bendable few-mode LMA fiber concepts with built-in filtering techniques for the higher order modes have been developed. These concepts promise single-mode operation and large core sizes that are not feasible with step-index fibers or PCFs. Of particular interest are all-solid designs, i.e. designs that do not include air-holes or air-claddings such as most PCFs, as it should be possible to utilize standard techniques to splice such fibers to each other or to conventional step-index fibers. A corresponding example are chirally-coupled-core (CCC) fibers [Ma11]. They consist of a conventional step-index structure, but the core is additionally chirally surrounded by one or more satellite cores. By choosing the correct helix parameters a phase-matching between the higher order modes in the core and the modes in the satellite core(s) is achieved. Consequently, the higher order modes are “pulled” out of the core, which then only guides the fundamental mode. In particular a passive CCC fiber with a core diameter of $55\ \mu\text{m}$ and a core NA of 0.07 has already been characterized with respect to the TEM_{00} mode content at $1064\ \text{nm}$ [Kar12b]. The analyzed sample provided nearly single-mode operation, i.e. a TEM_{00} mode content of more than 95 %, even for a misaligned in-coupling. Thus, it is a promising candidate as a passive delivery fiber at $1.0\ \mu\text{m}$ in GWDs. However, Yb^{3+} -doped CCC fibers that have been analyzed in [Kar13b] and [Kar13a] revealed either quite significant limitations regarding the obtainable output power or the beam quality, i.e. the TEM_{00} mode content. Thus, as stated in [Kar13a], a final conclusion with respect to the suitability of the CCC fiber design for applications at $1064\ \text{nm}$ in GWDs cannot yet be drawn. In addition, Er^{3+} -doped or $\text{Er}^{3+}:\text{Yb}^{3+}$ -codoped CCC fibers have not yet been fabricated. Thus, it remains to be investigated if this fiber design is suitable for high-power single-frequency LMA fiber amplifiers at $1.5\ \mu\text{m}$.

Another promising example for an all-solid LMA fiber design with built-in suppression of the higher order modes are weakly-guiding fibers, i.e. leakage channel fibers (LCFs). In early LCFs the core area was surrounded and formed by an array of large air holes [Don07]. However, due to the large diameter of the air holes these fibers were very impractical. A solution was found in the form of all-solid LCFs in which the air holes have been replaced by fluorine-doped rods because the fluorine-doping also leads to a lower refractive index than that of fused silica [Don09b]. Similar to PCFs, wave-guidance in LCFs can be understood by total internal reflections at the effective refractive index step between the core area and the array of the fluorine-doped rods. However, by design all guided modes in LCFs are leaky, i.e. they experience quite large propagation losses. Nevertheless, effective

single-mode operation can be obtained by choosing an appropriate refractive index, size, and spacing of the fluorine-doped rods as this leads to a significantly smaller propagation loss of the fundamental LP_{01} mode compared to the higher order modes. Most practical LCFs support only the fundamental LP_{01} mode and the two LP_{11} modes, which have the same intensity pattern but distinct orientations. Furthermore, resonantly enhanced leakage channel fibers (Re-LCFs) utilize non-uniform layers of fluorine-doped rods and exploit a bend-induced resonance between the LP_{11} modes and the cladding structure to increase the loss for the LP_{11} modes even further [Bar12]. Most theoretical investigations of LCFs rely on the assumption of an infinite cladding. Especially for double clad fibers with a well defined refractive index step between the cladding and the coating this approximation is questionable. Indeed, theoretical investigations [Don09a] have confirmed that a circular shaped cladding leads to coherent reflections at the cladding-to-coating boundary and a re-localization of the higher order modes in the core area. However, it was also shown experimentally [Gu13] that these coherent reflections can either be suppressed by coiling the fiber or by using a hexagonally shaped cladding.

Experimentally, the composition of the output beam profile of a particular 50 μm core Re-LCFs with respect to the LP fiber modes at 1.0 μm and 1.5 μm has been analyzed with the S^2 technique [Jol13]. This approach is based on spectrally and spatially resolving the mode interference of a broadband signal that is transmitted passively through the fiber [Nic08]. The results indicate that the investigated fiber sample provided single-mode operation at both wavelengths. However, no measurements of the TEM_{00} mode contents of LCFs at 1.0 μm and 1.5 μm , which are essential for passive delivery fibers in GWDs, have been performed, so far.

4.2.1 Fiber Design

The actual beam quality measurements have been performed with a 2.2 m long double-clad Re-LCF that was kindly provided by Prof. Liang Dong from the Clemson University (Clemson, SC, USA). A cross-section of the fiber is presented in Fig. 4.8. Except for the hexagonally shaped cladding the fiber was quite similar to the sample that was used for the mentioned S^2 measurements in [Jol13]. The refractive index of the fluorine-doped rods surrounding the core was 0.0155 below that of fused silica and the fiber was originally designed to work at a coiling diameter of around 40 cm at 1050 nm. The core diameter was 50.9 μm at its smallest dimension, 51.3 μm at its largest dimension and the cladding diameter was 426 μm (flat-to-flat).

Prior to any measurements, the refractive index profile of the Re-LCF was modeled in a commercially available software (COMSOL) in the group of Prof. Dong and the

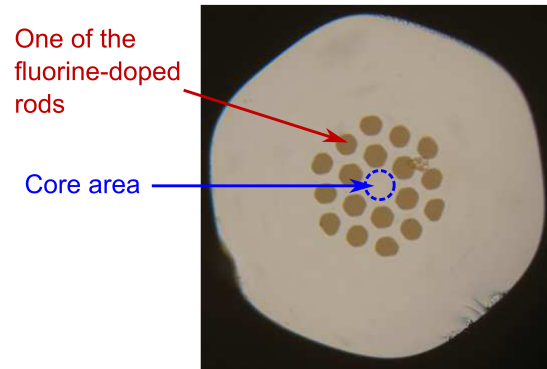


Figure 4.8: Cross section of the hexagonal shaped Re-LCF that was used to measure the beam quality, i.e. the TEM_{00} mode content, of this fiber type at $1.0\ \mu\text{m}$ and $1.5\ \mu\text{m}$.

Helmholtz-equation was solved by the built-in finite-element solver on a corresponding 2D mesh in order to obtain the E-field distributions of the LP_{01} and the LP_{11} modes at $1064\ \text{nm}$ and $1550\ \text{nm}$ [Gu14]. Afterwards, the E-field distributions of the fundamental LP_{01} modes at $1064\ \text{nm}$ and $1550\ \text{nm}$ were used to calculate the maximum possible TEM_{00} mode contents for the case that only the LP_{01} modes are guided by the Re-LCF. This was done by mapping the calculated intensity distribution of each LP_{01} mode to a 2D grid and by fitting the offset and the beam diameter of a pure TEM_{00} mode to it. The fit parameters were optimized numerically until the overlap integral between both modes was maximized. Note that this overlap is equal to the TEM_{00} mode content if the correct normalization is applied. For the particular Re-LCF, a maximum possible TEM_{00} mode content of 98.2% at $1064\ \text{nm}$ and 98.3% at $1550\ \text{nm}$ was calculated.

4.2.2 Beam Quality Measurements at $1.0\ \mu\text{m}$ and $1.5\ \mu\text{m}$

The experimental setup that was used to measure the TEM_{00} mode content of the Re-LCF is presented in Fig. 4.9. Either a single-frequency NPRO (Mephisto, Innolight/Coherent (Santa Clara, CA, USA)) at $1064\ \text{nm}$ or the pre-amplified single-frequency fiber laser at $1556\ \text{nm}$ acted as a test laser for passive transmission through the fiber. At both wavelengths, mode matching to the corresponding fundamental LP_{01} mode of the fiber was performed with two lenses ($f=120\ \text{mm}$ and $f=8\ \text{mm}$). An additional lens ($f=12\ \text{mm}$) was used to collimate the light at the output end of the fiber. In order to suppress any light guided by the cladding of the fiber, high index gel was applied to both ends of the fiber over a length of around $6\ \text{cm}$. In addition, a pinhole blocking any residual cladding light was used at the output end of the fiber. The actual measurements of the TEM_{00} mode content at $1556\ \text{nm}$ were performed with the same non-confocal scanning ring cavity

that was introduced beforehand in section 4.1.4. The measurements of the TEM_{00} mode contents at 1064 nm were performed with a similarly constructed cavity that had a free spectral range of 715 MHz and a finesse of about 200 at 1064 nm (p-polarization).

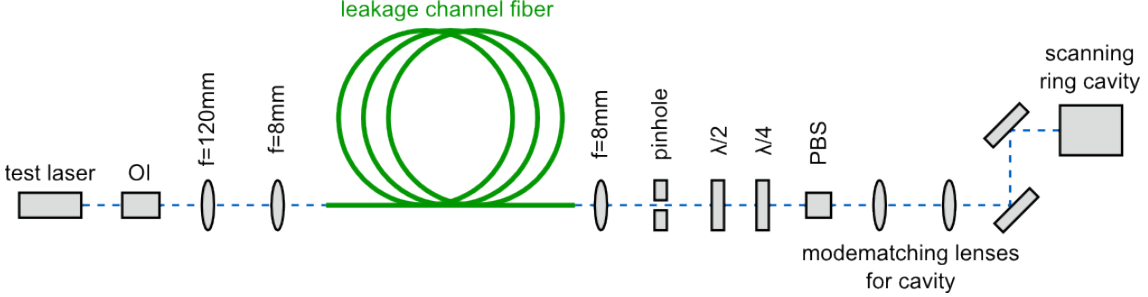


Figure 4.9: Experimental setup for the measurements of the TEM_{00} mode content of the passive Re-LCF at 1.0 μm and 1.5 μm . OI: optical isolator, PBS: polarizing beam splitter.

At both wavelengths, the TEM_{00} mode content measurements were performed for two different coiling diameters of 50 cm and 60 cm. For such coiling diameters the tested Re-LCF provides a fundamental LP_{01} mode loss at 1064 nm in the order of 1 dB/m, whereas the loss for the higher LP_{11} mode is in the order of 10 dB/m [Gu13]. The results of the measurements are presented in Tab. 4.1. At 1556 nm the measured TEM_{00} mode content was 98.14 % (50 cm coiling diameter) and 98.17 % (60 cm coiling diameter) and at 1064 nm the measured TEM_{00} mode content was 97.57 % (50 cm coiling diameter) and 97.50 % (60 cm coiling diameter). Compared with the theoretically obtained values for the case of pure LP_{01} modes these results indicate that the Re-LCF provided pure single-mode operation at both wavelengths.

Table 4.1: Measured and calculated TEM_{00} mode contents of the passive Re-LCF at 1064 nm and 1556 nm for different coiling diameters.

Note	1064 nm	1556 nm
50 cm coiling diameter	97.57 %	98.14 %
60 cm coiling diameter	97.70 %	98.17 %
calculated theoretical limit	98.20 %	98.30 %

In order to investigate how the beam quality reacts to any misalignment of the in-coupling, additional measurements were performed. Prior to each of these additional measurements, the in-coupling of the corresponding test laser into the Re-LCF was changed such that 5 % less power was transmitted through the fiber. However, the alignment to the corresponding scanning ring cavity was not changed, in particular with respect to the results that are presented in the next section. These experiments revealed a quite different behavior at both wavelengths. At 1064 nm a TEM_{00} mode content of around 97.4-97.5 %

was measured. Thus, the misalignment almost did not change the TEM_{00} mode content. However, at 1550 nm the misalignment led to a significantly lower TEM_{00} mode content of less than 90 %. In addition, at 1064 nm a higher amount of cladding-light was observed on a corresponding IR-card after the misalignment and at 1556 nm such behavior was not observed. This effect is most probably explained by a stronger suppression of the LP_{11} mode at 1064 nm in comparison with the suppression at 1556 nm, in particular as the fiber was originally designed to work at 1050 nm.

4.2.3 Conclusion

At 1064 nm the measured TEM_{00} mode content of more than 97 %, even with a misaligned in-coupling, indicates true single-mode operation of the Re-LCF. However, at 1556 nm the tested sample provided a TEM_{00} mode content of more than 98 %, i.e. single-mode operation, only for an optimized in-coupling. Misalignment led to an excitation of higher order modes. Nevertheless, as the fiber was originally designed to work at 1050 nm, the performance at 1.5 μm can be certainly improved by an optimized fiber design. Thus, the Re-LCF concept is a promising candidate for passive delivery fibers in GWDs not only at 1.0 μm but also at 1.5 μm .

So far, only Yb^{3+} -doped LCFs have been fabricated and investigated. The performance of these fibers, e.g. the obtainable slope efficiencies in laser configuration, are quite comparable to the performance of conventional Yb^{3+} -doped step-index fibers, see for example [Kon13]. However, Er^{3+} -doped or $\text{Er}^{3+}:\text{Yb}^{3+}$ -codoped LCFs have not yet been fabricated. In addition, it is questionable if $\text{Er}^{3+}:\text{Yb}^{3+}$ -codoped LCFs are technically feasible. The reason is that the core of a LCF must have the same (or lower) refractive index than the fused silica background, i.e. the area around the fluorine-doped rods. The necessary codoping with phosphor, which suppresses the energy back-transfer from Er^{3+} to Yb^{3+} , would raise the refractive index of the core significantly. Thus, it would require laborious and expensive compensation of the refractive index of the fused silica background.

4.3 Beam Quality Measurements on Few-Mode Large Mode Area Fibers

The decomposition of a given beam profile into a set of TEM modes by a scanning ring cavity is the most commonly used method to determine the TEM_{00} mode content in the context of laser sources for GWDs, see for example [Kar12a; Kuh10b]. However, in particular for beam profiles that correspond to few-mode LMA fibers, i.e. fibers that support higher order modes, some care must be taken when the TEM_{00} mode content is determined by this method. In the following, numerical data for the E-field distributions of the fundamental LP_{01} mode and one of the LP_{11} modes at 1064 nm of the Re-LCF, which

was investigated in the last section, are used to highlight the critical points. Note that these modes only act as an example and that the methodology and the results are similar for any other few-mode LMA fiber.

As explained in the last section, the TEM_{00} mode content of the fundamental LP_{01} mode can be determined by fitting a pure TEM_{00} mode to it, i.e. by maximizing the overlap between both modes. A small additional in-phase LP_{11} mode content that is added to the LP_{01} mode results in a laterally shifted beam profile. If again a TEM_{00} mode is fitted to this beam profile, the result still corresponds to a comparably high TEM_{00} overlap but with an adaption of the TEM_{00} center position. Thus, for the case of a complete decomposition into a set of TEM modes, e.g. by a non-confocal scanning ring cavity, this result refers to a different TEM mode set.

As the intensity profile of any modal superposition depends on the relative phases of the involved modes, any fit of a TEM_{00} mode to such a modal superposition and the subsequent evaluation of the TEM_{00} mode content is only valid for a fixed phase relationship between the different modes. Because in any real few-mode fiber the phase relationship between the modes is not fixed necessarily but changes with time, the TEM_{00} mode content, determined by the overlap with a fixed TEM_{00} mode, also changes with time. Even if the change is very slow, e.g. due to thermal effects, this has already a high impact for GWDs as they have to run reliably 24 hours a day for long time periods. Indeed, the fitting procedure could be repeated instantaneously every time the modal phase distribution changes, but this is hard to realize experimentally. Only if the TEM mode set obtained by a fit to a pure

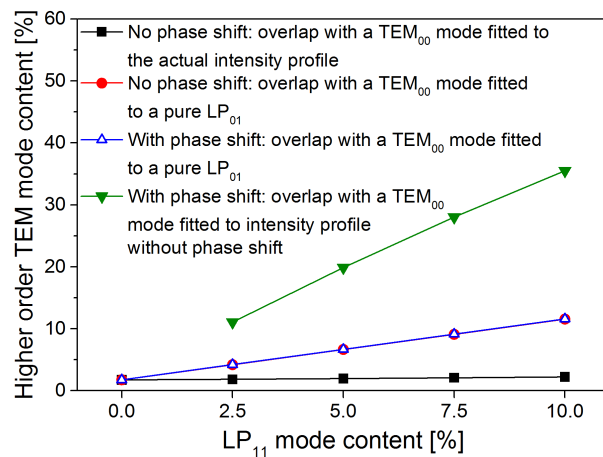


Figure 4.10: Numerically obtained TEM_{00} mode content of beam profiles that correspond to the investigated Re-LCF in dependency of the actual LP_{11} mode content (see text for further explanation).

LP₀₁ mode is also used for the analysis of the composed beam, the TEM₀₀ content becomes independent of the relative phases, as it is proven by the numerical results presented in Fig. 4.10. Here, the LP₁₁ mode content was increased stepwise, a TEM₀₀ mode was fitted to the corresponding beam profile, and the overlap with the TEM₀₀ mode was calculated (black data points). In a second step, the LP₁₁ mode content was increased stepwise again but with an additional relative phase shift of π and the TEM₀₀ mode content was evaluated with the identical reference mode set (green data points). Because the additional phase shift results in a lateral shift of the beam, which is not accounted for in the choice of reference mode, the overlap calculation results in a strongly reduced TEM₀₀ mode content. Finally, the overlap of the beam profile with and without the additional relative phase shift with a TEM₀₀ mode, which was fitted beforehand to the pure LP₀₁ mode, was calculated (blue and red data points, respectively). It can be seen that, as pointed out above, only for this choice of reference mode set, the TEM₀₀ mode overlap is independent of the relative phases of the modes. This fact must be considered carefully when the TEM₀₀ overlap of few-mode fibers that support higher order modes is determined experimentally by a non-confocal scanning ring cavity.

CHAPTER 5

Gain Dynamics of $\text{Er}^{3+}:\text{Yb}^{3+}$ -Codoped Fiber Amplifiers

While the previous chapter was dealing with the power scaling of single-frequency $\text{Er}^{3+}:\text{Yb}^{3+}$ -codoped fiber amplifiers, the present chapter is dedicated to the temporal dynamics of $\text{Er}^{3+}:\text{Yb}^{3+}$ -codoped fiber amplifiers, in particular with respect to a possible application in next-generation GWDs.

As it is explained in more detail in the following section, understanding the temporal and in particular the gain dynamics of laser sources in GWDs is quite important for several reasons. The gain dynamics of Yb^{3+} - and Er^{3+} -doped fiber amplifiers have already been studied in great detail [Nov02a; Nov02b], in particular with respect to a possible application in GWDs [Tün12c]. In addition, the gain dynamics of $\text{Er}^{3+}:\text{Yb}^{3+}$ -codoped glass lasers have been investigated for CW [Tac98] and pulsed [Sch04] operation. However, a corresponding analysis regarding CW $\text{Er}^{3+}:\text{Yb}^{3+}$ -codoped fiber amplifiers was missing, so far. Therefore, the gain dynamics, i.e. the response of the output power of $\text{Er}^{3+}:\text{Yb}^{3+}$ -codoped fiber amplifiers to pump or seed power fluctuations, have been analyzed theoretically and experimentally in the frame of this thesis for the first time. The corresponding results are presented in the first part of this chapter and, as will be shown, a full analytical solution does not exist. Thus, a numerical simulation was developed that allowed to study the gain dynamics of an exemplary $\text{Er}^{3+}:\text{Yb}^{3+}$ -codoped fiber amplifier in more detail. A qualitative comparison of numerically and experimentally obtained results indicate good agreement. In addition, the experimental results allowed to obtain the transfer function of the Yb^{3+} -to- Er^{3+} energy transfer for the first time.

The second part of this chapter is dedicated to the coupling of the optical phase of the output signal of $\text{Er}^{3+}:\text{Yb}^{3+}$ -codoped fiber amplifiers to power fluctuations of the pump diodes via thermal effects and via the inversion, i.e. the gain in combination with the Kramers–Kronig relation (KKR). This is of particular interest for coherent beam combining

schemes as controlling the actual phases of the individual amplifiers is indispensable and utilizing the pump diodes is a very simple and elegant way to do so. Hence, within the frame of this thesis the dynamical response of the optical phase of the output signal of an exemplary $\text{Er}^{3+}:\text{Yb}^{3+}$ -codoped fiber amplifier to pump power modulations has been investigated experimentally with a fiber-based Mach-Zehnder interferometer for the first time. However, in contrast to similar investigations of Yb^{3+} -doped fiber amplifiers [Tün12b; Tün12c], a final and complete evaluation of the obtained results is not possible. Most probably, this is because additional loss-mechanisms such as up-conversion or secondary energy-transfer and corresponding additional energy states also contribute significantly to the total optical phase shift via thermal effects or via the KKR.

Part of the work and the results presented in this chapter have been published beforehand in [Ste15a].

5.1 Transfer Functions of Pump and Seed Power Noise

As the sophisticated power stability requirements of GWDs cannot be fulfilled by free running lasers and consequently also not by fiber amplifiers in MOPA configuration, an external stabilization is indispensable. However, the initial power noise properties of the laser source, e.g. a high-power single-frequency $\text{Er}^{3+}:\text{Yb}^{3+}$ -codoped fiber amplifier like it was presented in the previous chapter, are not negligible as higher noise levels also require better control loops. Besides other contributions, e.g. variations in the spectrum of the pump diode, i.e. spectral pump noise, a major contribution to the amplifier power noise are seed and pump power fluctuations. Thus, it is quite important to understand how power noise from the pump or the seed laser couples via the inversion, i.e. the gain, to the output signal of an $\text{Er}^{3+}:\text{Yb}^{3+}$ -codoped fiber amplifier. Furthermore, as it is explained in the following paragraph, detailed knowledge of the dynamic system response to pump power fluctuations might also enable novel techniques to stabilize the output power of fiber amplifiers in GWDs.

In the current generation of GWDs the actual power stabilization is performed by a control loop that utilizes an external acousto-optic modulator (AOM) to dynamically dump a fraction of the total power. However, other approaches are more attractive. For example, the power stabilization could be realized by a feedback to the pump diodes of the laser source. Indeed, such an approach would still need a dynamic power reserve, but it does not require the additional AOM. However, as mentioned, such an approach requires a detailed knowledge about the dynamic response of the laser system to pump power fluctuations.

The gain dynamics of fiber amplifiers are most commonly analyzed by means of the complex transfer functions of the system, i.e. the frequency-dependent magnitude and

phase response of the output power to a sinusoidal modulation of the pump or seed power. The transfer functions determine how noise from the pump or the seed laser couples to the output power of the amplifier. Fortunately, the transfer functions of Yb^{3+} - and Er^{3+} -doped fiber amplifiers are given by analytical expressions [Nov02b]. The pump-to-signal transfer function is given by a low-pass

$$\frac{m_s^{(p)}}{m_p} e^{i\phi_s^{(p)}} = \frac{B_s (P_{p,0}(z=0) - P_{p,0}(z=L))}{\omega_{\text{eff}} + i\omega} \quad (5.1)$$

like it is depicted schematically in Fig. 5.1. The magnitude $m_s^{(p)}/m_p$ is given by the ratio of the induced modulation depth $m_s^{(p)}$ of the signal and the initial modulation depth m_p of the pump power modulation. Furthermore, the phase $\phi_s^{(p)}$ corresponds to the phase shift of the induced modulation of the signal with respect to the initial pump power modulation. Note that throughout the whole chapter a subscripted 0 indicates the non-modulated steady state values, e.g. $P_{p,0}(z=0)$ is the steady state pump power at the beginning of the fiber ($z=0$). Also note that $z=L$ corresponds to the end of the fiber. The cut-off frequency

$$\omega_{\text{eff}} = B_s P_{s,0}(z=L) + B_p P_{p,0}(z=L) + \frac{1}{\tau}. \quad (5.2)$$

of the low-pass is related to the output power and residual pump power of the amplifier, i.e. $P_{s,0}(z=L)$ and $P_{p,0}(z=L)$, and the lifetime τ of the corresponding upper energy state.

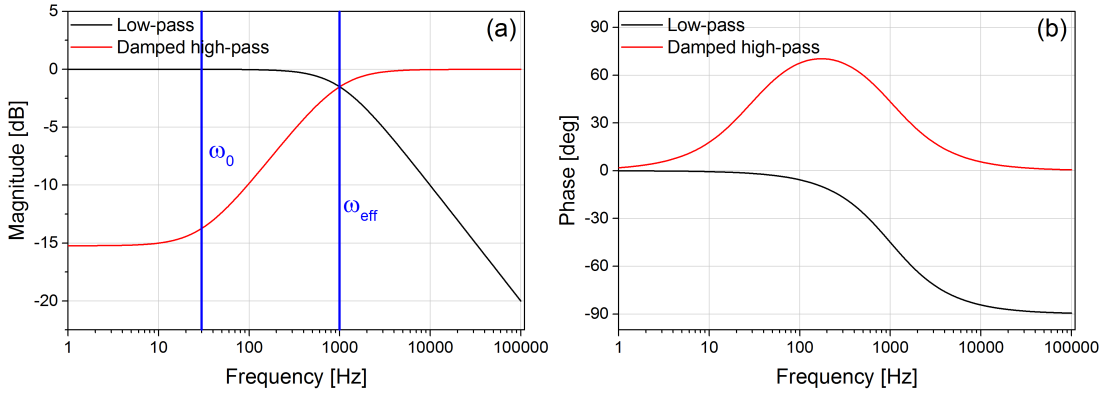


Figure 5.1: Typical transfer functions of an exemplary Yb^{3+} - or Er^{3+} -doped fiber amplifier. (a): Magnitude of a low-pass (black) that corresponds to the pump-to-signal transfer function and magnitude of a damped high-pass (red) that corresponds to the seed-to-signal transfer function. (b): Corresponding phase shifts.

The constants

$$\begin{aligned} B_s &= \frac{\Gamma_s}{A_c} \left(\sigma_s^{\text{abs}} + \sigma_s^{\text{em}} \right) \\ B_p &= \frac{\Gamma_p}{A_c} \left(\sigma_p^{\text{abs}} + \sigma_s^{\text{em}} \right) \end{aligned} \quad (5.3)$$

are determined by the absorption and emission cross sections σ_s^{abs} , σ_p^{abs} , σ_s^{em} , and σ_p^{em} and the overlap factors Γ_s and Γ_p of the seed and the pump light with the core area A_c of the fiber. The overlap factors can be expressed as

$$\Gamma_{p,s} = 1 - \exp\left(\frac{-2r_c^2}{w_{p,s}^2}\right) \quad (5.4)$$

where r_c is the core diameter and

$$w_{p,s} \simeq r_c \left(0.65 + \frac{1.619}{V_{p,s}^{1.5}} + \frac{2.879}{V_{p,s}^6} \right) \quad (5.5)$$

is either the mode radius of the pump or seed light, which depends on the V-parameter $V_{p,s}$ of the fiber and which is slightly different at the pump and the seed wavelength. In case of a cladding-pumped amplifier, the overlap of the pump light with the core must be rescaled for example by a factor of $\frac{A_c}{A_{\text{clad}}}$ where A_{clad} is the pump cladding area. Commonly, the cut-off frequency ω_{eff} is understood as being the inverse of the effective ion lifetime and the population of the upper energy state, i.e. the inversion, can only follow pump power modulations that are slower than this effective lifetime. Mathematically, this behavior corresponds to the low-pass given by Eq. (5.1).

The seed-to-signal transfer function is given by a damped high-pass

$$\frac{m_s^{(s)} e^{i\phi_s^{(s)}}}{m_{\text{in}}} = \frac{\omega_0 + i\omega}{\omega_{\text{eff}} + i\omega} \quad (5.6)$$

like it is also presented schematically in Fig. 5.1. The upper cut-off frequency ω_{eff} is the same as for the case of a pump power modulation and the lower cut-off frequency

$$\omega_0 = B_s P_{s,0}(z=0) + B_p P_{p,0}(z=L) + \frac{1}{\tau} \quad (5.7)$$

is related to ω_{eff} by

$$\omega_0 = \omega_{\text{eff}} + B_s (P_{s,0}(z=0) - P_{s,0}(z=L)). \quad (5.8)$$

Thus, in case of a seed power modulation high frequency noise ($\omega_{\text{eff}} < \omega$) couples lossless to the output power of the amplifier and low frequency noise ($\omega < \omega_0$) is suppressed. The magnitude of the suppression is determined by the separation of ω_0 and ω_{eff} , which is related to the gain of the amplifier, see Eq. (5.8).

Within the frame of this thesis, the methodology originally applied in [Nov02b] to obtain the above discussed transfer functions of Yb^{3+} - and Er^{3+} -doped fiber amplifiers has been adopted as far as possible for $\text{Er}^{3+}:\text{Yb}^{3+}$ -codoped fiber amplifiers and the results are presented in the following. The analysis has been limited to the frequency range of 1 Hz- 100 kHz as this is the relevant domain for interferometric GWDs. In addition, in order to keep the evaluation of the results as simple as possible the analysis has been restricted to $\text{Er}^{3+}:\text{Yb}^{3+}$ -codoped fiber amplifiers cladding-pumped at 976 nm and well below the threshold of parasitic processes at 1.0 μm . Thus, a potential co-seed was not included in the analysis, but it can be integrated by corresponding additional terms in the rate equations.

5.1.1 Analytical Model

As a reminder, the $\text{Er}^{3+}:\text{Yb}^{3+}$ level system is presented in Fig. 5.2. As mentioned earlier, the Yb^{3+} -to- Er^{3+} energy transfer corresponds to a de-excitation of an Yb^{3+} -ion from its excited energy state ${}^2\text{F}_{5/2}$ to the ground state ${}^2\text{F}_{7/2}$ and an excitation of a neighboring Er^{3+} -ion from its ground state ${}^4\text{I}_{15/2}$ to the upper energy state ${}^4\text{I}_{11/2}$, from where it quickly relaxes via non-radiative multi-phonon transitions to the metastable energy state ${}^4\text{I}_{13/2}$. A seed signal can then be amplified by stimulated transitions between the metastable Er^{3+} energy state ${}^4\text{I}_{13/2}$ and the ground state ${}^4\text{I}_{15/2}$.

The rate equations of an $\text{Er}^{3+}:\text{Yb}^{3+}$ -codoped fiber amplifier without back-transfer of

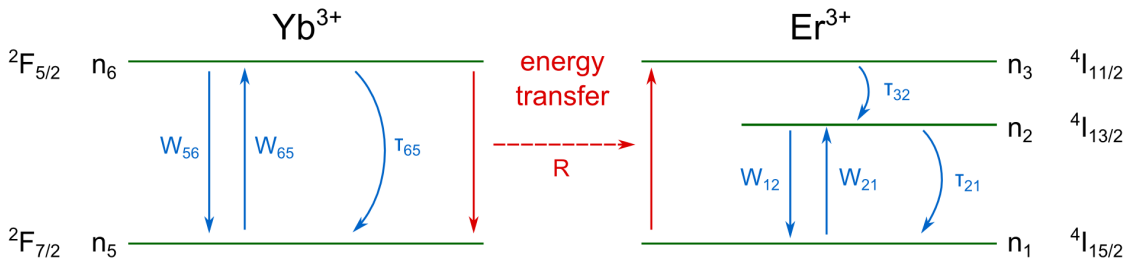


Figure 5.2: Energy level diagram of the $\text{Er}^{3+}:\text{Yb}^{3+}$ system. Not included are any up-conversion processes, back-transfer of energy or absorption of pump light by the Er^{3+} -ions.

energy and without absorption of pump light by the Er³⁺-ions can be expressed as [Kar97]

$$\begin{aligned}
0 &= p_{\text{Er}} - n_1 - n_2 - n_3 \\
\frac{\partial n_2}{\partial t} &= W_{12}n_1 - W_{21}n_2 - \frac{n_2}{\tau_{21}} + \frac{n_3}{\tau_{32}} \\
\frac{\partial n_3}{\partial t} &= -\frac{n_3}{\tau_{32}} + Rn_6n_1 \\
0 &= p_{\text{Yb}} - n_5 - n_6 \\
\frac{\partial n_6}{\partial t} &= W_{56}n_5 - W_{65}n_6 - \frac{n_6}{\tau_{65}} - Rn_6n_1
\end{aligned} \tag{5.9}$$

where t represents the time, n_i the population density of the i -th energy state, and τ_{ij} the lifetime of the transition from the i -th to the j -th energy state. R is the cross-relaxation coefficient, which determines the Yb³⁺-to-Er³⁺ energy transfer, and p_{Er} and p_{Yb} are the Er³⁺- and Yb³⁺-doping concentrations. The W_{ij} terms represent the stimulated transfer rates between the individual Yb³⁺ and Er³⁺ energy states and can be expressed as

$$W_{56} = \frac{\Gamma_p \sigma_p^{\text{abs}} P_p(z,t)}{A_c} \quad W_{65} = \frac{\Gamma_p \sigma_p^{\text{em}} P_p(z,t)}{A_c} \tag{5.10}$$

$$W_{12} = \frac{\Gamma_s \sigma_s^{\text{abs}} P_s(z,t)}{A_c} \quad W_{21} = \frac{\Gamma_s \sigma_s^{\text{em}} P_s(z,t)}{A_c}. \tag{5.11}$$

Again, A_c is the fiber core area and σ_s^{abs} , σ_p^{abs} , σ_s^{em} , and σ_p^{em} are the absorption and emission cross sections of the pump and the seed. In addition, $P_p(z,t)$ and $P_s(z,t)$ are the pump and seed power in units of photons per second.

Any small modulation of the seed or pump power leads to a corresponding modulation of the population density of the Er³⁺:Yb³⁺ system around its steady state solution. The exact lifetime of the upper Er³⁺ energy state ${}^4\text{I}_{11/2}$ depends on the core composition of the fiber under use. Typically, it is kept as small as possible by codoping the core with P₂O₅ to avoid back-transfer of energy, see section 3.2.2. Thus and in particular for the evaluation of the steady state population densities, a vanishing lifetime is commonly assumed in the literature, see for example [Yah03] and references within. As only modulation frequencies up to 100 kHz are considered here, it appears to be justified to assume that the lifetime of the upper Er³⁺ energy state ${}^4\text{I}_{11/2}$ is not much larger than 10 μs , in particular as it is already in the order of some microseconds without the P₂O₅-codoping [Lay77]. Under this assumption, the upper Er³⁺ energy state ${}^4\text{I}_{11/2}$ reacts instantaneously to any change of pump or seed power and from the experimental results, which are presented later in this chapter, there is no evidence that this approximation might be wrong. As a consequence,

the rate equations of the $\text{Er}^{3+}:\text{Yb}^{3+}$ system can be simplified by neglecting the upper Er^{3+} energy state $^4\text{I}_{11/2}$. This approach leads to an energy transfer directly between the upper Yb^{3+} energy state $^2\text{F}_{5/2}$ and the metastable Er^{3+} energy state $^4\text{I}_{13/2}$, which is denoted from here on the upper Er^{3+} energy state for the sake of convenience. The simplified rate equations are then given by

$$\begin{aligned} 0 &= p_{\text{Er}} - n_1 - n_2 \\ \frac{\partial n_2}{\partial t} &= W_{12}n_1 - W_{21}n_2 - \frac{n_2}{\tau_{21}} + Rn_6n_1 \\ 0 &= p_{\text{Yb}} - n_5 - n_6 \\ \frac{\partial n_6}{\partial t} &= W_{56}n_5 - W_{65}n_6 - \frac{n_6}{\tau_{65}} - Rn_6n_1 \end{aligned} \quad (5.12)$$

and the evolution of the pump light $P_p(z,t)$ and seed light $P_s(z,t)$ along the fiber for any time t is given by

$$\frac{dP_p}{dz} = \Gamma_p(n_6\sigma_p^{\text{em}} - n_5\sigma_p^{\text{abs}})P_p = A_c(W_{65}n_6 - W_{56}n_5) \quad (5.13)$$

$$\frac{dP_s}{dz} = \Gamma_s(n_2\sigma_s^{\text{em}} - n_1\sigma_s^{\text{abs}})P_s = A_c(W_{21}n_2 - W_{12}n_1). \quad (5.14)$$

In case of a forward pumped amplifier, Eqs. (5.12), (5.13), and (5.14) constitute a system of partial differential equations (PDEs) with boundary conditions

$$\begin{aligned} P_p(z=0,t) &= P_{p,\text{in}}(t) \\ P_s(z=0,t) &= P_{s,\text{in}}(t). \end{aligned} \quad (5.15)$$

As the main focus here is the response of the amplified seed signal to pump or seed power modulations, the following analysis is focused on the corresponding equations for the upper Er^{3+} energy state. However, the response of the upper Yb^{3+} energy state and the residual pump power to a seed or pump power modulation can be analyzed similarly. First, substitution of Eq. (5.14) into the corresponding rate equation for the upper Er^{3+} energy state and integration along the fiber leads to

$$(5.16)$$

where

$$N_2 = \int_{z=0}^{z=L} dz A_c n_2 \quad (5.17)$$

is the total length-integrated ion population of the upper Er³⁺ energy state and

$$X = \frac{R}{A_c} \int_{z=0}^{z=L} dz A_c n_1 A_c n_6 \quad (5.18)$$

corresponds to the total energy transfer along the fiber. In addition, by partial integration of Eq. (5.14) the seed power at the end of the fiber ($P_s(z = L, t)$) can be related with the seed power at the beginning of the fiber ($P_s(z = 0, t)$)

$$P_s(z = L, t) = P_s(z = 0, t) e^{B_s N_2 - C_s} \quad (5.19)$$

with

$$B_s = \frac{\Gamma_s}{A_c} (\sigma_s^{\text{em}} + \sigma_s^{\text{abs}}) \quad (5.20)$$

$$C_s = \Gamma_s \sigma_s^{\text{abs}} L p_{\text{Er}}.$$

Finally, substitution of Eq. (5.19) into Eq. (5.16) leads to

$$\frac{\partial N_2}{\partial t} = P_s(z = 0) (1 - e^{B_s N_2 - C_s}) - \frac{N_2}{\tau_{21}} + X. \quad (5.21)$$

Any sinusoidal modulation of the input pump or seed power

$$P_{p,s}(z = 0, t) = P_{p,s,\text{in}} (1 + m_{p,s} e^{i\omega t}) \quad (5.22)$$

with a small modulation depth $m_{p,s}$ will lead to a sinusoidal modulation of the total population of the upper Er³⁺ energy state

$$N_2(t) = N_{2,0} \left(1 + m_2^{(p,s)} e^{i(\omega t + \phi_2^{(p,s)})} \right) \quad (5.23)$$

and of the total energy transfer

$$X(t) = X_0 \left(1 + m_X^{(p,s)} e^{i(\omega t + \phi_X^{(p,s)})} \right) \quad (5.24)$$

where the superscripted (p) or (s) indicates either pump or seed power modulation. By substitution of Eqs. (5.23), (5.24), and (5.22) into Eq. (5.21) and by neglecting higher order terms with respect to the modulation depths one obtains in case of a pump power

modulation

$$\frac{N_{2,0}m_2^{(p)}}{m_p}e^{i\phi_2^{(p)}} = \frac{X_0m_X^{(p)}}{m_p}e^{i\phi_X^{(p)}}\frac{1}{\omega_{\text{eff}} + i\omega} \quad (5.25)$$

and in case of a seed power modulation

$$\frac{N_{2,0}m_2^{(s)}}{m_s}e^{i\phi_2^{(s)}} = \frac{P_{s,0}(z=0) - P_{s,0}(z=L)}{\omega_{\text{eff}} + i\omega} + \frac{X_0m_X^{(s)}}{m_s}e^{i\phi_X^{(s)}} \quad (5.26)$$

with

$$\omega_{\text{eff}} = B_s P_{s,0}(z=L) + \frac{1}{\tau_{21}}. \quad (5.27)$$

Equations (5.25) and (5.26) can be used to calculate the response of the amplified seed signal to a pump power modulation

$$\frac{m_s^{(p)}}{m_p}e^{i\phi_s^{(p)}} = \frac{X_0m_X^{(p)}}{m_p}e^{i\phi_X^{(p)}}\frac{B_s}{\omega_{\text{eff}} + i\omega} \quad (5.28)$$

or to a seed power modulation

$$\frac{m_s^{(s)}}{m_s}e^{i\phi_s^{(s)}} = \frac{\omega_0 + i\omega}{\omega_{\text{eff}} + i\omega} + \frac{X_0m_X^{(s)}}{m_s}e^{i\phi_X^{(s)}} \quad (5.29)$$

with

$$\omega_0 = B_s P_{s,0}(z=0) + \frac{1}{\tau_{21}} = \omega_{\text{eff}} + B_s(P_{s,0}(z=0) - P_{s,0}(z=L)). \quad (5.30)$$

Thus, the pump-to-signal transfer function (see Eq. (5.28)) consists of a low-pass $\frac{B_s}{\omega_{\text{eff}} + i\omega}$ with a corresponding cut-off frequency ω_{eff} that is multiplied with an unknown transfer function $\frac{X_0m_X^{(p)}}{m_p}e^{i\phi_X^{(p)}}$ of the energy transfer. The seed-to-signal transfer function (see Eq. (5.29)) involves two terms, one is a damped high-pass $\frac{\omega_0 + i\omega}{\omega_{\text{eff}} + i\omega}$ with two cut-off frequencies $\omega_0 < \omega_{\text{eff}}$ and the other one is again a product of a low-pass with another unknown transfer function $\frac{X_0m_X^{(s)}}{m_s}e^{i\phi_X^{(s)}}$ of the energy transfer.

Based on these transfer functions several conclusions can be drawn and some open questions remain. First, the pump-to-signal transfer function predicts that any modulation of the pump power gets filtered by the unknown transfer function of the energy transfer before it has any influence on the upper Er^{3+} energy state population. In addition, if the

cut-off frequency ω_{eff} can be determined experimentally, Eq. (5.28) can be multiplied with the inverse of a corresponding low-pass in order to obtain the transfer function of the total energy transfer. Then, it is quite interesting to analyze if this transfer function of the energy transfer is somehow universal (for example a low-pass) or if it's different for different amplifier configurations. In case of a seed power modulation it seems reasonable to question if the second term of the seed-to-signal transfer function (see Eq. (5.29)) can be neglected in comparison with the first one, in particular at high modulation frequencies for which it is likely that the energy transfer will strongly suppress any transfer of modulation from the Er³⁺- to the Yb³⁺-ions due to its own finite transfer rate. Indeed, if the second term of Eq. (5.29) can be omitted, the seed-to-signal transfer function would be a damped high-pass and the cut-off frequencies ω_0 and ω_{eff} would be given by analytical expressions, similar to Er³⁺- and Yb³⁺-doped fiber amplifiers [Nov02b]. In addition, the upper cut-off frequency ω_{eff} could then be measured by modulating the seed power and, as explained above, Eq. (5.28) could be used to obtain the transfer function of the energy transfer.

5.1.2 Numerical Investigations

To study the gain dynamics of Er³⁺:Yb³⁺-codoped fiber amplifiers in more detail than the final analytical results allow for and to answer the questions formulated at the end of the previous section a numerical simulation was developed that utilized a finite volume solver [Guy09] to solve the PDE system defined by Eqs. (5.12), (5.13), and (5.14). For a given amplifier configuration in a first step always the steady state solution was calculated and subsequently either the input pump or seed power was modulated sinusoidally with a small modulation depth. The solver then stepped forward in time until a stable solution emerged, which was used to calculate the magnitude and phase of the relevant transfer functions by fitting a sinus to the data.

In the following, numerically obtained transfer functions of an exemplary Er³⁺:Yb³⁺-codoped fiber amplifier that was cladding-pumped at 976 nm are presented. The actual amplifier and simulation parameters are listed in Tab. 5.1. As far as possible, parameters similar to a commercially available single-mode Er³⁺:Yb³⁺-codoped fiber (SM-EYDF-6/125-HE, Nufern (East Grandby, CT, USA)) were used because this particular fiber was also used in the experiments (see next section). In contrast to the actual doping concentrations, which were kindly provided by Nufern, the cross sections were not known. Thus, cross sections from a commercially available software (Liekki Application Designer) were used. These cross sections were originally determined from Yb³⁺- and Er³⁺-doped aluminosilicate fibers and the actual cross sections of Er³⁺:Yb³⁺-codoped phosphoaluminosilicate fibers are certainly different. However, with respect to the present qualitative study of the gain

dynamics it is sufficient that the cross sections are of the correct magnitude. Furthermore, to the best of the author's knowledge the work presented in [Kar97] is the only result of an experimental investigation that links the energy transfer rate and the Er^{3+} - and Yb^{3+} -doping concentrations. Hence, the energy transfer rate R has been calculated from Eq. (15) in [Kar97].

Table 5.1: Parameters of the numerical simulation on the gain dynamics of an exemplary $\text{Er}^{3+}:\text{Yb}^{3+}$ -codoped fiber amplifier, which was cladding-pumped at 976 nm.

Parameter	Value	Note
λ_p	976 nm	Pump wavelength
λ_s	1555 nm	Seed wavelength
$P_{s,\text{in}}$	5 mW	Input seed power
$P_{p,\text{in}}$	up to 300 mW	Input pump power
r_c	6 μm	Core diameter
r_{clad}	125 μm	Cladding diameter
NA	0.18	Core NA
L	1.8 m	Fiber length
p_{Er}	$1.11 \times 10^{25} \text{ m}^{-3}$	Er^{3+} -doping concentration
p_{Yb}	$2.42 \times 10^{26} \text{ m}^{-3}$	Yb^{3+} -doping concentration
σ_p^{abs}	$2.5 \times 10^{-24} \text{ m}^2$	Absorption cross section for the pump
σ_p^{em}	$2.44 \times 10^{-24} \text{ m}^2$	Emission cross section for the pump
σ_s^{abs}	$2.78 \times 10^{-25} \text{ m}^2$	Absorption cross section for the seed
σ_s^{em}	$4.36 \times 10^{-25} \text{ m}^2$	Emission cross section for the seed
τ_{21}	10 ms	Lifetime of upper Er^{3+} state
τ_{65}	0.7 ms	Lifetime of upper Yb^{3+} state
R	$1.93 \times 10^{-22} \text{ m}^3\text{s}^{-1}$	Energy transfer rate

Due to the stiffness of the PDE system a maximum time step of 1×10^{-4} s was necessary to prevent any overshooting during the computation of the steady state solution. Thus, for the actual computation of the transfer functions, either a time step of 1×10^{-4} s or a smaller time step was used, in order to have a sufficiently large number of points per oscillation for the subsequent evaluation. Especially at high modulation frequencies it was necessary to compute several ($\gtrsim 10$) oscillations in order to allow the system to reach a stable solution, whereas at low modulation frequencies a stable solution already emerged after a few ($\lesssim 5$) oscillations.

The seed-to-signal transfer functions, i.e. the magnitude and the phase shift, for the case of a seed power modulation are presented in Figs. 5.3 (a) and 5.3 (b) for six different pump power levels. At first glance each of the transfer functions appears to be a damped high-pass with a flat magnitude at low and high frequencies and two distinctive cut-off

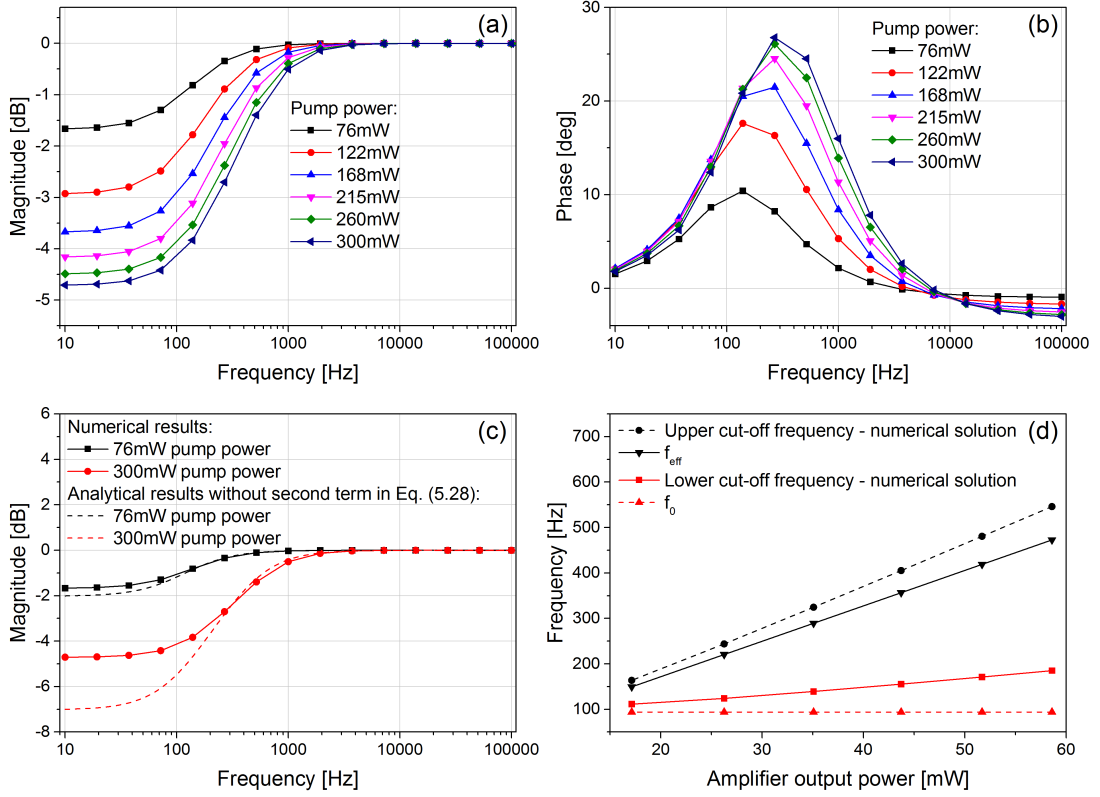


Figure 5.3: Numerically obtained transfer functions of a 976 nm cladding-pumped $\text{Er}^{3+}:\text{Yb}^{3+}$ -codoped fiber amplifier for the case of a seed power modulation: Magnitude (a) and phase (b). (c): Comparison of the numerically obtained magnitude and the magnitude of the first term in Eq. (5.29) for the lowest and highest pump power. (d): Comparison of the cut-off frequencies ω_0 and ω_{eff} of the first term in Eq. (5.29) and the cut-off frequencies of a damped high-pass fit to the numerically obtained transfer functions.

frequencies in between. However, to investigate the influence of both terms in Eq. (5.29) on the actual transfer functions, further numerical investigations have been carried out. In Fig. 5.3 (c) the magnitude of the numerically obtained seed-to-signal transfer functions at the highest and lowest pump power is compared with the magnitude of the first term of Eq. (5.29), which is a damped high-pass with cut-off frequencies ω_0 and ω_{eff} and which can be calculated directly from the steady state solution. As already conjectured at the end of the previous section, the second term of Eq. (5.29) is small for high modulation frequencies, so that the numerical solution is mainly determined by the first term. However, as Fig. 5.3 (c) might indicate that only the lower cut-off frequency ω_0 is influenced by the second term of Eq. (5.29), a damped high-pass was fitted to the numerical solutions and the corresponding cut-off frequencies are compared in Fig. 5.3 (d) with the cut-off frequencies

$f_0 = \frac{\omega_0}{2\pi}$ and $f_{\text{eff}} = \frac{\omega_{\text{eff}}}{2\pi}$ of the first term in Eq. (5.29). Indeed, both cut-off frequencies are influenced by the second term and with increasing pump power this effect is more and more pronounced. Note that it was also verified numerically that the actual influence of the second term depends on the launched seed power. Thus, even if the seed-to-signal transfer functions of an $\text{Er}^{3+}:\text{Yb}^{3+}$ -codoped fiber amplifier might behave like damped high-passes, setting the cut-off frequencies equal to ω_0 and ω_{eff} should only be used as an approximation and its suitability depends on the actual amplifier configuration.

The relevant results, i.e. the magnitude and the phase shift, for the case of a pump power modulation are presented in Figs. 5.4 (a) and 5.4 (b). While the solid lines correspond to the pump-to-signal transfer functions, the dashed lines correspond to the transfer functions of the energy transfer. The latter appear to be simple low-passes, as indicated by the typical shape of the magnitude (maximum inclination of -10 dB per decade) and the maximum phase shift of -90 degree. In addition, fits of a low-pass to the data revealed that the corresponding cut-off frequency is constant, this means it does not depend on the pump power. Note that the low-frequency magnitude depends weakly on the pump power because this might appear to be not the case in Fig. 5.4 (a).

Each of the pump-to-signal transfer functions appears to be a double low-pass, as indicated again by the typical shape of the magnitude (maximum inclination of -20 dB per decade) and the maximum phase shift of -180 degree. One of the cut-off frequencies is equal to the cut-off frequency of the transfer function of the energy transfer and the second one is equal to ω_{eff} (see Eq. (5.27)).

In Figs. 5.4 (c) and 5.4 (d) the computed pump-to-signal transfer functions and the transfer functions of the energy transfer of an $\text{Er}^{3+}:\text{Yb}^{3+}$ -codoped amplifier pumped at 915 nm are presented because this is one of the secondary pump wavelengths for such amplifiers. The cross sections were changed to $\sigma_{\text{p}}^{\text{abs}} = 6.7 \times 10^{-25} \text{ m}^2$ and $\sigma_{\text{p}}^{\text{em}} = 2.3 \times 10^{-26} \text{ m}^2$. In addition, the fiber length was 0.5 m, the seed power was 0.1 W, and the pump power was 5 W. Note that these values have been used because the corresponding results, i.e. the transfer functions, are very suitable to highlight what is discussed in the following. In particular in the magnitude of the energy transfer, in contrast to a simple low-pass, a non-uniform inclination at high frequencies is present. Furthermore, the phase also behaves different than a simple low-pass (compare for example to Fig. 5.4 (b)). Thus, although in the given case the deviation from a simple low-pass appears to be small, this result indicates that no universal shape for the transfer functions of the energy transfer exists. Most probably, this is explained by the nonlinear coupling of the upper Yb^{3+} energy state and the Er^{3+} ground state by the energy transfer process in the rate equations, see Eq. (5.12).

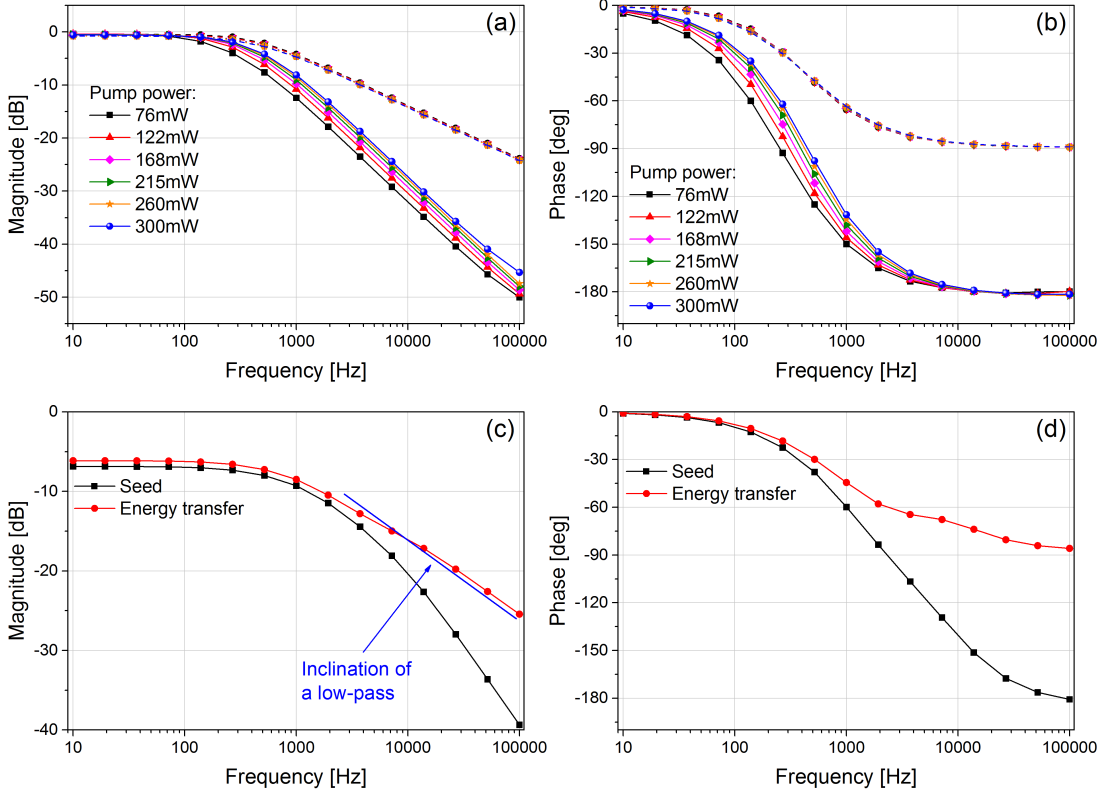


Figure 5.4: Numerically obtained transfer functions of the energy transfer (dashed lines) and the amplified signal (solid lines) of a 976 nm cladding-pumped $\text{Er}^{3+}:\text{Yb}^{3+}$ -codoped fiber amplifier for the case of a pump power modulation: Magnitude (a) and phase (b). Computed transfer functions of the energy transfer and amplified seed of an $\text{Er}^{3+}:\text{Yb}^{3+}$ -codoped fiber amplifier that was cladding-pumped at 915 nm: Magnitude (c) and phase (d).

5.1.3 Experimental Results

The experimental setup for the measurements of the transfer functions of an $\text{Er}^{3+}:\text{Yb}^{3+}$ -codoped fiber amplifier with parameters similar to the numerical simulation is presented in Fig. 5.5. A single-mode laser diode emitting at 976 nm was used to pump the amplifier and in order to convert the single-mode to multimode radiation a short piece of tightly spooled multimode fiber was spliced to the pump diode. Modulation of the pump power could be obtained by modulating the driving current of the diode. A distributed feedback (DFB) laser diode emitting at 1555 nm was used to seed the amplifier and an additional fiber-coupled AOM allowed to modulate the seed power as a modulation of the driving current led to unwanted wavelength shifts. The pump and seed light was combined in an in-house made pump combiner. As a reference port for the pump power modulation

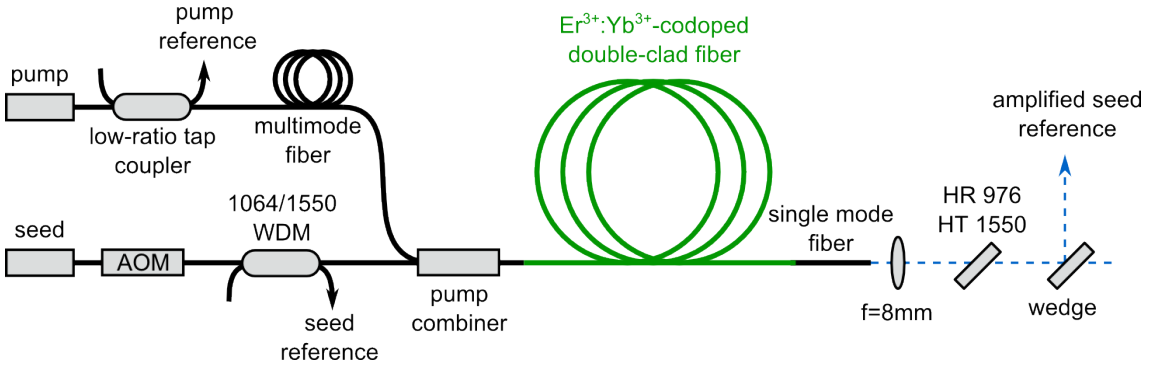


Figure 5.5: Experimental setup for the measurements of the transfer functions of a 976 nm cladding-pumped $\text{Er}^{3+}:\text{Yb}^{3+}$ -codoped fiber amplifier.

a low-ratio tap coupler behind the pump diode was used. To obtain a reference port for the seed power modulation a 1064/1550 nm wavelength division multiplexer (WDM) was integrated behind the AOM. This WDM was also protecting the seed diode from any potentially backward propagating Yb^{3+} -ASE. As in the numerical simulation, behind the pump combiner a maximum pump power of 300 mW and a seed power of around 5 mW could be used for the amplifier. Because it was discovered that the presence of cladding light distorted the measured transfer functions, high index paste and a short piece of a matching single-mode fiber were used to remove the cladding light at the end of the amplifier. After filtering out any residual pump light with a dichroic mirror, the amplified seed power was measured and a small fraction was used for the modulation measurements. Note that the measured maximum output power of 30 mW at a maximum pump power of 300 mW and the corresponding slope efficiency were a factor of two smaller compared to the numerically obtained values. However, this is acceptable as the model for the numerical simulation was rather simple and did not include any up-conversion processes or other loss mechanisms. For the measurements of the transfer functions the reference ports were connected to photodiodes, each with a bandwidth of 150 MHz. Sweeping of the pump or seed power modulation frequency and recording of the actual transfer functions was performed with a dynamic signal analyzer. Note that the actual measurements were performed at pump power levels similar to those used in the numerical simulation.

In Figs. 5.6 (a) and 5.6 (b) the measured seed-to-signal transfer functions are presented. Similar to the results of the numerical simulation, each of the seed-to-signal transfer functions appears to be a damped high-pass, but, as stated earlier, the corresponding cut-off frequencies are not necessarily equal to ω_{eff} and ω_0 . Nevertheless, fits of a damped high-pass to the measured data were performed in order to determine both cut-off frequencies for a later comparison (see paragraph after the next).

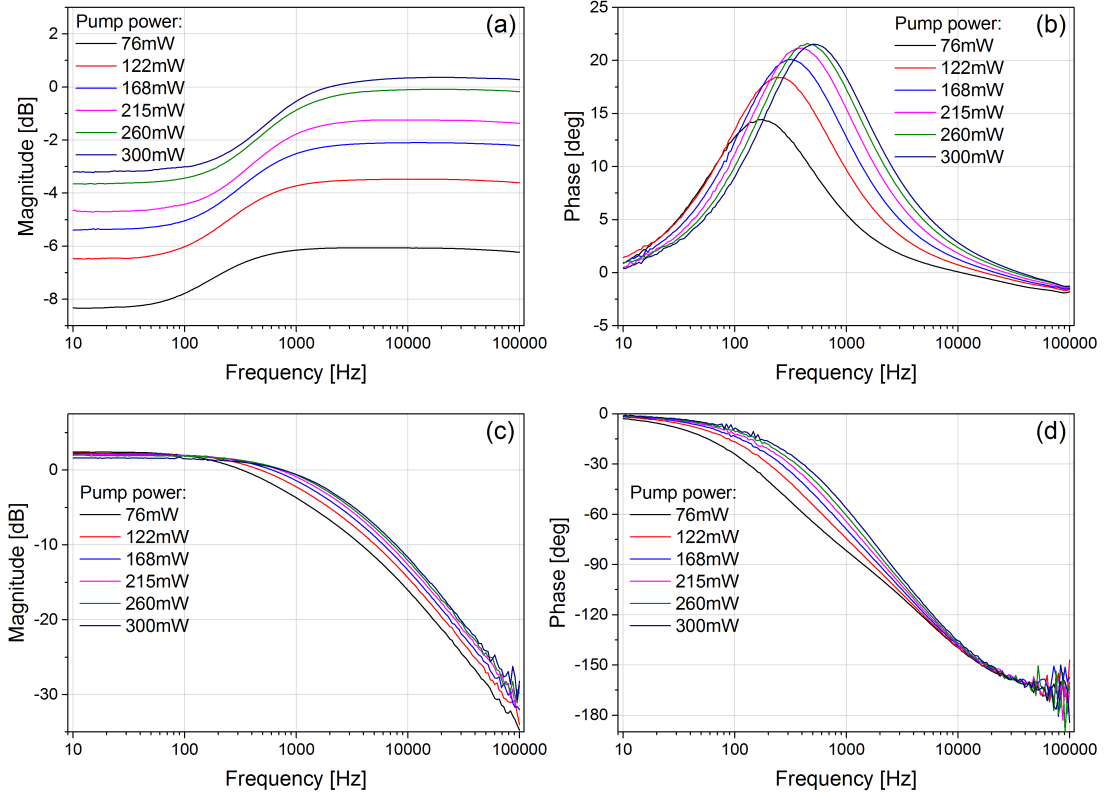


Figure 5.6: Measured transfer functions (not normalized) of the $\text{Er}^{3+}:\text{Yb}^{3+}$ -codoped fiber amplifier for the case of a seed power modulation: Magnitude (a) and phase (b). Measured transfer functions (not normalized) for the case of a pump power modulation: Magnitude (c) and phase (d).

The pump-to-signal transfer functions are presented in Figs. 5.6 (c) and 5.6 (d). As predicted by the numerical simulation, each of the transfer functions appears to be a double low-pass, as indicated by a maximum inclination of the magnitude of -20 dB per decade and by the maximum phase shift of almost -180 degree. However, in contrast to the numerical results the two kinks in the magnitude at around 0.1 - 1 kHz and around 8.5 kHz, which correspond to the two cut-off frequencies, are more separated. Such a behavior could be reproduced in the numerical simulation by setting the energy transfer coefficient R around 100 times higher than in Tab. 5.1. Note that this approach led to a comparably large amplifier efficiency, which can most probably be compensated to some extent by implementing up-conversion or other loss processes in the model. Furthermore, Eq. (15) in [Kar97] was obtained by comparing the performance of a few purely Er^{3+} -doped fibers with respect to the up-conversion process and by drawing some analogies to the Er^{3+} -to- Yb^{3+}

energy transfer process, see also [Fed95]. These analogies were unreasonable because it was for example indirectly assumed that the Er^{3+} and Yb^{3+} cross sections are equal. Thus, the experimental results of this thesis are a strong indication that further investigations of this topic are necessary in the future.

To obtain the two cut-off frequencies of the measured pump-to-signal transfer functions, fits of a double low-pass to the data were performed and the corresponding cut-off frequencies are compared with the cut-off frequencies that have been obtained from the seed-to-signal transfer functions in Fig. 5.7 (a). For the case of a seed power modulation, both cut-off frequencies increase linearly with the amplifier output power like it was already the case for the numerical results. In case of a pump power modulation, the upper cut-off frequency is almost constant for different amplifier output power levels. Thus, with respect to the numerical results, it is most certainly determined by the energy transfer process. The lower cut-off frequency (which is then ω_{eff} , see Eq. (5.27)) increases linearly with the amplifier output power and is, in contrast to the numerical results, equal to the upper cut-off frequency obtained for the case of a seed power modulation. Hence, for the presented experimental configuration the additive term of the energy transfer (see Eq. (5.29)) has only a negligible influence on the seed-to-signal transfer functions at high frequencies and the corresponding upper cut-off frequency is equal to ω_{eff} . Furthermore, Eq. (5.27) indicates that for a vanishing amplifier output power, ω_{eff} is equal to the inverse of the lifetime of the upper Er^{3+} energy state. Thus, a linear fit was performed to the data and the lifetime was determined to be 3 ms, which is close to the value of 1-10 ms that is used throughout the literature.

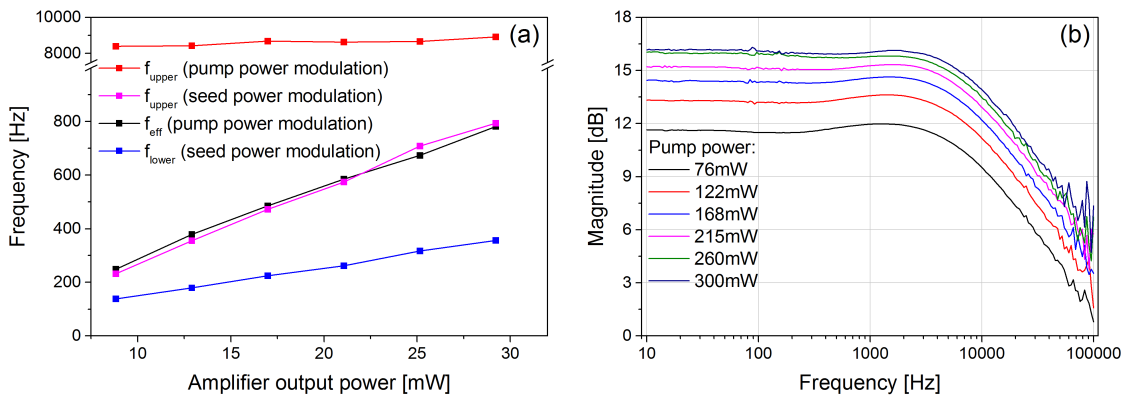


Figure 5.7: (a): Comparison of the cut-off frequencies obtained from the measured seed-to-signal and pump-to-signal transfer functions of the $\text{Er}^{3+}:\text{Yb}^{3+}$ -codoped fiber amplifier. (b): Calculated magnitude of the transfer function of the energy transfer for a pump power modulation.

As argued above, if ω_{eff} is known, the measured pump-to-signal transfer functions can be multiplied with the inverse of a corresponding low-pass in order to obtain the transfer functions of the energy transfer. The corresponding results are presented in Fig. 5.7 (b). Each of the transfer functions of the energy transfer appears, as already suggested by the numerical results, to be a simple low-pass (inclination of -10 dB per decade) with a corresponding cut-off frequency at around 8.5 kHz that is independent of the amplifier output power. In addition, similar to the numerical results, the magnitude at low modulation frequencies depends on the actual pump power. Indeed, the differences are more pronounced, but this can be explained by a missing normalization of the measured transfer functions and the fact that not all experimental parameters were exactly known.

5.1.4 Conclusion

In the frame of this thesis, the gain dynamics of Er³⁺:Yb³⁺-codoped fiber amplifiers have been studied for the first time. As the Yb³⁺-to-Er³⁺ energy transfer process appears as a nonlinear term in the rate equations, a full analytical solution of the problem does, to the best of the author's knowledge, not exist. Thus, a numerical simulation was developed that allowed to solve the underlying PDE system numerically by a finite volume solver. Numerical results of an exemplary 976 nm cladding-pumped Er³⁺:Yb³⁺-codoped fiber amplifier well below the threshold of parasitic processes at 1.0 μm suggest that the seed-to-signal transfer function behaves like a damped high-pass. However, depending on the actual amplifier configuration, the unknown transfer function of the energy transfer can influence both cut-off frequencies, so that they are not given by analytical expressions. In case of a pump power modulation, the Yb³⁺-to-Er³⁺ energy transfer behaves like a low-pass. Consequently and in accordance with the analytical results, the pump-to-signal transfer function is given by a double low-pass. However, it was also discovered with the numerical simulation that the transfer function of the Yb³⁺-to-Er³⁺ energy transfer of an exemplary 915 nm cladding-pumped Er³⁺:Yb³⁺-codoped fiber amplifier cannot be described by a simple low-pass. Hence, a universal behavior of the transfer function of the Yb³⁺-to-Er³⁺ energy transfer does not exist, but it is given approximately by a simple low-pass.

Experimental transfer functions were recorded with an Er³⁺:Yb³⁺-codoped fiber amplifier setup quite comparable to the setup used in the numerical simulations. Corresponding results show good qualitative agreement with the numerical results. Indeed, the transfer function for a pump power modulation behaved like a double low-pass and the transfer function for a seed power modulation behaved like a damped high-pass. In addition, in contrast to the numerical results, only the upper cut-off frequency of the damped high-

pass was influenced by the transfer function of the energy transfer. Furthermore, the experimental results suggest a lifetime of the upper Er^{3+} energy state in the range of 3 ms, which is quite comparably to the value of 1-10 ms that is commonly used in the literature. Although the simple low-pass behavior of the energy transfer was also observed in the experiment, the experimental results suggest that the energy transfer rate is higher than predicted by the results, i.e. Eq. (15), presented in [Kar97]. However, this is most probably explained by some unreasonable approximations that were used in [Kar97] and [Fed95] and further investigations of this topic are definitely required.

5.2 Optical Phase Shift

As laser radiation consists of electromagnetic waves, not only the output power of a fiber amplifier fluctuates with time but also the optical phase. In particular for laser sources in interferometric GWDs the corresponding phase noise is of quite significance since it couples to the signal of the interferometer and affects the sensitivity.

The accumulated optical phase shift of an electromagnetic signal propagating through a fiber amplifier depends on the actual fiber length and the refractive index. While it is well-known that the refractive index varies with temperature, it is also coupled to the inversion, i.e. the gain, of the fiber amplifier via the KKR [Kro26]. The origin of the KKR relies on the fact that the frequency-dependent electric susceptibility $\chi(\omega)$ is connected to the temporal response $u(t)$ of the fundamental dipoles to an external electric field by a Fourier transformation. As the temporal response must be causal ($u(t < 0) = 0$), the theory of the Fourier transformations states that the susceptibility is analytic in the upper half plane of the complex plane. Mathematically this means that the real and imaginary parts of the susceptibility are connected via a Hilbert transformation. Since the real part of the susceptibility determines the refractive index and the imaginary part is responsible for the absorption, the KKR describes the interplay of refractive index and absorption: A change in absorption causes a corresponding change of the refractive index and vice versa.

In a typical fiber amplifier a significant absorption is given by the absorption of the pump light. The corresponding absorption band can be described mathematically by a complex Lorentz function

$$L(\omega) = \alpha \frac{i}{1 - i \frac{\omega - \omega_0}{\Delta\omega}} \quad (5.31)$$

whose real part corresponds to the actual absorption and whose imaginary part is related to the corresponding change of the refractive index, i.e. the induced phase shift. ω_0 is the center frequency, α the magnitude, and $\Delta\omega$ the linewidth of the absorption. An exemplary

plot of the real and imaginary part of Eq. (5.31) around the center frequency is presented in Fig. 5.8. Indeed, the plot suggests that a significant phase shift can only be expected near the center frequency, whereas the shift should be negligible directly at and far from the resonance. However, in most rare-earth doped glasses very strong absorptions in the ultraviolet (UV) lead to significant refractive index changes even far from the absorption bands [Ark98; Dig97]. Note that the actual strength of these absorptions is coupled to the inversion, i.e. the gain, of the fiber amplifier. Thus, by changing the gain, e.g. by temporally modulating the pump power, a corresponding modulation of the refractive index can be induced, which then induces an optical phase shift of the signal.

From time domain measurements on Yb^{3+} -doped [Fot08] and Er^{3+} -doped [Tün11] fiber amplifiers it is known that the optical phase shift induced by a change of the pump power is a result of temperature contributions and the KKR. In addition, results of advanced frequency domain measurements on an Yb^{3+} -doped fiber amplifier indicate that the thermal effects are mostly responsible for slow ($\leq 1-10$ Hz) optical phase fluctuations, whereas KKR-induced optical phase fluctuations follow the comparably fast changes of the inversion, i.e. the gain [Tün12c]. However, the individual contributions of both effects on the total phase change depend on the actual amplifier configuration. For example, the induced phase shift can be already completely dominated by thermal effects if the amplifier is well-saturated, i.e. fluctuations of the pump power induce sufficient thermal load but barely change the gain. Such an amplifier configuration was utilized in [Tün12b] to investigate the thermally-induced refractive index changes in an Yb^{3+} -doped fiber amplifier. The

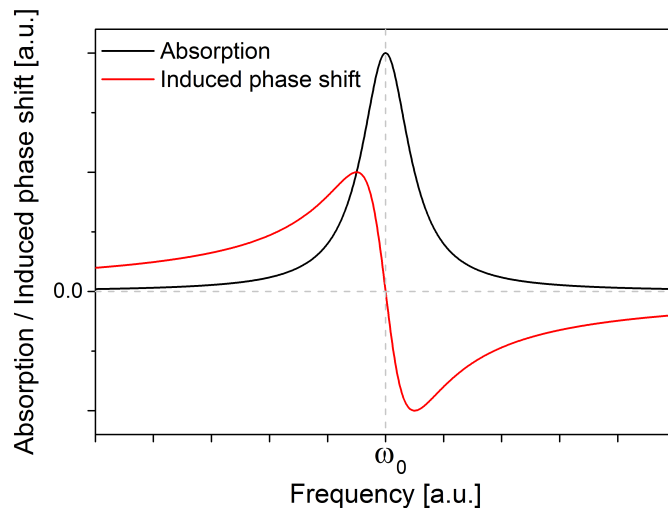


Figure 5.8: Lorentz-shaped absorption and corresponding phase shift induced by the Kramers–Kronig relation.

presented results in combination with an appropriate model indicate that the heating in the particular Yb^{3+} -doped fiber was not related to any transition between electronic states of the Yb^{3+} -ions. Instead, the heating of the Yb^{3+} -doped fiber core adopted instantaneously to any changes of the pump light, at least up to a pump power modulation frequency of 10 kHz. This result is somehow surprising as typical sources of heating such as the quantum defect or up-conversion processes are coupled to corresponding electronic states of the Yb^{3+} -ions and one might expect to see an influence of the corresponding transfer functions.

As argued, the temperature effects and the KKR contribute to the phase noise of rare-earth doped fiber amplifiers via corresponding refractive index changes. Thus, from a practical point of view and in particular for a potential application in GWDs, both effects are detrimental. Nevertheless, the refractive index changes induced by corresponding fluctuations of the pump power can be exploited by utilizing Yb^{3+} -doped fiber amplifiers as phase actuators in coherent beam combining (CBC) schemes of Er^{3+} -doped fiber amplifiers and vice versa [Fot09; Tün11]. However, although this method is quite elegant and allows for all-fiber setups, the actual actuator range scales with the number of contributing excited ions. In consequence, an additional fiber amplifier with a sufficiently large output power level is required and corresponding setups become quite complex. As a promising alternative a different all-fiber coherent beam combining scheme was investigated in [Tün12a]. Coherent combination of two Yb^{3+} -doped fiber amplifiers was achieved by controlling the differential phase shift between both amplifiers via a differential pump power control. Note that the differential control instead of controlling only the phase of one amplifier is a major feature of this scheme as it allows theoretically for a combined power that is not modulated. The same approach has been applied in [Wan15] in order to coherently combine two Yb^{3+} -doped fiber amplifiers with ns pulses and the authors state in their conclusion that they were even successful in combining three amplifiers.

As argued in the previous chapter, the power scaling of $\text{Er}^{3+}:\text{Yb}^{3+}$ -codoped fiber amplifiers is, due to the onset of parasitic lasing at $1.0\ \mu\text{m}$, somehow problematic and quite challenging. However, as also argued earlier, in terms of achievable efficiency and pump light absorption per unit length (important for nonlinear effects) $\text{Er}^{3+}:\text{Yb}^{3+}$ -codoped fibers are in favor compared to Er^{3+} -doped fibers. Thus, a coherent combination of multiple $\text{Er}^{3+}:\text{Yb}^{3+}$ -codoped fiber amplifiers with moderate output power levels might be a promising approach to achieve the output power levels desired by next-generation GWDs. As the differential pump power control scheme that was introduced in the previous paragraph is, due to the non-necessary additional phase actuator, a very promising CBC approach, it is also very interesting for the coherent combination of multiple $\text{Er}^{3+}:\text{Yb}^{3+}$ -codoped fiber amplifiers. Indeed, designing corresponding control loops is feasible even

if the actual coupling of pump power fluctuations and the induced phase shift in each of the amplifiers is not exactly known. However, from an academic point of view it is quite interesting to analyze the thermally-induced and the KKR-induced phase shift in $\text{Er}^{3+}:\text{Yb}^{3+}$ -codoped fiber amplifiers because the $\text{Er}^{3+}:\text{Yb}^{3+}$ -codoped level system provides for example two upper laser states that can contribute individually via corresponding UV resonances to the total KKR-induced phase shift. In addition, it is known that the Er^{3+} -doping concentration in typical $\text{Er}^{3+}:\text{Yb}^{3+}$ -codoped fibers is so high that the Er^{3+} -ions start to cluster [Lim12; Mys97]. Therefore, pair-induced as well as homogeneous up-conversion processes should contribute to the heating of $\text{Er}^{3+}:\text{Yb}^{3+}$ -codoped fiber amplifiers.

5.2.1 Experimental Setup

The experimental setup that was used to measure the pump power modulation induced refractive index changes in an exemplary 976 nm cladding-pumped $\text{Er}^{3+}:\text{Yb}^{3+}$ -codoped fiber amplifier is presented in Fig. 5.9. A probe laser at 1310 nm with a MHz linewidth was fed into a fiber based Mach-Zehnder interferometer by a corresponding tap coupler with a splitting ratio of 50:50. One of the interferometer arms contained the $\text{Er}^{3+}:\text{Yb}^{3+}$ -codoped fiber amplifier, which was quite comparable to the amplifier presented in the previous section. However, the 1064/1550 nm WDM was replaced by a 1310/1550 nm

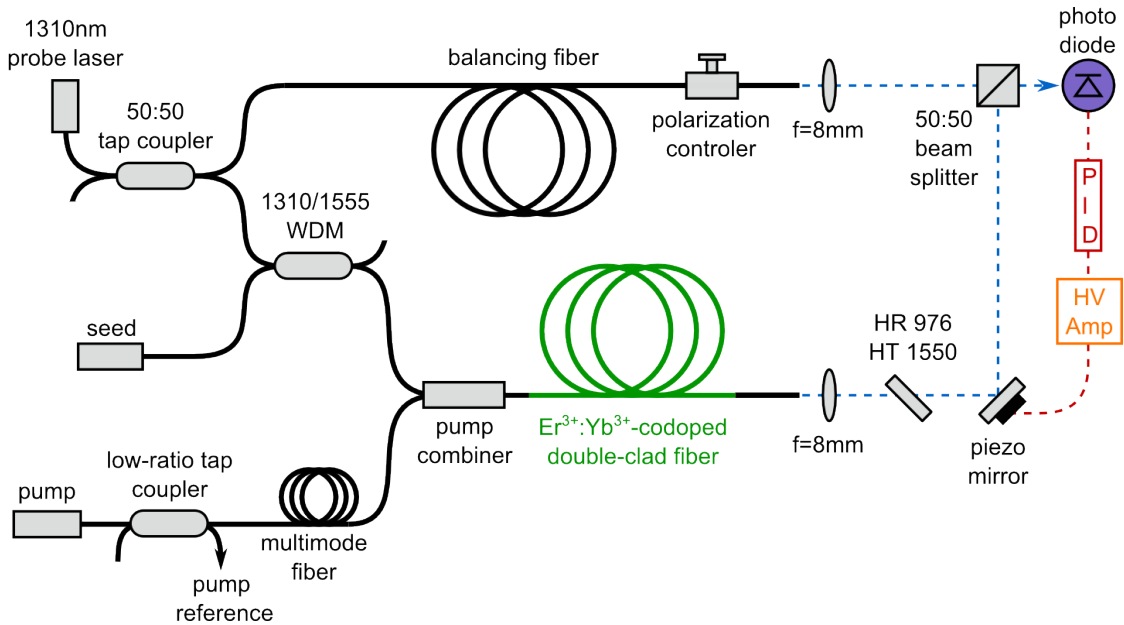


Figure 5.9: Fiber based Mach-Zehnder interferometer that was used to measure the pump power modulation induced refractive index changes in an exemplary $\text{Er}^{3+}:\text{Yb}^{3+}$ -codoped fiber amplifier.

WDM in order to combine the 1310 nm probe signal and the seed at 1555 nm. The other arm of the interferometer contained a balancing fiber whose length was matched to the $\text{Er}^{3+}:\text{Yb}^{3+}$ -codoped fiber amplifier in order to avoid excessive coupling of frequency noise from the 1310 nm probe laser to the interferometer signal. The output signals of both interferometer arms were recombined by a free-space 50:50 beam splitter and the corresponding interferometer signal was detected by a photodiode with a bandwidth of 150 MHz. The interferometer could be locked mid-fringe by a feedback loop that controlled via a proportional-integral-derivative (PID) controller one of the arm lengths of the interferometer by a piezo-mounted mirror.

5.2.2 Results

Even if not locked, the interferometer signal, i.e. the differential phase between both interferometer arms, was stable on a second time scale. Thus, in a first experiment a small step modulation was added to the pump power of the $\text{Er}^{3+}:\text{Yb}^{3+}$ -codoped fiber amplifier and the unlocked interferometer signal was monitored with the photodiode. A typical result of such a measurement at a pump power of 200 mW is presented in Fig. 5.10. Quite similar to the results of corresponding investigations of Er^{3+} -doped [Tün11] and Yb^{3+} -doped [Fot08] fiber amplifiers, two time scales can be identified: a fast, almost instantaneous step followed by a slow drift on a second time scale. Analog to Er^{3+} - and Yb^{3+} -doped fiber amplifiers, the fast change of the optical phase can be attributed to KKR-induced refractive index changes and the slow drift to thermal effects.

In order to investigate the frequency-dependent response of the optical phase to pump

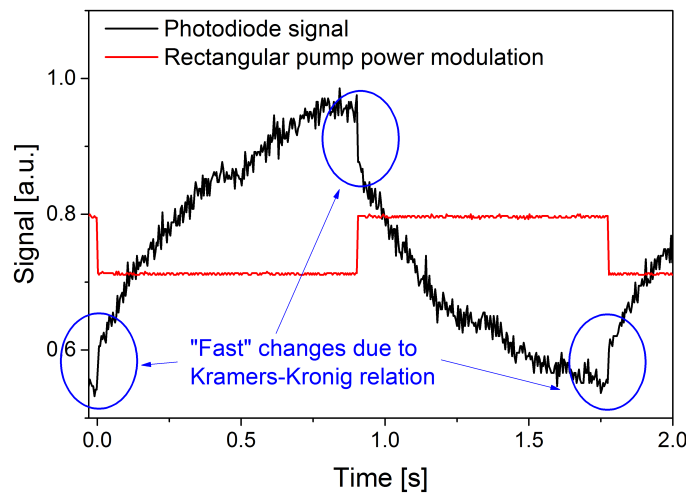


Figure 5.10: Induced phase shift in an exemplary $\text{Er}^{3+}:\text{Yb}^{3+}$ -codoped fiber amplifier due to a step modulation of the 976 nm pump power.

power modulation frequencies between 1 Hz and 100 kHz, the interferometer was locked. Note that a common way to perform the actual measurements would have been to chose a sufficiently large unity-gain frequency of the feedback loop, modulate the pump power, and monitor the control signal of the feedback loop. However, due to the comparably slow HV amplifier the maximum obtainable cut-off frequency of the feedback loop was limited to some hundreds of hertz, even though the PID controller would have allowed for larger cut-off frequencies. Thus, the parameters of the PID controller were chosen such that the cut-off frequency of the control loop was below 1 Hz and instead of evaluating the control signal the error signal, i.e. the signal of the photodiode, was monitored.

The results, i.e. the obtained pump-to-optical-phase transfer functions at different pump power levels, are presented in Fig. 5.11. At low pump power levels the shape of the transfer functions changes with increasing pump power, but for a pump power of more than 300 mW it does not change significantly anymore and thus the corresponding transfer functions are not shown in Fig. 5.11. As argued in the following, the characteristic shape of the transfer functions at pump power levels ≥ 300 mW cannot be explained completely for several reasons.

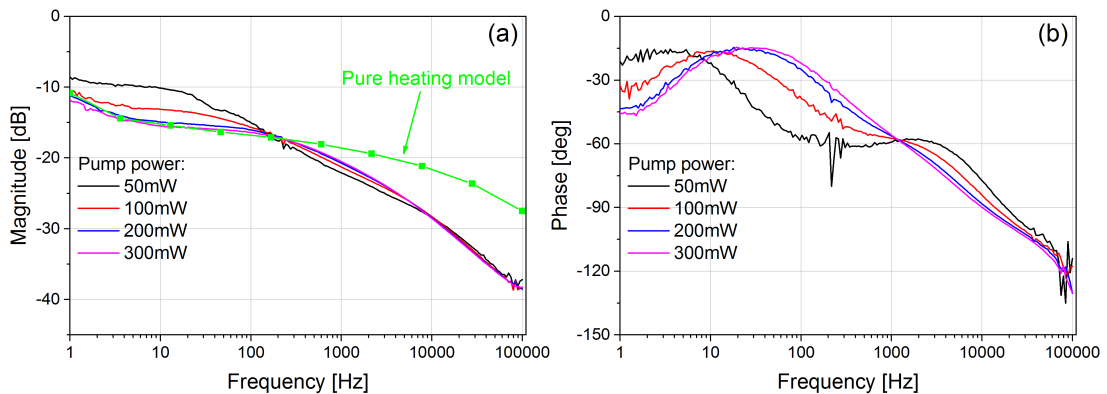


Figure 5.11: Measured pump-to-optical-phase transfer functions of the exemplary $\text{Er}^{3+}:\text{Yb}^{3+}$ -codoped fiber amplifier at different pump power levels: Magnitude (a) and phase (b). The green data points correspond to numerically obtained results under the assumption of thermally-induced refractive index changes [Tün12b].

If only thermally-induced refractive index changes are considered and under the assumption that the heating is not coupled to any energy state of the $\text{Er}^{3+}:\text{Yb}^{3+}$ system, the behavior of the transfer function up to 100 Hz at a pump power of 300 mW can be explained by a corresponding numerical simulation, originally developed by H. Tünnermann [Tün12b] (see the green data points in Fig. 5.11 (a)). However, at modulation frequencies of more than 100 Hz the magnitude of the observed transfer functions falls off steeper than the

model of pure heating can explain. Indeed, one could argue that a significant contribution to the heating should be given by the relaxation of the upper Er^{3+} energy state $^4\text{I}_{11/2}$ to the metastable Er^{3+} energy state $^4\text{I}_{13/2}$, i.e. the Er^{3+} quantum defect. Then, any pump power modulation would be filtered by the low-pass of the energy transfer before it induces refractive index changes via the quantum defect heating. However, this assumption leads to transfer functions that fall off steeper than the experimentally obtained transfer functions. Furthermore, to the best of the author's knowledge and as a result of detailed numerical investigations with the simulation tool introduced in the first part of this chapter, it is also not possible to reproduce the observed characteristic shape of the transfer functions by assuming only contributions of the upper Er^{3+} and Yb^{3+} energy states via the KKR, neither individually or in combination.

Possible origins for this result are most certainly additional loss processes in the $\text{Er}^{3+}:\text{Yb}^{3+}$ system, such as homogeneous and pair-induced up-conversion [Lim12; Mys97] or secondary energy transfer and non-participatory Yb^{3+} -ions [Sef04]. These loss processes lead to an excitation of higher energy states that can contribute via non-radiative relaxation processes and corresponding heating to thermally-induced refractive index changes and via UV resonances to KKR-induced refractive index changes. As long as the individual magnitudes of these effects and the dynamical responses, i.e. the transfer functions, of the additional energy states are not known, a final interpretation of the experimentally obtained pump-to-optical-phase transfer functions is not feasible.

5.2.3 Conclusion

In conclusion, the pump power modulation induced refractive index changes in an exemplary 976 nm cladding-pumped $\text{Er}^{3+}:\text{Yb}^{3+}$ -codoped fiber amplifier have been analyzed for the first time with a fiber-based Mach-Zehnder interferometer. In the time domain, experimental data indicate that thermally-induced as well as KKR-induced refractive index changes contribute to the total phase shift. However, a final interpretation of the frequency-dependent phase shift, induced by a sinusoidal pump power modulation up to a modulation frequency of 100 kHz, is not feasible, in particular as it remains unclear which thermal effects (due to additional loss mechanisms, e.g. up-conversion) and which energy states (via the KKR) contribute to the refractive index changes.

Some suggestions for further interesting and necessary investigations regarding the pump power modulation induced refractive index changes in $\text{Er}^{3+}:\text{Yb}^{3+}$ -codoped fiber amplifiers are provided in chapter 8 of this thesis. For example, the pump power modulation induced refractive index changes in an exemplary $\text{Er}^{3+}:\text{Yb}^{3+}$ -codoped fiber amplifier pumped at 1480 nm should be investigated in detail. Such an experiment will certainly help to

understand which effects that are exclusively related to the Er^{3+} -ions contribute to the total phase shift in $\text{Er}^{3+}:\text{Yb}^{3+}$ -codoped fiber amplifiers.

CHAPTER 6

Single-Mode Pump Source for Er³⁺-Doped Fiber Amplifiers

As argued in the previous chapters, single-frequency Er³⁺:Yb³⁺-codoped fiber amplifiers are promising but still very challenging candidates as laser sources at 1.5 μm in next-generation GWDs. Indeed, as shown in chapter 4 of this thesis, the co-seeding method is a viable approach to suppress the excessive generation of Yb³⁺-ASE and corresponding parasitic processes at 1.0 μm , even at comparably high output power levels of more than 10 W. However, corresponding setups are quite complex, i.e. they require a second seed source at 1.0 μm in combination with an appropriate and stable scheme for the in-coupling. Furthermore, as presented in the previous chapter and in contrast to Er³⁺-doped fiber amplifiers, predicting the noise transfer of Er³⁺:Yb³⁺-codoped fiber amplifiers at high output power levels, e.g. by an extrapolation from lower output power levels, is not feasible, in particular as a complete analytical solution is missing. If cladding-pumped at 976 nm, Er³⁺-doped fiber amplifiers do not present a viable alternative, in particular due to the typical low absorption at 976 nm as it requires long fiber lengths that lead to a decreasing threshold of SBS. In contrast, core-pumped Er³⁺-doped fiber amplifiers provide some good prospects regarding a possible application in next-generation GWDs for several reasons. Most probably, the length of the Er³⁺-doped fiber could be kept quite short as the absorption per unit length would be higher than in a cladding-pumped setup. Thus, the threshold of nonlinear effects would be increased significantly and it could even be possible to use an Er³⁺-doped fiber with a comparably small core that supports only the fundamental mode. Such a fiber would provide a high TEM₀₀ mode content and it would not be prone to mode instabilities since this effect only occurs in fibers supporting higher order modes [Jau11]. Even if a few-mode LMA fiber must be used for some reasons, the high overlap of the single-mode pump with the fundamental fiber mode compared to the small overlap with the higher order modes would make the fiber, i.e. the output

beam profile, effectively single-mode [Jas09]. It was also shown that core-pumping schemes of higher order mode fibers allow for stable amplification of a single higher order mode, which provides an increased threshold for nonlinear effects due to a large effective mode area and can be back-converted to the fundamental fiber mode quite efficiently [Nic12]. Unfortunately, single-mode laser diodes at 976 nm are limited to output power levels of some watts. However, as the absorption of Er³⁺-doped fibers is also sufficiently large at around 1480 nm, corresponding fiber amplifiers can be pumped quite efficiently at this wavelength with a small quantum defect. Indeed, the typical output power level of single-mode laser diodes at 1480 nm is also limited to some watts, but in recent years it has been shown that CRFLs are compact all-fiber laser sources at 1480 nm, which can provide output power levels of some hundreds of watts [Sup13a; Sup13b] and allow for high-power all-fiber Er³⁺-doped laser systems [Sup12a]. Therefore, CRFLs at 1480 nm are promising pump sources for core-pumped single-frequency Er³⁺-doped fiber amplifiers at 1.5 μm in next-generation GWDs. In the first part of this chapter numerically and experimentally obtained results are used to highlight the most common challenges, limitations, and workarounds regarding the experimental realization and the power scaling of CRFLs at 1480 nm, in particular because such a compilation was missing in the literature, so far.

The second part of this chapter is dedicated in more detail to one of the major limitations, namely the onset of lasing at the parasitic Stokes order. It is shown that it can be exploited to achieve a passive pump-to-Stokes noise transfer suppression. This approach was already proposed by others [Sun08a; Sun08b], but an experimental confirmation and investigations of optimization strategies were missing, so far. A first experimental proof-of-principle of the passive noise transfer suppression in a two-stage CRFL at 1180 nm and 1240 nm is presented in this thesis. In addition, experimental and numerical investigations of the gain dynamics in a single-stage Raman fiber lasers at 1180 nm with and without the parasitic Stokes order are presented. The results reveal some general relationships between the cavity design parameters and the parameters of the passive noise transfer suppression. Furthermore, results of an advanced numerical simulation propose that the passive noise transfer suppression can also be applied for CRFLs at 1480 nm with an additional parasitic Stokes order at 1580 nm. This is in particular very interesting for the design of low-noise Er³⁺-doped fiber amplifiers as the pump-to-signal noise transfer in such amplifiers is given by a low-pass [Nov02b]. Thus, a CRFL at 1480 nm in combination with the passive noise transfer suppression scheme could act as a low noise pump source for an Er³⁺-doped fiber amplifier, which then also provides a low initial power noise level. This is of particular interest for GWDs as the necessary power stabilization of the laser source requires and benefits from a low initial power noise level.

Part of the work and the results presented in this chapter have been published beforehand in [Ste15b].

6.1 Cascaded Raman Fiber Laser at 1480 nm

CRFLs exploit the SRS process and are a widely used concept to realize laser sources at wavelengths for which no active rare-earth dopants are available. A typical setup of an n -th order CRFL is presented in Fig. 6.1. Most commonly, an Yb^{3+} -doped fiber laser acts as a pump laser for a Raman conversion stage. Inside the conversion stage the pump pumps the first Stokes order via SRS, the first Stokes order pumps the second Stokes order, and so on. Highly reflective (HR) FBGs confine the power of all intermediate Stokes orders to the conversion stage and a partly reflective out-coupling (OC) FBG at the n -th Stokes order couples out a part of the corresponding power. The utilized fiber in the Raman conversion stage can either be a standard single-mode fiber or a specially fabricated Raman fiber with a comparably high Raman gain. The obtainable frequency shift from each Stokes order to the next order is determined by the specific fiber type under use. Standard passive germanosilicate fibers provide a quite broad (up to 40 THz) SRS gain spectrum that has a maximum at around 13.2 THz with respect to the frequency of the pump source. Thus, if pumped at 1064 nm, the obtainable Stokes orders of a corresponding CRFL are at around 1117 nm, 1180 nm, 1240 nm, 1310 nm, 1390 nm, 1480 nm, and so on.

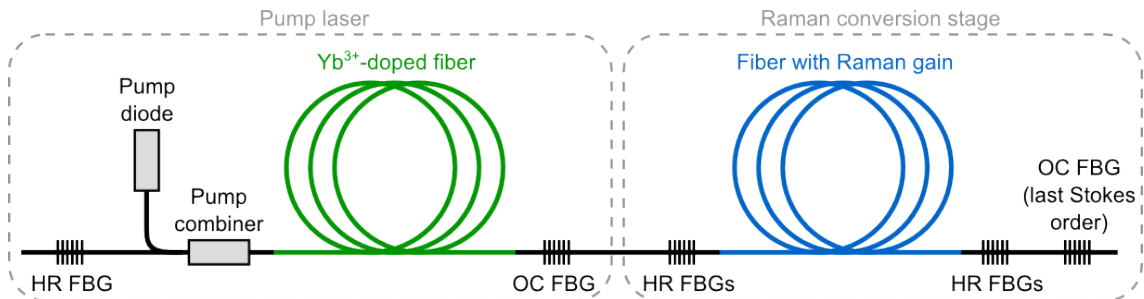


Figure 6.1: Schematic setup of a cascaded Raman fiber laser that consists of an Yb^{3+} -doped pump laser and a Raman conversion stage.

In particular the output power level of CRFLs at 1480 nm has been scaled significantly during the last years. Early experimental investigations were restricted by the onset of lasing at the parasitic Stokes order at around 1580 nm and the achievable output power at 1480 nm was limited to some tens of Watts [Emo07]. However, by appropriate design of the wavelength-dependent loss of the fiber under use the parasitic Stokes order can be suppressed significantly and output power levels of around 100 W at 1480 nm are possible with such fibers [Sup12b]. Further scaling of the output power became feasible with a hybrid CRFL and amplifier design [Sup13b]. With this design the output power at 1480 nm

was scaled to a record of 301 W [Sup13a]. Another prominent example for the application of Raman fiber laser systems are high-power combined Raman and Yb³⁺-doped fiber amplifiers at 1120 nm [Zha14a; Zha14b], which can be used to pump single-frequency Raman amplifiers at 1180 nm and subsequent frequency doubling to 589 nm for laser guide star applications in ground-based space observatories [Zha13; Zha14c]. Yet another example are ultra-long Raman fiber lasers with cavity lengths of several hundreds of kilometers for sensing applications [Mar11]. Furthermore, the molecular fingerprint region, i.e. the wavelength regime above 3.0 μm , can be reached with Raman fiber lasers based on fluoride [For12], chalcogenide [Ber14], and tellurite [Zhu15] fibers.

In the following section it is explained how CRFLs can be described mathematically. Furthermore, it is presented how they can be studied with numerical methods, in particular because an analytical solution, which corresponds for example to the steady state power levels of the Stokes orders within the Raman conversion stage, does not exist. In addition, numerical results regarding an exemplary CRFLs at 1480 nm based on a germanosilicate fiber are presented and evaluated.

6.1.1 Numerical Investigations

The steady-state power evolution of the pump, the different Stokes orders, and the parasitic Stokes order in an n-th order CRFL is governed by a system of $2(n+1)+1$ coupled differential equations [Agr01]

$$\begin{aligned} \frac{dP_0}{dz} &= -\frac{\nu_0}{\nu_1} g_0 (P_1^+ + P_1^- + 2\beta_1) P_0 - \alpha_0 P_0 \\ \pm \frac{dP_i^\pm}{dz} &= -\frac{\nu_i}{\nu_{i+1}} (P_{i+1}^+ + P_{i+1}^- + 2\beta_{i+1}) P_i^\pm - \alpha_i P_i^\pm \\ &\quad + g_{i-1} (P_{i-1}^+ + P_{i-1}^-) (P_i^\pm + \beta_i) \end{aligned} \quad (6.1)$$

for the pump power P_0 and the power P_i^\pm of all Stokes orders ($i = 1, \dots, n+1$). Note that $P_{i+1}^\pm \equiv 0$ for $i = n+1$. The superscripted \pm indicates either forward (+) or backward (-) propagation and α_0 or α_i is either the linear loss of the pump or the loss of the i-th Stokes order. The term

$$\beta_i = (1 + \eta) h\nu_i B_{\text{eff},i} \quad (6.2)$$

represents the spontaneous Raman effect and generates noise that is used as starting point in the numerical simulations. h is Planck's constant and ν_i the frequency of the i-th Stokes order. $B_{\text{eff},i}$ is the effective bandwidth at the i-th Stokes order and is either given

by the bandwidth of the corresponding FBGs or, at the parasitic Stokes order, by the bandwidth of the SRS process. The spontaneous Raman effect depends on the thermal phonon occupancy [Bur04]

$$\eta = \left(\exp \left(\frac{h\Delta\nu}{k_b T} \right) - 1 \right)^{-1} \quad (6.3)$$

where k_b is the Boltzmann constant, T the temperature, and $\Delta\nu$ the Raman frequency shift. If the Raman gain g_α at some wavelength λ_α is known, the Raman gain coefficient at the i -th Stokes order with wavelength λ_i is given by

$$g_i = \frac{\lambda_\alpha A_\alpha}{\lambda_i A_i} g_\alpha. \quad (6.4)$$

The effective interaction area

$$A_i = \pi W_i^2 \quad (6.5)$$

is related to the mode field radius

$$W_i \approx \left(0.65 + \frac{1.619}{V_i^{3/2}} + \frac{2.879}{V_i^6} \right) r_c \quad (6.6)$$

and can be calculated if the core radius r_c and the V -parameter of the fiber under use are known. Note that A_α corresponds to the effective interaction area at the wavelength λ_α .

The launched pump power and the FBGs of the different Stokes orders at the beginning ($z = 0$) and the end ($z = L$) of the fiber impose additional boundary conditions

$$\begin{aligned} P_0(z = 0, t) &= P_{\text{pump}}(t) \\ P_i^+(z = 0, t) &= R_{\text{left}, i} P_i^-(z = 0, t) \\ P_i^-(z = L, t) &= R_{\text{right}, i} P_i^+(z = L, t) \end{aligned} \quad (6.7)$$

where $R_{\text{left}, i}$ and $R_{\text{right}, i}$ are the reflectivities of the left and right FBGs at the i -th Stokes order. Ideally, the forward and backward propagating power of the parasitic Stokes order does not experience any reflections. However, in every real experimental setup reflections cannot be suppressed completely. Thus, if the parasitic Stokes order should be included in the analysis, Eq. (6.7) must be extended by small reflections for the parasitic Stokes order.

Mathematically, Eqs. (6.1) and (6.7) constitute a boundary value problem (BVP). Without further approximations, see for example [Bur05a; Bur05b], an analytical solution

does not exist and numerical methods must be used. A lot of work has been contributed in the past to solve BVPs describing steady-state CRFLs numerically by self-written routines that relied on different numerical approaches, see for example [Tar09] and references within. A common approach for BVPs and in particular for CRFLs is the *shooting method*¹ [Jac01]. First, the BVP is transformed to an initial value problem with a guess for the unknown functions at the beginning of the spatial interval of interest. Then, the corresponding differential equations are integrated over the interval and boundary conditions are applied at the end of the interval. Afterwards, the differential equations are integrated again towards the beginning of the interval, where again the boundary conditions are applied. The result of this procedure is then compared to the initial guess, corrections are applied, and the procedure starts again with an updated guess. Thus, this approach converges in an iterative process towards a solution of the BVP. Note that the integration is not performed explicitly but implicitly by an appropriate sampling of the interval and subsequent solving of a nonlinear equation system that is determined by the sampling points and the differential equations. The original routine applied in [Jac01] was written in Fortran and is part of a more general shooting method BVP solver [Sha06]. The numerical simulations described and evaluated in the following were performed with a wrapped Python version of the original Fortran BVP solver [Sal12].

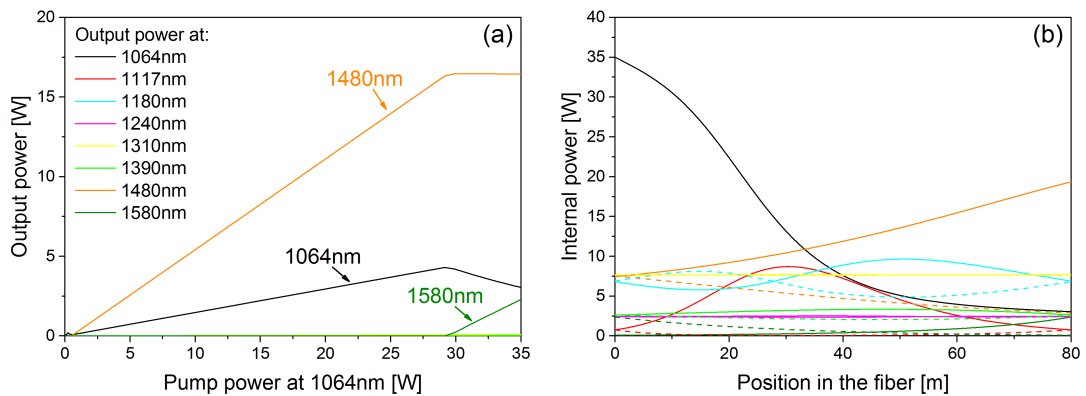


Figure 6.2: (a): Simulated slope of a cascaded Raman fiber laser at 1480 nm with an additional parasitic Stokes order at 1580 nm. Note that the laser was pumped at 1064 nm. (b): Corresponding internal power distribution in the Raman conversion stage. Solid lines: forward propagating fields. Dashed lines: backward propagating fields.

¹ This name references to the fact that it is similar to the problem of hitting a distant point with a cannon and that optimization can be performed by iteratively optimizing the initial parameters (up-tilt etc.) of the cannon.

Table 6.1: Parameters of the numerical simulation on an exemplary cascaded Raman fiber laser at 1480 nm with an additional parasitic Stokes order at 1580 nm.

Parameter	Value	Note
L	80 m	Raman fiber length
r_{core}	1.65 μm	Core radius of the Raman fiber
NA	0.26 μm	Core NA of the Raman fiber at 1064 nm
g_0	0.0025 $\frac{1}{\text{mW}}$	Raman gain coefficient at 1550 nm
R_{HR}	0.99	Reflectivity of the highly reflective FBGs
R_{OC}	0.15	Reflectivity of the 1480 nm output coupler
$R_{\text{parasitic}}$	0.04	Parasitic reflectivities at 1580 nm
$\Delta\nu$	13.24 THz	Raman frequency shift
B_{eff}	0.2 THz	Effective bandwidth at all Stokes orders
$B_{\text{eff,parasitic}}$	10.0 THz	Effective bandwidth at the parasitic Stokes order
T	295 K	Temperature (in the fiber core)

In Fig. 6.2 the results of a numerical simulation of an exemplary CRFL at 1480 nm with an additional parasitic Stokes order at 1580 nm, which was pumped at 1064 nm, are presented. The most important simulation parameters are listed in Tab. 6.1. All parameters related to the Raman fiber were determined by the specifications (the datasheet) of a commercially available Raman fiber from OFS (Norcross, GA, USA) as this fiber was used in all experiments presented in the following sections. The particular slope of the CRFL presented in Fig. 6.2 (a) represents one of the major limitations regarding the power scaling of CRFLs, namely the onset of lasing at the parasitic Stokes order. It is not only reported for germanosilicate CRFLs at 1480 nm [Emo07] but also for example for a phosphosilicate¹ Raman fiber laser at 1248 nm [Xio03]. The lasing of the parasitic Stokes order decreases the slope efficiency of the main Stokes order and limits the achievable output power. Indeed, the actual threshold for the onset of lasing at the parasitic Stokes order can be influenced by the cavity design. For example, by minimizing the back-reflections and the intra-cavity power of the main Stokes order or by keeping the fiber short, the threshold can be increased. However, all these approaches will also somehow limit the achievable output power at the main Stokes order. As mentioned earlier, a specially designed Raman fiber

¹ The strong P_2O_5 molecular vibrations in phosphosilicate fibers allow for a comparably large and strong Stokes shift of around 40 THz. Thus, phosphosilicate fibers allow for a significantly simplified cascaded Raman laser setups [Kar00], but they are not that common in comparison with germanosilicate fibers.

with a significantly increased loss at the parasitic Stokes order can be used to overcome this limitation [Sup12b]. However, as this fiber is not commercially available, it cannot be considered as a general workaround.

A more easily accessible solution was investigated in [Sup13b] and is illustrated by the numerical results presented in Fig. 6.3. The length of the Raman fiber was shortened to 20 m and the maximum pump power at 1064 nm was limited to 2 W. In addition, a 600 m long piece of Raman fiber was used behind the CRFL as a single-pass Raman fiber amplifier, which was seeded by the output of the CRFL and pumped at 1064 nm with a power of 33 W. Note that the combined pump power of the CRFL and the amplifier was 35 W and therefore equal to the pump power used in the simulations presented before. All other parameters, e.g. the Raman gain, were not changed. At the highest pump power of 2 W and due to the small residual transmission of the HR FBGs, the CRFL emits at all Stokes orders. Thus, the Raman fiber amplifier is seeded at all Stokes orders and along the 600 m long Raman fiber amplifier each Stokes order (starting with the pump) is converted to the next Stokes order by the SRS process. At around 550 m the Stokes order at 1480 nm starts to pump the parasitic Stokes order at 1580 nm, but this can be avoided by cutting the Raman fiber for example at around 450 m. Then, in contrast to the single CRFL presented earlier, the CRFL in combination with the Raman fiber amplifier would not be limited by the onset of the parasitic Stokes order and the maximum obtainable output power at 1480 nm is increased. Note that the actual Raman fiber used for the experimental proof-of-principle of this approach presented in [Sup13b] was the same as it was used in [Sup12b], i.e. the wavelength-dependent loss was designed such that the parasitic Stokes

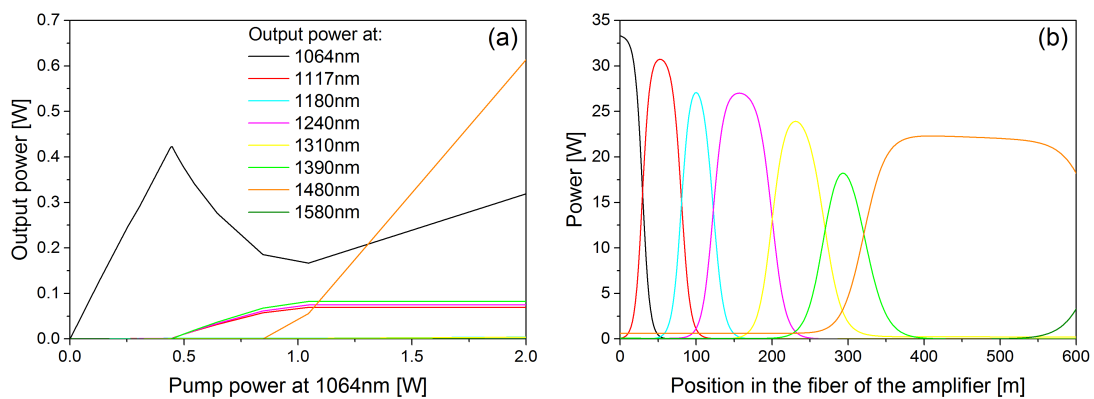


Figure 6.3: Simulation results of a cascaded Raman fiber laser at 1480 nm in combination with a single-pass Raman fiber amplifier that is seeded by the output of the Raman fiber laser. (a): Slope of the cascaded Raman fiber laser. (b): Internal power distribution of the Raman fiber amplifier at the highest pump power of the laser and the amplifier.

order was suppressed. However, the numerical results presented above suggest that this is most probably not necessary as the fiber just has to have the correct length. Furthermore, the higher the pump power of the amplifier, the shorter the Raman fiber amplifier can be and the hybrid CRFL and Raman fiber amplifier approach becomes even more attractive for compact all-fiber based systems.

6.1.2 Experimental Results

Yb^{3+} -doped fibers are known to provide high gain levels at around 1064 nm. Thus, it appears to be logical to use Yb^{3+} -doped fiber lasers at 1064 nm as pump sources for CRFLs at 1480 nm, as it was assumed for the simulations presented in the previous section. However, as shown in the following, this choice of the pump wavelength induces some serious problems regarding the power scaling capabilities of the Raman conversion stage.

In Fig. 6.4 the experimental setup of a single-stage Raman fiber laser at 1117 nm, which was pumped by an Yb^{3+} -doped fiber laser 1064 nm, is presented. The pump laser consisted of a 12 m long single-mode Yb^{3+} -doped double-clad fiber (SM-YDF-5/130-VIII from Nufern) that was pumped by two 25 W multimode diodes at 976 nm. The reflectivity of the HR FBG at 1064 nm was 99 %, the reflectivity of the OC FBG was 6 %, and the -3 dB bandwidth of each FBG was around 1 nm. Note that all FBGs that have been used within the frame of this thesis were fabricated by AOS (Dresden, Germany). When the Raman conversion stage was detached, the Yb^{3+} -doped pump laser provided a maximum output power of 31 W at a pump power of 50 W. The Raman conversion stage consisted of a 30 m long Raman fiber from OFS and a 99 % and a 6 % FBG at 1117 nm, each also with a -3 dB bandwidth of around 1 nm.

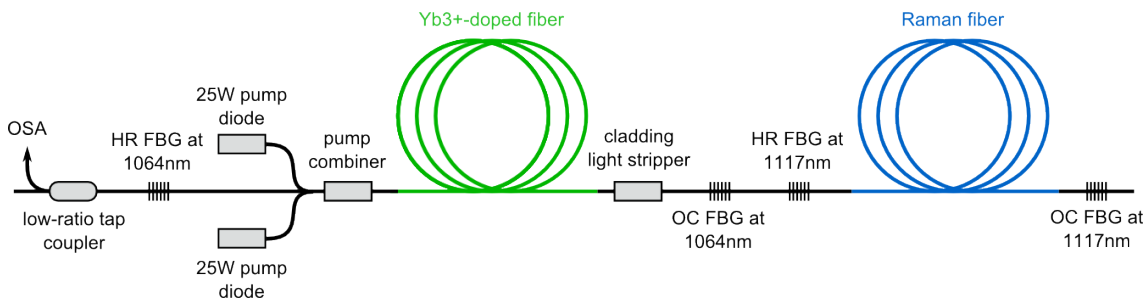


Figure 6.4: Experimental setup of the single-stage Raman fiber laser at 1117 nm, which was pumped by an Yb^{3+} -doped fiber lasers at 1064 nm. OSA: optical spectrum analyzer.

After the Yb^{3+} -doped pump laser was spliced to the Raman conversion stage and when the pump power was increased, lasing at 1117 nm could be observed in the optical spectra. However and in particular compared to a corresponding numerical simulation, the achieved output power levels were extraordinarily low. Thus, a low-ratio tap coupler was

integrated behind the pump laser (see Fig. 6.4) and the optical spectra in backward direction were analyzed. It was observed that some power at 1117 nm was leaking from the Raman conversion stage through the corresponding HR FBG into the Yb³⁺-doped pump laser. The optical spectra in combination with an appropriate power head were also used to calculate the backward propagating power levels at 1064 nm and 1117 nm. The corresponding result is presented in Fig. 6.5. Not surprisingly, the backward propagating power at 1117 nm was amplified in the Yb³⁺-doped pump laser. However, this amplification process was so strong and decreased the gain of the pump laser at 1064 nm so much that the backward propagating signal and therefore also the output power at 1064 nm decreased significantly. Thus, less pump power at 1064 nm was available to pump the Raman conversion stage and this certainly explains the observed low output power levels of the Raman fiber laser at 1117 nm. Indeed, a 1064/1117 nm WDM could have been used between the pump laser and the Raman conversion stage to filter out any backward propagating power at 1117 nm before it can enter the pump laser. However, this approach would have required a WDM that can handle the corresponding power levels and does not introduce significant losses at 1064 nm. Another possible solution was to change the wavelength of the Yb³⁺-doped pump laser to 1117 nm. This approach has two obvious major advantages. First, any backward propagating power at the next Raman wavelength of 1180 nm is not amplified in the pump laser as the corresponding emission cross sections are just too small. Furthermore, in a CRFL at 1480 nm the actual number of Stokes shifts is decreased by one and the overall efficiency of the Raman conversion stage is most probably increased because one pair of FBGs can be omitted that might cause otherwise additional losses due to inadequate splices or unequal spectral reflections. In addition, Yb³⁺-doped fiber lasers work well at

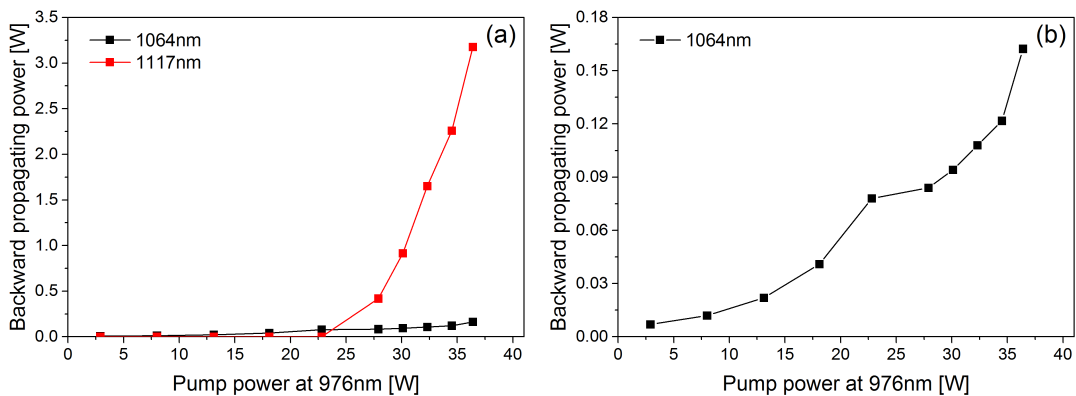


Figure 6.5: Backward propagating power behind the 1064 nm Yb³⁺-doped pump laser of the single-stage Raman fiber laser at 1117 nm. (a): 1064 nm and 1117 nm. (b): Only 1064 nm.

1117 nm, although the emission cross section is significantly smaller than for 1064 nm. Just by changing the 1064 nm FBGs to FBGs at 1117 nm with the same specifications, the Yb^{3+} -doped pump laser still provided a maximum output power of 28.5 W at a pump power of 50 W. Indeed, optical spectra indicated a noticeable amount of ASE at around 1075 nm, but the signal-to-ASE suppression was better than 30 dB (0.5 nm RBW). Thus, for all experiments and numerical simulations presented in the following sections, Yb^{3+} -doped pump lasers at 1117 nm were used. Although not discussed explicitly in the literature, the reported problems related to a pump wavelength of 1064 nm most certainly explain the common choice of pump lasers at 1117 nm to scale the output power of CRFLs at 1480 nm, see for example [Sup13a].

A common approach for the inscription of a FBG in an optical fiber is the phase-mask technique, i.e. the inscription of the FBG via a interference pattern, which is induced by a phase mask that acts as a diffractive element for a UV laser. A detailed description of this method and other relevant aspects of FBGs can be found in [Oth99]. Several models to describe the chemical processes during the inscription have been developed and most of them deal with various mechanisms such as photochemistry, which are mainly related to the bleaching of defects in the glass host. The bleaching causes changes in the UV absorption spectra and a refractive index modulation, i.e. the FBG, is imprinted via the Kramers-Kronig relation. To obtain a significantly large refractive index modulation the fiber has to be photosensitive, i.e. sensitive to the UV laser radiation. Due to the common codoping of the cores in fused silica fibers, e.g. with GeO_2 , they are already quite photosensitive. Nevertheless, some techniques have been developed to increase the photosensitivity and to accelerate the FBG inscription. One highly efficient method is the hydrogenation prior to the inscription process, i.e. the loading of the fiber with molecular hydrogen by soaking it in hydrogen gas at temperatures up to 100 °C and pressures of some hundreds atm. It is known that the hydrogenation leads to strong absorption bands of molecular hydrogen and OH species [Nog85]. In particular a strong absorption of molecular hydrogen at around 1.24 μm can be critical for CRFLs at 1480 nm because the Stokes order at 1240 nm coincides with this absorption. Indeed, not only the FBGs at 1240 nm are potentially affected but all FBGs that experience significant power at 1240 nm. Therefore, it was investigated within the frame of this thesis if the hydrogenation with molecular hydrogen leads to any limitations of silica-based CRFLs at 1480 nm and how they can be avoided.

As depicted in Fig. 6.6, a low-ratio tap coupler behind a two-stage Raman fiber laser at 1180 nm and 1240 nm was used to analyze the optical spectra of the laser. The Raman conversion stage was pumped by an Yb^{3+} -doped fiber laser at 1117 nm, the length of the

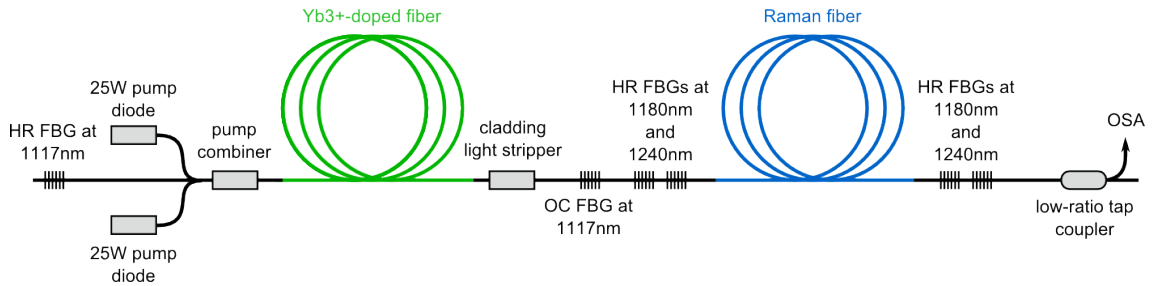


Figure 6.6: Experimental setup that was used to investigate the performance of the fiber Bragg gratings loaded with hydrogen or deuterium. OSA: optical spectrum analyzer.

Raman fiber from OFS was 30 m, and the reflectivity of the FBGs at 1180 nm and at 1240 nm was 99 %, each with a -3 dB bandwidth of around 1 nm. The individual FBGs were arranged such that the 1180 nm FBGs were located innermost, surrounded by the 1240 nm FBGs. In addition, two sets of FBGs were tested. One set was loaded with hydrogen and the other set was soaked in deuterium as it also increases the photosensitivity but does not introduce the strong absorption at around 1240 nm. The optical spectra of the first Stokes order at 1180 nm at different pump power levels are presented in Fig. 6.7. The spectra presented in Fig. 6.7 (a) correspond to the FBGs loaded with hydrogen and a significant wavelength drift can be observed. The spectra presented in Fig. 6.7 (b) correspond to the FBGs soaked in deuterium and no drift is present at all. Note that the same tendency was observed for the FBGs at 1240 nm. After the FBGs at 1240 nm were detached from the setup, in both cases (hydrogen and deuterium loaded FBGs) no drift of the Stokes order at 1180 nm appeared. Thus, the observed drift was definitely related to the hydrogen absorption at 1240 nm and a corresponding thermal heating, which is known to cause drifts of the center wavelengths [Oth99]. As these drifts can cause a spectral mismatch among the FBGs of a certain Stokes order, FBGs loaded with deuterium are more suitable for high-power CRFLs than FBGs loaded with hydrogen.

6.1.3 Conclusion

Several detrimental effects affect the power scaling capabilities of CRFLs at 1480 nm. The onset of lasing at the parasitic Stokes order will always somehow limit the achievable output power level, in particular if a configuration is used that is prone to reflections. However, as shown in the literature and as confirmed by the presented numerical results, a hybrid laser and amplifier configuration is a promising concept to avoid the excessive generation of power at the parasitic Stokes order. In addition, this scheme does not necessarily require a specially designed Raman fiber with an increased loss at the parasitic Stokes order. Thus, commercially available Raman fibers might be used instead. Most commonly,

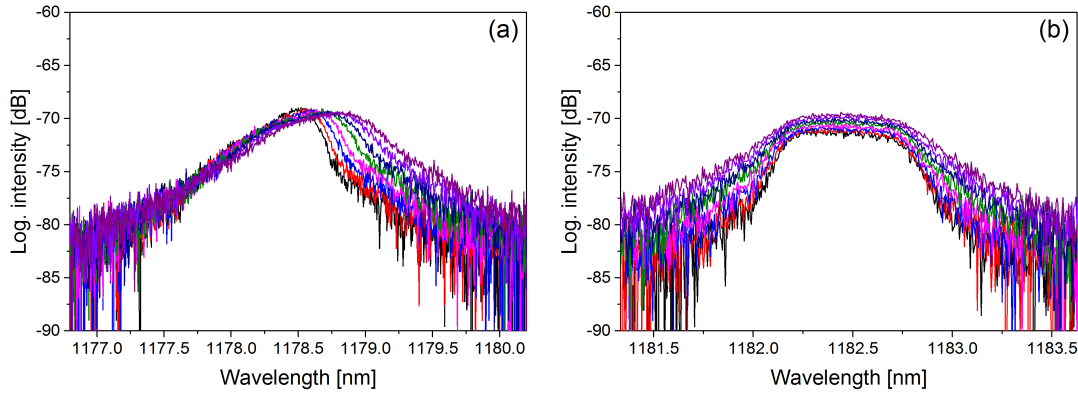


Figure 6.7: Spectra of the first Stokes order at 1180 nm of a two-stage Raman fiber laser at different pump power levels. (a): Fiber Bragg gratings loaded with hydrogen. (b): Fiber Bragg gratings loaded with deuterium.

pump lasers at 1117 nm are used to scale the output power of CRFLs at 1480 nm and this choice of the pump wavelength is explained by a harmful amplification processes at around 1117 nm if a pump laser at 1064 nm is used. As presented, Yb^{3+} -doped fiber lasers work well at 1117 nm and they also allow to reduce the actual number of Stokes shifts by one. The hydrogenation of the FBGs, which is used to increase their photosensitivity, can induce thermal drifts of the corresponding center wavelengths, especially if it is performed with hydrogen. Induced spectral mismatches between pairs of FBGs certainly affect the obtainable efficiencies. Therefore, FBGs loaded with deuterium should be used instead because they do not introduce the strong absorption at around 1240 nm.

It is well-known that FWM between different longitudinal modes of the Raman conversion stage leads to a strong spectral broadening at all Stokes orders. As this broadening reduces the effective reflectivities of the FBGs, it affects the conversion efficiency from each Stokes order to the next. Thus, the FWM effect is quite detrimental for the power scaling of CRFLs at 1480 nm. It was for example estimated during some experiments performed in the frame of this thesis that the reflectivities of the HR FBGs decreased by some tens of percent. However, this particular effect is not analyzed in detail here since the available literature on this subject is very versatile, see for example [Lab80] and [Kar00] for experimental investigations, [Bab07] and references within for theoretical studies, and [Hag07] for a numerical investigation.

6.2 Passive Pump-to-Stokes Noise-Transfer Suppression

As mentioned earlier, the onset of lasing at the parasitic Stokes order can be exploited to achieve a passive pump-to-Stokes noise transfer suppression. The idea behind this approach

is depicted schematically in Fig. 6.8. Below the threshold of the parasitic Stokes order a certain change of pump power induces a corresponding change of the output power at the main Stokes order and above the threshold the magnitude of this effect is decreased. Therefore, transfer of noise from the pump to the main Stokes order is suppressed. This scheme becomes very interesting if the CRFL is for example designed such that the parasitic Stokes order starts to lase slightly below the maximum pump power. Then, the maximum output power at the main Stokes order is just slightly reduced, but the passive noise transfer suppression still occurs.

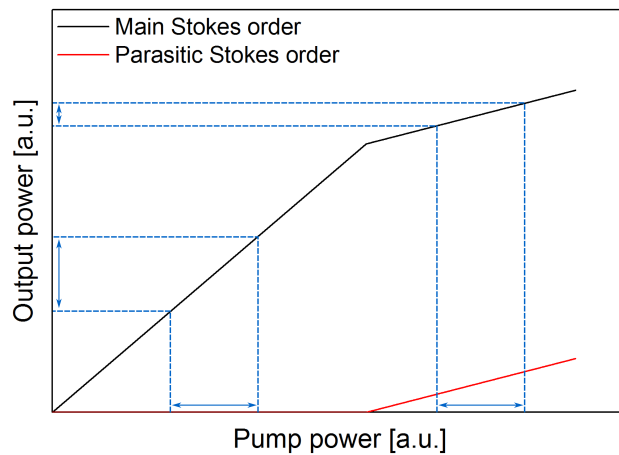


Figure 6.8: Exemplary slope of the main and the parasitic Stokes order of a cascaded Raman laser and how it can be exploited to achieve a passive pump-to-Stokes noise transfer suppression.

A first experimental proof-of-principle of the passive noise transfer suppression in a two-stage CRFL at 1180 nm and 1240 nm is presented and analyzed in section 6.2.2, but first numerical and experimental studies on the gain dynamics in a single-stage Raman fiber laser at 1180 nm are presented because the corresponding results are important for understanding the gain dynamics in the two-stage Raman fiber laser and the passive noise transfer suppression. In addition, such an investigation was missing in the literature, so far. Similar to the previous chapter, the gain dynamics were analyzed by means of the complex transfer functions of the system, i.e. the frequency-dependent transfer of pump power noise to the main Stokes orders. To the best of the author's knowledge, analytical solutions of these transfer functions do not exist and numerical methods must be used instead. The numerical approach presented in the following was already used to determine the characteristic noise transfer in a Raman fiber laser at frequencies in the order of multiples of the cavity's free spectral range [Kra06]. For this thesis, the analysis has been limited

to the frequency domain of 10 Hz-1 MHz as it contains the most interesting dynamical features. Furthermore, higher frequencies are not relevant for GWDs.

6.2.1 Gain Dynamics in Raman Fiber Lasers

If also the time evolution of the Stokes fields in a CRFL is of interest, corresponding time derivatives must be included in the differential equations given by Eq. (6.1) [Agr01]

$$\begin{aligned} \frac{dP_0}{dz} + \frac{1}{c_0} \frac{\partial P_0}{\partial t} &= -\frac{\nu_0}{\nu_1} g_0 (P_1^+ + P_1^- + 2\beta_1) P_0 - \alpha_0 P_0 \\ \pm \frac{dP_i^\pm}{dz} + \frac{1}{c_i} \frac{\partial P_i^\pm}{\partial t} &= -\frac{\nu_i}{\nu_{i+1}} (P_{i+1}^+ + P_{i+1}^- + 2\beta_{i+1}) P_i^\pm - \alpha_i P_i^\pm \\ &\quad + g_{i-1} (P_{i-1}^+ + P_{i-1}^-) (P_i^\pm + \beta_i) \end{aligned} \quad (6.8)$$

where c_0 and c_i are the propagation velocities of the pump and the i -th Stokes order in the fiber. In order to obtain the transfer functions it is useful to consider a small sinusoidal modulation of the input pump power

$$\begin{aligned} P_{\text{pump}}(t) &= P_{\text{pump}}^0 (1 + \delta e^{i\omega t}) \\ &= P_{\text{pump}}^0 + p_{\text{pump}}(t) \end{aligned} \quad (6.9)$$

with a small modulation depth δ . Then, a corresponding ansatz can be made for the pump power and for the power of all Stokes orders within the Raman conversion stage

$$\begin{aligned} P_0(z,t) &= P_0^0(z) \left(1 + \delta_0 e^{i(\omega t + \phi_0)}\right) \\ &= P_0^0(z) + p_0(z,t) \\ P_i^\pm(z,t) &= P_i^{\pm,0}(z) \left(1 + \delta_i^\pm e^{i(\omega t + \phi_i^\pm)}\right) \\ &= P_i^{\pm,0}(z) + p_i^\pm(z,t) \end{aligned} \quad (6.10)$$

where a superscripted 0 always indicates the corresponding steady state solution. By substitution of Eq. (6.10) in Eq. (6.8) and by neglecting higher order terms with respect

to the modulation depths one obtains

$$\begin{aligned}
\frac{dp_0}{dz} &= \left(-\frac{\nu_0}{\nu_1} g_0 \left(P_1^{+,0} + P_1^{-,0} + 2\beta_1 \right) - \alpha_0 - \frac{i\omega}{c_0} \right) p_0 \\
&\quad - \frac{\nu_0}{\nu_1} g_0 P_0^0 \left(p_{i+1}^+ + p_{i+1}^- \right) \\
\pm \frac{dp_i^\pm}{dz} &= \left(g_{i-1} \left(P_{i-1}^{+,0} + P_{i-1}^{-,0} \right) - \frac{\nu_i}{\nu_{i+1}} g_i \left(P_{i+1}^{+,0} + P_{i+1}^{-,0} + 2\beta_{i+1} \right) - \alpha_i - \frac{i\omega}{c_i} \right) p_i^\pm \\
&\quad - \frac{\nu_i}{\nu_{i+1}} g_i P_i^{\pm,0} \left(p_{i+1}^+ + p_{i+1}^- \right) + g_{i-1} \left(P_i^{\pm,0} + \beta_i \right) \left(p_{i-1}^+ + p_{i-1}^- \right).
\end{aligned} \tag{6.11}$$

As these equations are linear in p_0 and p_i^\pm , the Fourier transformations

$$\begin{aligned}
\tilde{p}_0(z, \omega) &= \int dt p_0(z, t) e^{-i\omega t} \\
\tilde{p}_i^\pm(z, \omega) &= \int dt p_i^\pm(z, t) e^{-i\omega t}
\end{aligned} \tag{6.12}$$

also satisfy the PDE system given by Eq. (6.8) and one finally obtains

$$\begin{aligned}
\frac{d\tilde{p}_0}{dz} &= \left(-\frac{\nu_0}{\nu_1} g_0 \left(P_1^{+,0} + P_1^{-,0} + 2\beta_1 \right) - \alpha_0 - \frac{i\omega}{c_0} \right) \tilde{p}_0 - \frac{\nu_0}{\nu_1} g_0 P_0^0 \left(\tilde{p}_1^+ + \tilde{p}_1^- \right) \\
\pm \frac{d\tilde{p}_i^\pm}{dz} &= \left(g_{i-1} \left(P_{i-1}^{+,0} + P_{i-1}^{-,0} \right) - \frac{\nu_i}{\nu_{i+1}} g_i \left(P_{i+1}^{+,0} + P_{i+1}^{-,0} + 2\beta_{i+1} \right) - \alpha_i - \frac{i\omega}{c_i} \right) \tilde{p}_i^\pm \\
&\quad - \frac{\nu_i}{\nu_{i+1}} g_i P_i^{\pm,0} \left(\tilde{p}_{i+1}^+ + \tilde{p}_{i+1}^- \right) \\
&\quad + g_{i-1} \left(P_i^{\pm,0} + \beta_i \right) \left(\tilde{p}_{i-1}^+ + \tilde{p}_{i-1}^- \right)
\end{aligned} \tag{6.13}$$

with corresponding boundary conditions

$$\begin{aligned}
\tilde{p}_0(z=0, \omega) &= \tilde{p}_{\text{pump}}(\omega) \\
\tilde{p}_i^+(z=0, \omega) &= R_{\text{left}, i} \tilde{p}_i^-(z=0, \omega) \\
\tilde{p}_i^-(z=L, \omega) &= R_{\text{right}, i} \tilde{p}_i^+(z=L, \omega).
\end{aligned} \tag{6.14}$$

Eqs. (6.13) and (6.14) constitute a $2n+1$ -dimensional complex BVP, which can be transferred to a $2(2n+1)$ -dimensional real BVP by using the real and imaginary parts. If the steady state solutions are known, Eqs. (6.13) and (6.14) can be used to calculate the transfer functions of the CRFL by comparing the input and output magnitudes and phases of the complex solutions.

Computed transfer functions of a single-stage Raman fiber laser at 1180 nm between

10 Hz and 1 MHz are presented in Fig. 6.9. The laser was pumped at 1117 nm, the Raman fiber length was 50 m and the reflectivity of the 1180 nm OC FBG was 80 %. The magnitude of each transfer function is flat at low frequencies and falls off with 10 dB per decade at high frequencies. This behavior corresponds to a low-pass and is characterized by a corresponding -3 dB cut-off frequency. By fitting a low-pass to the data, the cut-off frequencies were determined to be around 100 kHz. The maximum phase shift of a low-pass is -90 degree, which is obviously not the case for the computed transfer functions. The additional phase shift is explained by runtime effects as the model (see Eq. (6.8)) and therefore also the simulation deals with a finite speed of propagation.

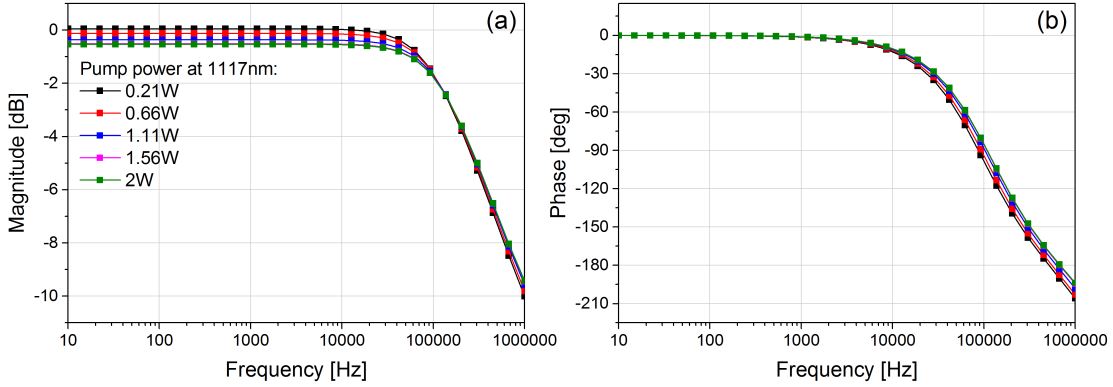


Figure 6.9: (a): Magnitude of computed transfer functions of a single-stage Raman fiber laser at 1180 nm that is pumped at 1117 nm. (b): Corresponding computed phase shift.

Although it is not possible to reduce the PDE system given by Eq. (6.8) to a purely time-dependent problem by analytical integration over the cavity, the observed low-pass behavior can be explained by making some analogies to *conventional* lasers, i.e. lasers whose dynamical properties are determined by a time-dependent interaction of the total laser field and a cavity-integrated atomic or molecular inversion. If the lifetime associated with the inversion of such a laser is much larger than the cavity lifetime (class B regime), the transfer function of the total laser field is given by a relaxation oscillation [Sie86]. Mathematically, it corresponds to a double low-pass with complex conjugated cut-off frequencies. However, if the lifetime of the inversion is not too large compared to the cavity lifetime (class A regime), the transfer function is given instead by a double low-pass with two distinct real cut-off frequencies. Although both cut-off frequencies depend on the operation point of the laser, i.e. how far the laser is operated above the threshold, the lower cut-off frequency is basically determined by the larger lifetime (in most cases the lifetime of the inversion) and the upper one is mainly related to the smaller lifetime (in most cases the lifetime of the cavity).

In a Raman fiber laser, like in any other laser, the cavity-integrated gain must be constant above the laser threshold as it must always compensate the total losses. As the gain in a Raman fiber laser is provided directly by the pump power and not by any inversion, it is the cavity-integrated average pump power that is constant above the threshold of the Stokes order. Therefore, the dynamical behavior of a Raman fiber laser can be understood as a time-dependent interaction between the Stokes-shifted average laser field and the average pump power, which plays the role of the inversion. Although no mathematical expressions for the associated lifetimes exist, it is reasonable to argue that they are of the same magnitude as both scale with the fiber length. However, due to the corresponding FBGs the Stokes photons are confined to the cavity longer than the pump photons and the lifetime of the Stokes-shifted average laser field is larger but not too large compared to the lifetime of the average pump power. Therefore, Raman fiber lasers can be categorized as class A regime lasers and the simulated transfer functions are the low-frequency parts of double low-passes. In analogy to *conventional* lasers, the observed cut-off frequency is basically related to the lifetime of the Stokes-shifted laser field and the second cut-off frequency is mainly determined by the lifetime of the averaged pump power. This lifetime is at least given by or even smaller than the cavity length divided by the propagation speed of the pump photons. Thus, the corresponding cut-off frequencies ($\gtrsim 6$ MHz for 50 m of Raman fiber) are of the same magnitude as multiples of the cavity's free spectral range. Therefore, they are superposed by corresponding additional peaks in the transfer function, as they have already been observed experimentally as well as numerically [Kra06] and an exact evaluation of these cut-off frequencies is not possible.

In Fig. 6.10 (a) the cut-off frequencies of the observed low-passes (see Fig. 6.9) are presented in dependency of the output power of the Raman fiber laser and for a varying reflectivity of the OC FBG. As a larger (smaller) reflectivity yields a longer (shorter) lifetime of the Stokes-shifted photons in the cavity, it also yields a smaller (larger) cut-off frequency. In Fig. 6.10 (b) the same cut-off frequencies are presented but for a varying Raman fiber length. Again, a longer (shorter) fiber length yields a longer (shorter) lifetime of the Stokes-shifted photons and therefore a smaller (larger) cut-off frequency.

In Fig. 6.11 the experimental setup is presented that was used to measure the transfer functions of a single-stage Raman fiber laser at 1180 nm. The Yb³⁺-doped pump laser consisted of a 12 m long 6 μ m Yb³⁺-doped double-clad fiber from Nufern and was pumped by a 25 W multimode diode at 976 nm. The HR FBG at 1117 nm had a reflectivity of 99 % and the OC FBG had a reflectivity of 6 %, each with a -3 dB bandwidth of around 1 nm. At a pump power of 18 W the pump laser provided an output power of around 7.2 W. The Raman conversion stage consisted of around 50 m Raman fiber from OFS. A HR FBG

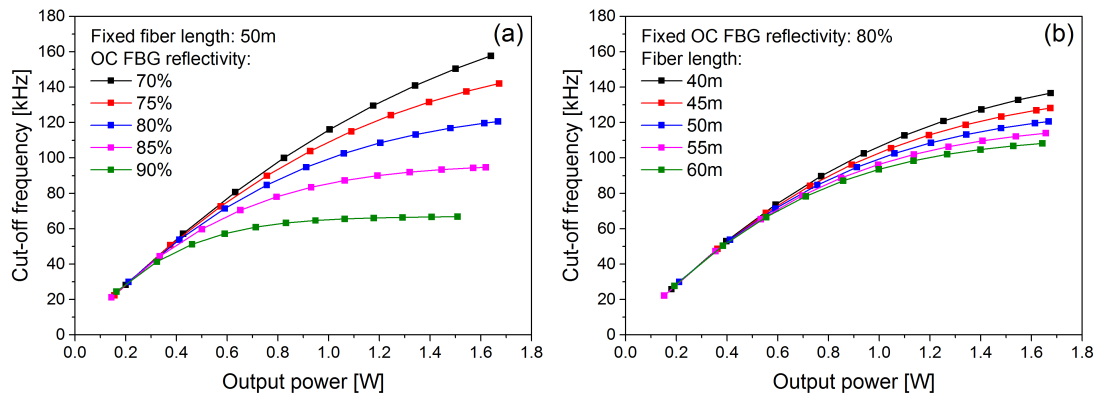


Figure 6.10: (a): Computed cut-off frequencies of the transfer functions of a Raman fiber laser at 1180 nm in dependency of the output power and for a varying reflectivity of the out-coupling fiber Bragg grating. (b): The same cut-off frequencies in dependency of a varying Raman fiber length.

with a reflectivity of 99% and an OC FBG with a reflectivity of 83%, each with a -3 dB bandwidth of 0.7 nm and a center wavelength of 1180 nm were used as a resonator for the Stokes-shifted power. Thus, the parameters of this Raman fiber laser were comparable to the parameters used in the simulations. At the output end of the Raman fiber laser an in-house made 1117/1180 nm WDM was used to separate the residual pump light from the laser output power at 1180 nm. The threshold pump power for the Raman fiber laser was 2.2 W and at a pump power of 7.2 W it provided an output power of 1.2 W at 1180 nm.

For the modulation measurements the current of the multimode 976 nm pump diode was modulated by a self-made current buffer that was connected in parallel to the DC current driver. A low-ratio tap coupler behind the pump laser was used as a reference for the induced modulation of the pump power. As the relaxation oscillation frequency of the pump laser was between 100 kHz and 500 kHz, a sufficiently large modulation depth up to

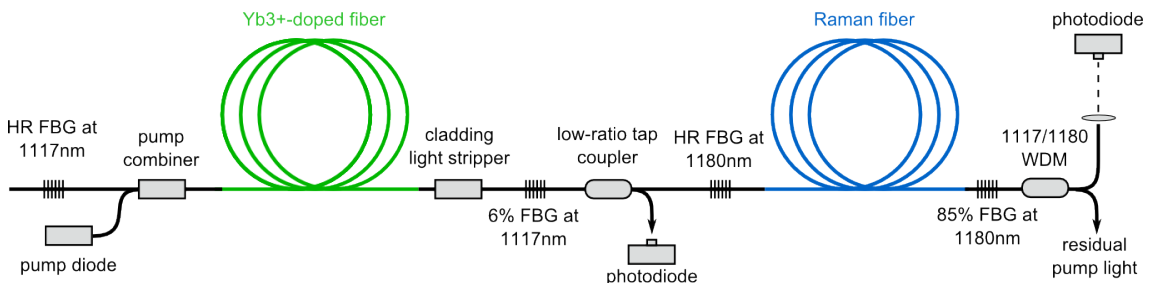


Figure 6.11: Schematic overview of the experimental setup used to measure the transfer functions of a Raman fiber laser at 1180 nm.

a modulation frequency of around 1 MHz could be achieved. The pump laser reference and a low-power sample of the output power at 1180 nm were detected by fast photodiodes, each with a bandwidth of 150 MHz. Sweeping of the pump power modulation frequency and recording of the corresponding transfer functions was performed with a dynamic signal analyzer.

The measured transfer functions between 1 kHz and 1 MHz at different output power levels of the Raman fiber laser are presented in Fig. 6.12. The increasing magnitude and phase shift at very high frequencies around 1 MHz are artifacts that are caused by the dynamic signal analyzer being unable to keep track of the signal for very small magnitudes. Nevertheless, the measured transfer functions definitely confirm the results of the numerical simulations presented before. However, fits of a low-pass to the data revealed that the experimental cut-off frequencies depend linearly on the output power in contrast to the saturation-like behavior of the numerically obtained cut-off frequencies (see Fig. 6.10). This behavior is explained by the intra-cavity FWM (see section 6.1.3) and the effective reflectivities of the FBGs that decrease with increasing output power. This effect was not included in the simulation, i.e. constant reflectivities have been assumed.

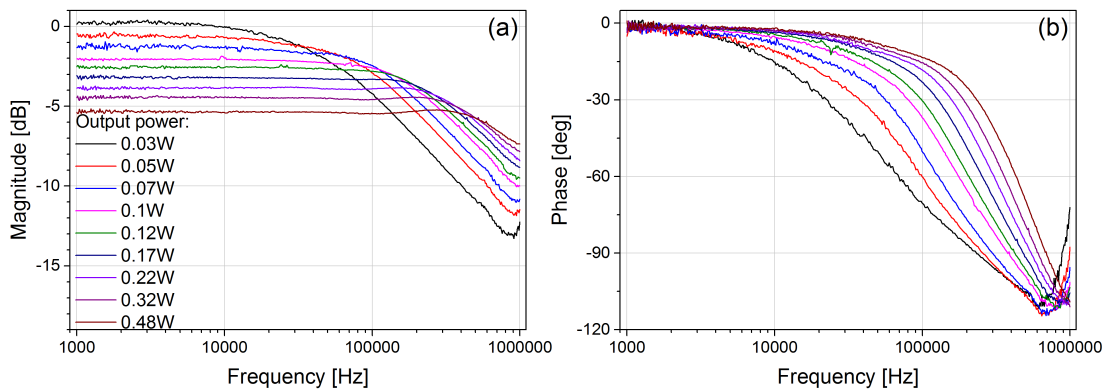


Figure 6.12: (a): Magnitude of measured transfer functions (not normalized) of the Raman fiber laser at 1180 nm for different output power levels. (b): Corresponding phase shift.

6.2.2 Raman Fiber Lasers with Parasitic Stokes Order

In Fig. 6.13 the experimental setup is presented that was used to confirm the passive pump-to-Stokes noise transfer suppression in a Raman fiber laser at 1180 nm with an additional parasitic Stokes order at 1240 nm. As before, the pump laser consisted of a 12 m long $6\ \mu\text{m}$ Yb^{3+} -doped single-mode double-clad fiber, but it was pumped this time by two 25 W multimode diodes at 976 nm. Thereby, the maximum output power at 1117 nm was increased to 27.5 W. The Raman fiber from OFS had a length of 30 m. Different in-house

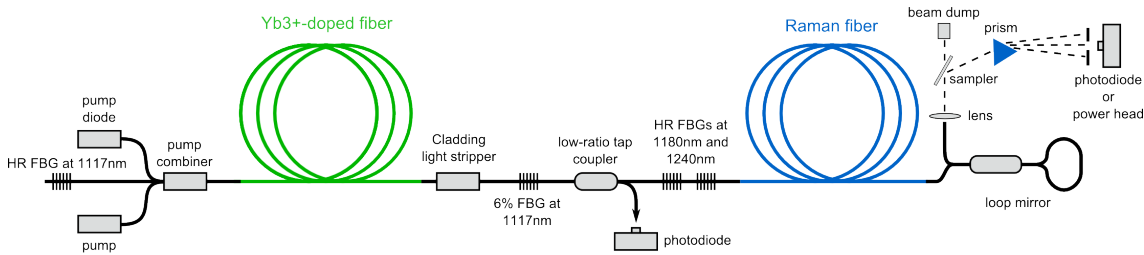


Figure 6.13: Schematic overview of the experimental setup used to confirm the passive pump-to-Stokes noise transfer suppression in a Raman fiber laser at 1180 nm with an additional parasitic Stokes order at 1240 nm.

made WDMs in loop-mirror configuration were tested as output couplers for both Stokes orders. The best results were achieved with a loop-mirror that had by design a reflectivity of 90 % at 1180 nm and 2 % at 1240 nm. As highly reflective counterparts at both Stokes orders FBGs with a reflectivity of 99 % and a -3 dB bandwidth of around 0.7 nm were used. At the output end of the Raman conversion stage a reference beam, which was sampled by an optical wedge, and a dispersive prism were used to separate the main Stokes order, the parasitic Stokes order, and the residual pump. Because the mirrors behind the prism introduced wavelength-dependent losses, the measured power ratios were certainly not the same as in the actual laser output. However, this was tolerable as only the relative change of the slope efficiency of the main Stokes order was of interest. As before, modulation of the pump power at 1117 nm was achieved by a self-made current buffer, which was connected in parallel to the DC current driver of the 976 nm pump diodes, and a low-ratio tap coupler behind the pump laser was used as a reference for the induced power modulation.

The measured power levels of both Stokes order behind the prism in dependency of the pump power and around the threshold of the Stokes order at 1240 nm are presented in Fig. 6.14 (a). At a pump power of around 11.5 W the parasitic Stokes order started to lase and simultaneously the slope efficiency of the main Stokes order at 1180 nm dropped by a factor of around 7.5. The magnitude of the measured transfer functions of the main Stokes order at different pump power levels below and above the threshold of the parasitic Stokes order is presented in Fig. 6.14 (b). Note that the transfer functions are only shown up to a frequency of 100 kHz, although measurements up to 1 MHz would have been feasible. Unfortunately, the loop-mirror introduced some non-linear feedback at the wavelength of the pump laser, in particular at modulation frequencies of more than 100 kHz. As the influence of this feedback on the transfer functions between 100 kHz and 1 MHz is unclear, this part of the transfer functions is omitted. Nevertheless, the passive noise transfer suppression is clearly present and the suppression tap factor of around 8.7 dB is as expected

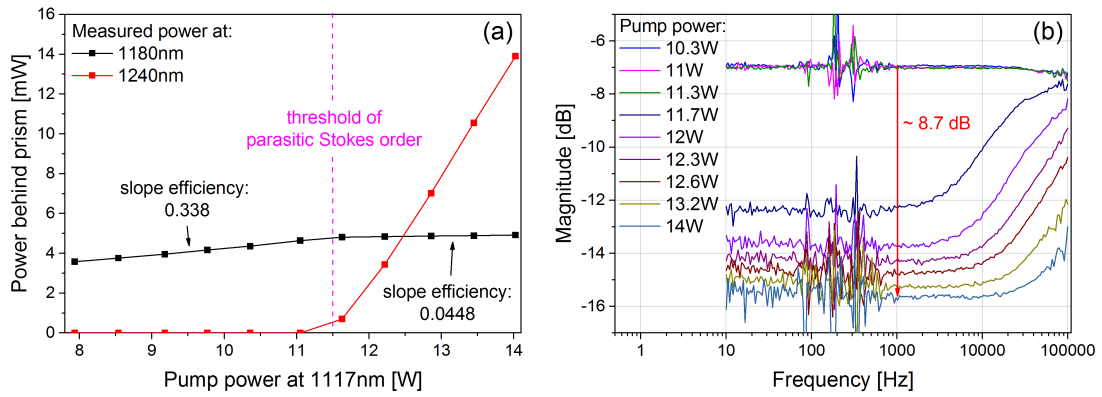


Figure 6.14: (a): Measured power levels of a Raman fiber laser at 1180 nm with an additional parasitic Stokes order at 1240 nm behind an optical wedge and a prism. (b): Magnitude of measured transfer functions (not normalized) of the main Stokes order at 1180 nm below and above the threshold of the parasitic Stokes order.

equal to the change of the slope efficiency of the main Stokes order at the threshold of the parasitic Stokes order. This demonstrates, to the best of the author's knowledge, for the first time the passive pump-to-Stokes noise transfer suppression in a CRFL utilizing the parasitic Stokes order.

In order to investigate the influence of the cavity design parameters on the parameters of the passive noise transfer suppression, the parasitic Stokes order was included in the numerical simulation that was introduced in the previous section. As presented in Fig. 6.15, the drop of the slope efficiency of the main Stokes order and the corresponding passive

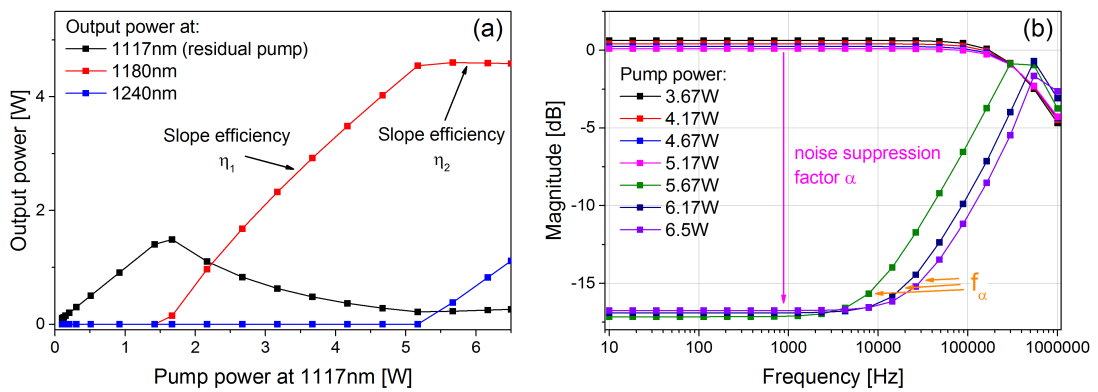


Figure 6.15: (a): Computed slope of a Raman fiber laser at 1180 nm with an additional parasitic Stokes order at 1240 nm. (b): Magnitude of computed transfer functions of the main Stokes order at 1180 nm below and above the threshold of the parasitic Stokes order.

noise transfer suppression in the transfer functions can be reproduced numerically with parameters (Raman fiber length etc.) similar to the experimental setup. As mentioned, the noise-suppression factor is obviously equal to the induced drop of the slope efficiency of the main Stokes order. Thus, it is just a matter related to the design of the cavity. However, it is very tempting to understand how to the +3 dB noise suppression cut-off frequency f_α (see Fig. 6.15 (b)) can be influenced. As a longer (shorter) Raman fiber length will lead to a longer (shorter) lifetime of all (pump, main, and parasitic Stokes order) photons, one would definitely expect a smaller (larger) cut-off frequency f_α . This is confirmed by the numerically obtained results presented in Fig. 6.16 (a) that shows f_α for three different Raman fiber lengths (25 m, 30 m and 35 m) and a reflectivity of the OC FBGs of 60 % at 1180 nm and 0.5 % at 1240 nm. Note that f_α has been determined by a fit of a high-pass to the data in the corresponding frequency domain. In addition, also the reflectivity of the OC FBG at the parasitic Stokes order has been varied for a fixed Raman fiber length of 30 m and a fixed reflectivity of the OC FBG of 60 % at 1180 nm. The corresponding results are also presented in Fig. 6.16 (a) and a smaller (larger) reflectivity leads to a larger (smaller) cut-off frequency. As presented in Fig 6.16 (b), a smaller (larger) reflectivity of the OC FBG at 1180 nm also leads to a larger (smaller) cut-off frequency. Thus, the smaller the lifetimes associated with the main and the parasitic Stokes order, the larger the noise suppression cut-off frequency f_α .

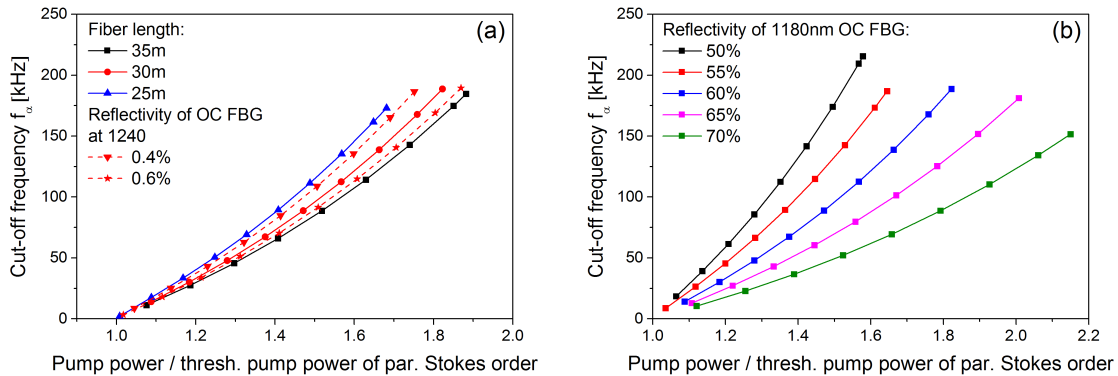


Figure 6.16: (a): Noise suppression cut-off frequency f_α in dependency of the fiber length and for a varying reflectivity of the out-coupling fiber Bragg grating of the parasitic Stokes order. (b): Noise suppression cut-off frequency f_α in dependency of the reflectivity of the out-coupling fiber Bragg grating of the main Stokes order.

Because they provide a quite interesting behavior, the numerically obtained transfer functions of the parasitic Stokes order at 1240 nm, i.e. the magnitude in the frequency range of 1 kHz - 1 MHz, are presented in Fig. 6.17 (a). Analog to the results that were

presented above, the Raman fiber length was 30 m, the reflectivity of the OC FBGs was 60 % at 1180 nm and 0.5 % at 1240 nm, and the reflectivity of both HR FBGs was 99 %. Just above the threshold of the parasitic Stokes order the transfer functions appear to be double low-passes with two distinct cut-off frequencies (class A regime), in particular good to identify for a pump power of 5.25 W (black data points). Remarkably, for further increased pump power a relaxation oscillation peak appears (class B regime), which still corresponds mathematically to a double low-pass but with complex conjugated instead of distinct real cut-off frequencies. In order to analyze this behavior in more detail either a double low-pass

$$\text{TF}(f) = \frac{A}{(f_{\text{eff},1} + if)(f_{\text{eff},2} + if)} \quad (6.15)$$

with two distinct real cut-off frequencies $f_{\text{eff},1}$ and $f_{\text{eff},2}$ or a double low-pass with complex conjugated cut-off frequencies

$$\text{TF}(f) = \frac{A}{(f_{\text{real}} + if_{\text{imag}} + if)(f_{\text{real}} - if_{\text{imag}} + if)} \quad (6.16)$$

was fitted to the data. As the quality of each fit relied significantly on the chosen model, it was used as an indicator which model should be applied to the data. The results of this analysis, i.e. the frequencies $f_{\text{eff},1}$, $f_{\text{eff},2}$, f_{real} , and f_{imag} , are presented in Fig. 6.17 (b). Indeed, just above the threshold the transfer functions are given by double low-passes and with increasing pump power the frequencies $f_{\text{eff},1}$ and $f_{\text{eff},2}$ approach each other. When both cut-off frequencies have the same value, the transition from the double low-pass

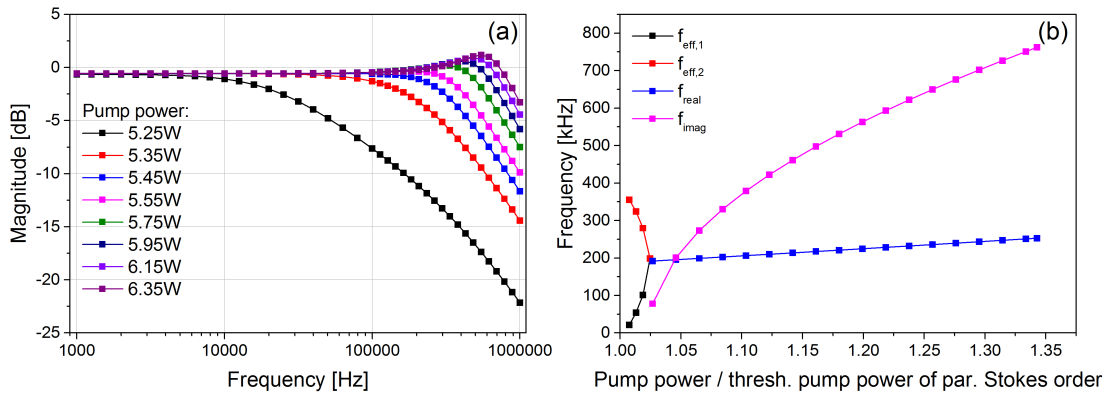


Figure 6.17: (a): Magnitude of numerically obtained transfer functions of the parasitic Stokes order at 1240 nm. (b): Corresponding cut-off frequencies (see text for further explanation).

(class A) regime to the relaxation oscillation (class B) regime occurs. For further increased pump power, the transfer functions are then given by double low-passes with complex conjugated cut-off frequencies. Unfortunately, such a behavior could not be observed in the experiments, mainly due to the maximum available modulation frequency of 100 kHz. However, the origin of this behavior can be understood again by making analogies to the model of a *conventional* laser, as it was already successfully used in the previous section. In a *conventional* laser a similar behavior is possible if the lifetime of the photons in the cavity is shorter but not too short compared to the lifetime of the inversion. Then, the transition can be driven by tuning the pump power, i.e. by controlling how far the laser is operated above the threshold. For semiconductor lasers, the reverse transition from the class B to the class A regime has already been observed, but only by changing the cavity length externally [Bai09]. For the case of a CRFL with an additional parasitic Stokes order, the averaged intra-cavity power of the main Stokes order is constant above the threshold of the parasitic Stokes order. Thus, similar to the 1117 nm pump power in the analysis of the 1180 nm Raman fiber laser in the previous section, it plays the role of the inversion. Due to the reflectivities of the utilized FBGs it is reasonable to assume that the lifetime of the averaged intra-cavity power of the parasitic Stokes order ($R_{\text{OC FBG}} = 0.5\%$) is indeed shorter but not too short in comparison to the lifetime of the averaged intra-cavity power of the main Stokes order ($R_{\text{OC FBG}} = 60\%$). Under this assumption, the observed transition from the double low-pass regime to the relaxation oscillation regime can be understood.

So far, the presented numerical and experimental results were dedicated to single-stage Raman fiber lasers at 1180 nm with an additional parasitic Stokes order at 1240 nm. As mentioned at the beginning of this chapter, CRFLs at 1480 nm are of particular interest in the context of next-generation GWDs as they are promising pump sources for Er^{3+} -doped fiber amplifiers at 1.5 μm . In addition, the pump-to-signal noise transfer in Er^{3+} -doped fiber amplifiers is given by a low-pass with a cut-off frequency in the range of 1 - 10 kHz [Nov02b]. As this is also the frequency domain up to which the noise transfer could be suppressed in the simulations and experiments presented above, it is quite intriguing to analyze if the passive pump-to-Stokes noise transfer suppression can also be applied for CRFLs at 1480 nm. If so, they could act as low-noise pump sources for Er^{3+} -doped fiber amplifiers that would also provide a low initial noise level. In particular the necessary power stabilization in GWDs would benefit from such low-noise laser sources because they lower the requirements on the corresponding control loops. Therefore, an advanced numerical simulation was used to investigate a CRFL at 1480 nm with an additional parasitic Stokes order at 1580 nm. The fiber length was 80 m, the reflectivity of all HR FBGs was 99% and the reflectivity of the OC FBGs was 20% at 1480 nm and 0.5% at 1580 nm. The corresponding results are

presented in Fig. 6.18. Indeed, above the threshold of the parasitic Stokes order the slope of the main Stokes order at 1480 nm flattens and the corresponding passive pump-to-Stokes noise transfer suppression up to frequencies in the order of some tens of kilohertz is present in the magnitude of the simulated transfer functions. Thus, instead of suppressing the parasitic Stokes order at 1580 nm in CRFLs at 1480 nm, it should be actively used to achieve a passive pump-to-Stokes noise transfer suppression because such lasers can act as a pump sources for low-noise Er³⁺-doped fiber amplifiers.

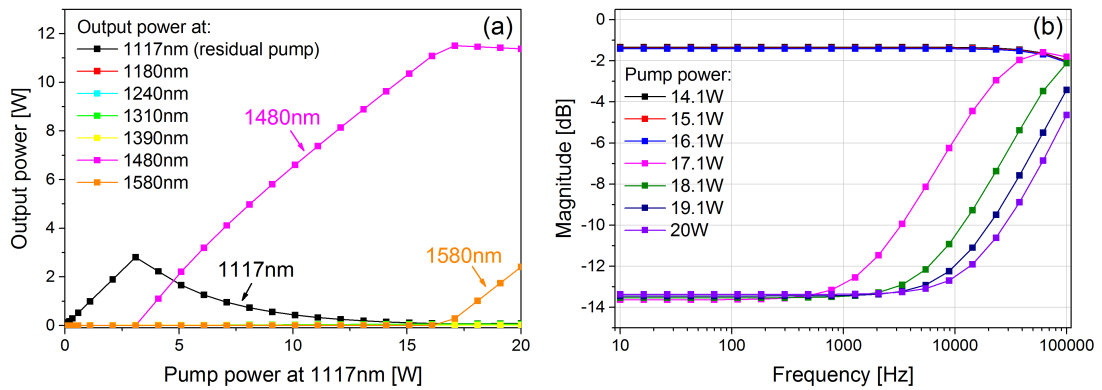


Figure 6.18: (a): Simulated slope of a cascaded Raman fiber laser at 1480 nm with an additional parasitic Stokes order at 1580 nm. (b): Magnitude of simulated transfer functions of the main Stokes order at 1480 nm below and above the threshold of the parasitic Stokes order.

6.2.3 Conclusion

The gain dynamics of single-stage Raman fiber lasers in the frequency range of 10 Hz - 1 MHz have been analyzed theoretically and experimentally for the first time. As a full analytical solution does not exist, the time-dependent PDE set describing a Raman fiber laser was Fourier-transformed and the corresponding boundary value problem was solved numerically by an appropriate solver. Numerically and experimentally obtained transfer functions of an exemplary Raman fiber laser at 1180 nm, which was pumped at 1117 nm, provide good qualitative agreement. By drawing some analogies to *conventional* lasers, i.e. lasers utilizing an atomic or molecular inversion, the simple low-pass behavior of the transfer functions can be understood and the influence of the cavity design parameters on the cut-off frequency has been analyzed with the numerical simulation.

By utilizing the parasitic Stokes order, the slope of a Raman fiber laser can become nearly insensitive to pump power fluctuations above the threshold of the parasitic Stokes order. Therefore, a corresponding passive pump-to-Stokes noise transfer suppression is achieved. A first experimental proof-of-principle of this approach was demonstrated in the

frame of this thesis with an exemplary Raman fiber laser at 1180 nm and an additional parasitic Stokes order at 1240 nm. In addition, the influence of the cavity design parameters on the suppression factor and the noise suppression cut-off frequency has been analyzed with the numerical simulation.

An advanced numerical simulation predicts that the passive pump-to-Stokes noise transfer suppression scheme can also be applied in a CRFL at 1480 nm with an additional Stokes order at around 1580 nm. Such a laser could act as a low-noise pump source for an Er^{3+} -doped single-frequency fiber amplifier in next-generation GWDs. As the Er^{3+} -doped fiber amplifier would also provide a low initial power noise level, the necessary power stabilization would benefit from this approach.

CHAPTER 7

Conclusion

Most probably, a new substrate material, i.e. crystalline silicon, in combination with laser sources at 1.5 μm will be used in the next generation of interferometric gravitational wave detectors (GWDs) to increase the sensitivity by a corresponding reduction of thermal noise. As fiber amplifiers in master oscillator power amplifier (MOPA) configuration are promising candidates to fulfill the special requirements of GWDs such as high output power levels and a good beam quality, i.e. a high TEM_{00} mode content, some important aspects of single-frequency fiber amplifiers at 1.5 μm have been investigated in the frame of this thesis.

So far, $\text{Er}^{3+}:\text{Yb}^{3+}$ -codoped large mode-area (LMA) fibers with core diameters larger than 20 μm were lacking either a good beam quality or a sufficient power handling capability, e.g. because of thermal failures at high output power levels. In the frame of this thesis it has been shown that a novel $\text{Er}^{3+}:\text{Yb}^{3+}$ -codoped triple-clad LMA fiber provides not only a comparably high TEM_{00} mode content of more than 90 % but also a large fiber core diameter of around 23 μm , which leads to a decreased threshold of stimulated Brillouin scattering (SBS). In recent years it has been shown by others that the co-seeding approach is a viable method to suppress the excessive generation of Yb^{3+} -amplified spontaneous emission (ASE) and corresponding parasitic processes at 1.0 μm in $\text{Er}^{3+}:\text{Yb}^{3+}$ -codoped fiber amplifiers. In the experiments performed for this thesis it has been proven that this method can also be applied at output power levels of more than 10 W as the maximum output power of a co-seeded single-frequency fiber amplifier based on the novel triple-clad LMA $\text{Er}^{3+}:\text{Yb}^{3+}$ -codoped fiber has been scaled to more than 60 W. As the power scaling was only limited by thermal misalignments of the co-seed in-coupling, the $\text{Er}^{3+}:\text{Yb}^{3+}$ -codoped triple-clad LMA fiber provides some good prospects for even higher output power levels in combination with a good beam quality.

The output power of the laser source in a GWD has to be delivered to the actual

interferometer, e.g. by a passive delivery fiber. Such a fiber must maintain an excellent beam quality and should not be prone to SBS. Novel LMA fiber designs with built-in suppression techniques for the higher order modes, e.g. leakage channel fibers (LCFs), promise single-mode operation and large mode field diameters. Therefore, the TEM_{00} mode content of the output beam profile of a passive LCF with a core diameter of around $50\ \mu\text{m}$ has been measured at $1.0\ \mu\text{m}$ and $1.5\ \mu\text{m}$ for the first time. The tested sample provided an excellent TEM_{00} mode content of more than 97.5% at both wavelengths, although it was sensitive to misalignments at $1.5\ \mu\text{m}$. However, as the fiber was originally designed to work at $1050\ \text{nm}$, the performance at $1.5\ \mu\text{m}$ can be certainly improved by an optimized fiber design. Thus, the LCF concept is a promising candidate for passive delivery fibers in GWDs.

Commonly, the TEM_{00} mode content of potential laser sources for GWDs is measured with a non-confocal scanning ring cavity. Numerically obtained data for the guided modes of the mentioned LCF have been used in a corresponding numerical simulation to analyze how the TEM_{00} mode content of beam profiles that contain higher order modes can be determined consistently. It has been shown that the overlap of such a beam profile with a fixed TEM_{00} mode varies with time if the phase difference between the fiber modes is not constant. However, the TEM_{00} mode content is independent of the differential phase if a TEM mode reference set is chosen that provides the highest possible TEM_{00} mode overlap with the fundamental fiber mode. These results must be considered carefully when the TEM_{00} overlap of few-mode fibers supporting higher order modes is determined experimentally by a non-confocal scanning ring cavity.

State of the art and novel power stabilization techniques in GWDs require and benefit from a detailed knowledge of how pump and seed power noise couples to the output signal via the inversion of the laser. The gain dynamics of Yb^{3+} - and Er^{3+} -doped fiber amplifiers were already studied by others. Within the frame of this thesis, the analysis has been extended to $\text{Er}^{3+}:\text{Yb}^{3+}$ -codoped fiber amplifiers. As a complete analytical solution of the problem does not exist, a numerical simulation was developed that allowed to study the transfer-functions of an exemplary $\text{Er}^{3+}:\text{Yb}^{3+}$ -codoped fiber amplifier. The results show quite good qualitative agreement with corresponding experimentally obtained results, i.e. the seed-to-signal transfer function behaves like a damped high-pass and the pump-to-signal transfer function behaves like a double low-pass. However, these results are not universal because the transfer function of the Yb^{3+} -to- Er^{3+} energy transfer depends on the actual amplifier configuration, e.g. it can not be approximated in all cases as a low-pass in case of a pump power modulation. Therefore and in contrast to Yb^{3+} - and Er^{3+} -doped fiber amplifiers, it is not possible to predict the noise transfer at high output power levels, e.g. by an extrapolation from lower output power levels. However, in particular the presented

numerical simulation can be further optimized and will certainly help to predict the noise transfer in $\text{Er}^{3+}:\text{Yb}^{3+}$ -codoped fiber amplifiers at different output power levels.

Advanced coherent beam combining schemes utilize a differential pump power control to stabilize the optical phase difference between the individual amplifiers. As such an approach requires a detailed knowledge of how pump power fluctuations couple to the signal phase via temperature effects or the Kramers–Kronig relation (KKR), the pump power modulation induced refractive index changes in an exemplary $\text{Er}^{3+}:\text{Yb}^{3+}$ -codoped fiber amplifier have been analyzed between 1 Hz and 100 kHz for the first time with a fiber-based Mach-Zehnder interferometer. Unfortunately, a final interpretation of the obtained results is not possible as it remains unclear which thermal effects and which energy states (via the KKR) contribute to the refractive index changes.

Er^{3+} -doped fiber amplifiers that are core-pumped at 1480 nm provide some promising features, e.g. a high absorption per unit length, regarding a possible application in GWDs. In recent years it has been shown that cascaded Raman fiber lasers (CRFLs) at 1480 nm are compact single-mode lasers with output power levels of some hundreds of watts. However, the power scaling is hindered by several detrimental effects and a few of them have been investigated in the frame of this thesis. Numerical results indicate that a hybrid CRFL and Raman fiber amplifier approach is suitable to avoid the common onset of lasing at the parasitic Stokes order, even if a standard fiber without an increased loss at the parasitic Stokes order is used. In addition, the Raman conversion stage should be pumped at 1117 nm as a pump laser at 1064 nm leads to a feedback of the Raman conversion stage at around 1117 nm that drastically affects the efficiency of the pump laser. Furthermore, only fiber Bragg gratings (FBGs) that were loaded during the fabrication with deuterium should be used because the common hydrogenation with molecular hydrogen leads to a strong absorption at the 1240 nm Stokes order that induces thermal drifts of the FBGs. All these results will certainly support the power scaling of CRFLs at 1480 nm in the future.

It has been shown experimentally in this thesis for the first time that the onset of lasing at the parasitic Stokes order in an exemplary CRFL at 1180 nm and 1240 nm leads to a passive pump-to-Stokes noise transfer suppression. The influence of the cavity design parameters on the suppression factor and the noise suppression cut-off frequency was studied with an appropriate numerical simulation. Furthermore, an advanced numerical simulation predicts that the passive pump-to-Stokes noise transfer suppression scheme can also be applied in a CRFL at 1480 nm with an additional Stokes order at around 1580 nm. Such a laser could act as a low-noise pump source for Er^{3+} -doped single-frequency fiber amplifiers in next-generation GWDs. As the Er^{3+} -doped fiber amplifiers would also provide a low initial power noise level, the necessary power stabilization would benefit from this approach.

CHAPTER 8

Outlook

As argued throughout this thesis and supported by the presented results, Er^{3+} -doped and $\text{Er}^{3+}:\text{Yb}^{3+}$ -codoped fiber amplifiers in MOPA configuration are promising candidates as laser sources at $1.5\ \mu\text{m}$ for the next generation of GWDs. However, several important and interesting topics remain to be thoroughly investigated in the future and some of them are listed in the following.

As the novel triple-clad LMA $\text{Er}^{3+}:\text{Yb}^{3+}$ -codoped fiber from INO provided an excellent performance and as the power scaling was only limited by thermal misalignments of the co-seed in-coupling, an improved experimental setup, e.g. an advanced mounting of the fiber, might allow for even higher output power levels in combination with a fairly good TEM_{00} mode content. Although INO also fabricated a matching passive fiber, it relied on the double-clad design and could not be spliced with tolerable losses to the active triple-clad fiber, most probably because of the additional GeO_2 - and P_2O_5 -doped pedestal of the active fiber that has a quite different melting temperature. However, if a matching fiber would be available that can be spliced with low losses to the active fiber, it could be used for example to fabricate an all-fiber pump-combiner that would allow for a spatially separated pump and co-seed in-coupling. Furthermore, the actual co-seed might be unnecessary if it would be possible to imprint a pair of FBGs in the active triple-clad fiber, so that corresponding stable lasing at around $1.0\ \mu\text{m}$ suppresses any excessive generation of Yb^{3+} -ASE. Just recently it has been shown that this approach is very promising, in particular for high-power configurations with free-space in-couplings [Han15].

Indeed, there are more promising all-solid LMA fiber designs with built-in filtering techniques for the higher order modes, e.g. chirally-coupled-core fibers, photonic bandgap fibers, and LCFs. Unfortunately, corresponding active fibers have been fabricated essentially so far only for applications at $1.0\ \mu\text{m}$ and $2.0\ \mu\text{m}$, i.e. they were doped with Yb^{3+} or Tm^{3+} .

However, if the fiber manufacturers can be encouraged to develop corresponding Er^{3+} -doped or $\text{Er}^{3+}:\text{Yb}^{3+}$ -codoped fibers, it will be highly interesting to analyze these fibers, in particular with respect to a possible application in next-generation GWDs.

As shown, the gain dynamics of $\text{Er}^{3+}:\text{Yb}^{3+}$ -codoped fiber amplifiers are quite complex and it is not possible to predict the noise transfer at high output power levels, e.g. by an extrapolation from lower output power levels. However, further systematic investigations will help to understand if the transfer function of the energy transfer in case of a pump power modulation can for example be approximated above certain output power levels as a simple low-pass. In addition, the presented numerical simulation can be further optimized in the future and will certainly help to predict the noise transfer in $\text{Er}^{3+}:\text{Yb}^{3+}$ -codoped fiber amplifier at different output power levels, in particular if all parameters (cross-sections, energy transfer rate etc.) are well known. Indeed, the energy transfer rate is certainly different for different fibers and it is highly questionable if the only experimentally obtained formula that links the doping concentrations and the energy transfer rate is reliable. Thus, further investigations of this subject are highly demanded. In addition, the common modeling of the energy transfer process as a simple rate in the rate equations is not correct as the underlying physical process is a dipole-dipole interaction. It might be interesting to adopt a stochastic model for the homogeneous up-conversion in Er^{3+} -doped fibers for the Yb^{3+} -to- Er^{3+} energy transfer, in particular as it models the interaction reasonably as a dipole-dipole interaction [Ser00; Ser07].

Further experimental investigations of the pump power modulation induced refractive index changes in Er^{3+} -doped and $\text{Er}^{3+}:\text{Yb}^{3+}$ -codoped fiber amplifiers will help to understand and separate the individual contributions of the involved processes. For example, the thermally-induced refractive index changes in an exemplary Er^{3+} -doped fiber amplifier should be investigated, in order to check if the heating is also decoupled from the energy states like in Yb^{3+} -doped fiber amplifiers or if other mechanism, e.g. the significant up-conversion in Er^{3+} -doped fibers, lead to different transfer functions. Furthermore, the same experimental investigation should be performed with an exemplary $\text{Er}^{3+}:\text{Yb}^{3+}$ -codoped fiber that is pumped at 1480 nm, for example by a CRFL. Such an experiment will certainly help to understand which effects related to the Er^{3+} -ions in $\text{Er}^{3+}:\text{Yb}^{3+}$ -codoped fiber amplifiers contribute to the total phase shift and to distinguish these effects from additional effects if pumped at 976 nm, which are related basically to the Yb^{3+} -codoping and the energy transfer processes.

A lot of interesting topics remain to be investigated in the context of high-power CRFLs at 1480 nm. In particular the hybrid CRFL and amplifier approach provides great prospects for even higher output power levels than they are reported in the literature. In addition,

optimization techniques of this scheme are highly required. Indeed, the numerical simulation developed in the frame of this thesis can be further optimized and used to obtain some design rules for hybrid Raman fiber laser and amplifier setups. In addition, it will be highly interesting to use a high-power CRFL at 1480 nm as a pump source for an all-fiber single-frequency Er^{3+} -doped fiber amplifier and to investigate the actual limitations of such a configuration.

Regarding the passive pump-to-Stokes noise transfer suppression a lot of challenging work remains to be performed in the future. Indeed, the obvious next step will be to implement the passive pump-to-Stokes noise transfer suppression in a CRFL at 1480 nm with an additional Stokes order at around 1580 nm. It will be highly interesting to see if the cavity can be designed and optimized such that the parasitic Stokes order just starts to lase slightly below the maximum pump power as only then the maximum output power at 1480 nm is just slightly reduced. Then, the 1480 nm CRFL should be used to pump an Er^{3+} -doped fiber amplifier and the relative intensity noise (RIN) of the amplifier should be measured with and without the passive noise suppression. Indeed, although it is very likely that the passive noise suppression will actually lead to a reduction of the RIN of the Er^{3+} -doped fiber amplifier, other noise sources such as variations in the spectrum of the pump laser, i.e. spectral pump noise, or time-dependent misalignments of free-space fiber in-couplings might dominate and need to be eliminated first.

So far, all investigations of single-frequency Er^{3+} -doped and $\text{Er}^{3+}:\text{Yb}^{3+}$ -codoped fiber amplifiers with respect to next-generation GWDs were performed with optical fibers based on fused silica. However, other glass materials provide a much higher solubility of Er^{3+} (and other rare-earth ions) without the detrimental clustering. In particular Er^{3+} -doped and $\text{Er}^{3+}:\text{Yb}^{3+}$ -codoped phosphate glasses and fibers have been studied extensively, because they allow for high gain levels per unit length and short cavities [Hu01; Jia03; Sen05]. Even an $\text{Er}^{3+}:\text{Yb}^{3+}$ -codoped phosphate all-solid single-mode photonic crystal fiber (PCF) has been demonstrated [Wan14]. Indeed, in comparison with silica fibers, phosphate fibers suffer from a lower mechanical stability and splicing phosphate to silica fibers is very challenging since they exhibit quite different melting temperatures. However, recently it has been shown that fibers consisting of an $\text{Er}^{3+}:\text{Yb}^{3+}$ -codoped phosphate core and a silica cladding overcome these drawbacks [Ego14]. Nevertheless, a lot of challenges regarding Er^{3+} -doped and $\text{Er}^{3+}:\text{Yb}^{3+}$ -codoped phosphate fibers remain, but it might be worth to investigate their suitability as active fibers in single-frequency fiber amplifiers at 1.5 μm for next-generation GWDs.

Bibliography

- [Aas15] J. Aasi et al., “Advanced LIGO”, *Class. Quantum Grav.* **32** (7), 2015.
- [Abe11] M. Abernathy et al., “Einstein gravitational wave telescope conceptual design study”, *European Gravitational Observatory Document ET-0106A-10*, 2011.
- [Ace15] F. Acernese et al., “Advanced Virgo: a second-generation interferometric gravitational wave detector”, *Class. Quantum Grav.* **32** (2), 2015.
- [Agr01] G. P. Agrawal, *Nonlinear Fiber Optics*, 3rd edition, Academic Press Inc., 2001.
- [Ain91] B. J. Ainslie, “A review of the fabrication and properties of Erbium-doped fibers for optical amplifiers”, *J. Lightwave Technol.* **9** (2), 1991, pp. 220–227.
- [Ark98] J. Arkwright, P. Elango, G. Atkins, T. Whitbread, and M. Dignonnet, “Experimental and theoretical analysis of the resonant nonlinearity in Ytterbium-doped fiber”, *J. Lightwave Technol.* **16** (5), 1998, pp. 798–806.
- [Aso13] Y. Aso, Y. Michimura, K. Somiya, M. Ando, O. Miyakawa, T. Sekiguchi, D. Tatsumi, and H. Yamamoto, “Interferometer design of the KAGRA gravitational wave detector”, *Phys. Rev. D* **88** (4), 2013, p. 043007.
- [Bab07] S. A. Babin, D. V. Churkin, A. E. Ismagulov, S. I. Kablukov, and E. V. Podivilov, “Four-wave-mixing-induced turbulent spectral broadening in a long Raman fiber laser”, *J. Opt. Soc. Am. B* **24** (8), 2007, pp. 1729–1738.
- [Bai09] G. Baili, M. Alouini, T. Malherbe, D. Dolfi, I. Sagnes, and F. Bretenaker, “Direct observation of the class-B to class-A transition in the dynamical behavior of a semiconductor laser”, *Europhys. Lett.* **87** (4), 2009, p. 44005.
- [Bal14] J. Ballato and P. Dragic, “Materials development for next generation optical fiber”, *Materials* **2014** (7), 2014, pp. 4411–4430.
- [Bar12] R. A. Barankov, K. Wei, B. Samson, and S. Ramachandran, “Resonant bend loss in leakage channel fibers”, *Opt. Lett.* **37** (15), 2012, pp. 3147–3149.

- [Bas12] C. Basu, P. Weßels, J. Neumann, and D. Kracht, “High power single frequency solid state master oscillator power amplifier for gravitational wave detection”, *Opt. Lett.* **37** (14), 2012, pp. 2862–2864.
- [Bec99] P. C. Becker, N. A. Olsson, and J. R. Simpson, *Erbium-Doped Fiber Amplifiers: Fundamentals and Technology*, Elsevier Science & Technology, 1999.
- [Ber14] M. Bernier, V. Fortin, M. El-Amraoui, Y. Messaddeq, and R. Vallée, “3.77 μm fiber laser based on cascaded Raman gain in a chalcogenide glass fiber”, *Opt. Lett.* **39** (7), 2014, pp. 2052–2055.
- [Boy03] R. W. Boyd, *Nonlinear Optics*, Second Edition, Academic Press Inc., 2003.
- [Buc04] J. A. Buck, *Fundamentals of Optical Fibers*, Wiley - Interscience, 2nd edition, 2004.
- [Bur04] B. Burgoyne, N. Godbout, and S. Lacroix, “Transient regime in a n th-order cascaded CW Raman fiber laser”, *Opt. Express* **12** (6), 2004, pp. 1019–1024.
- [Bur05a] B. Burgoyne, N. Godbout, and S. Lacroix, “Theoretical analysis of n th-order cascaded continuous-wave Raman fiber lasers. I. Model and resolution”, *J. Opt. Soc. Am. B* **22** (4), 2005, pp. 764–771.
- [Bur05b] B. Burgoyne, N. Godbout, and S. Lacroix, “Theoretical analysis of n th-order cascaded continuous-wave Raman fiber lasers. II. Optimization and design rules”, *J. Opt. Soc. Am. B* **22** (4), 2005, pp. 772–776.
- [Can06] G. Canat, Y. Jaouën, and J. C. Mollier, “Performance and limitations of high brightness Er^{3+} - Yb^{3+} fiber sources”, *Comptes Rendus Physique* **7** (2), 2006, pp. 177–186.
- [Can07] G. Canat, L. Lombard, S. Jetschke, S. Unger, J. Kirchhof, H.-R. Müller, A. Durécu, V. Jolivet, and P. Bourdon, “Er-Yb-doped LMA fiber structures for high energy amplification of narrow linewidth pulses at 1.5 μm ”, *CLEO 2007*, OSA Technical Digest Series (CD), paper CTuBB1, 2007.
- [Des02] E. Desurvire, D. Bayart, B. Desthieux, and S. Bigo, *Erbium-Doped Fiber Amplifiers, Device and System Developments*, Lavoisier, 2002.
- [Dig97] M. Digonnet, R. Sadowski, H. Shaw, and R. Pantell, “Experimental evidence for strong UV transition contribution in the resonant nonlinearity of doped fibers”, *J. Lightwave Technol.* **15** (2), 1997, pp. 299–303.

- [Don09a] L. Dong, H. A. McKay, A. Marcinkevicius, L. Fu, J. Li, B. K. Thomas, and M. E. Fermann, “Extending effective area of fundamental mode in optical fibers”, *J. Lightwave Technol.* **27** (11), 2009, pp. 1565–1570.
- [Don07] L. Dong, X. Peng, and J. Li, “Leakage channel optical fibers with large effective area”, *J. Opt. Soc. Am. B* **24** (8), 2007, pp. 1689–1697.
- [Don09b] L. Dong, T. W. Wu, H. A. McKay, L. Fu, J. Li, and H. G. Winful, “All-glass large-core leakage channel fibers”, *IEEE J. Sel. Top. Quantum Electron.* **15** (1), 2009, pp. 47–53.
- [Dro10] M. Drolet, P. Laperle, C. Paré, H. Zheng, L. Desbiens, A. Proulx, and Y. Taillon, “High-power fiber amplifier using a depressed-clad Yb-doped LMA fiber with low photodarkening”, *Proc. SPIE 7750, Photonics North 2010*, 2010, pp. 7750181–7750188.
- [Ego14] O. N. Egorova, S. L. Semjonov, V. V. Velmiskin, Y. P. Yatsenko, S. E. Sverchkov, B. I. Galagan, B. I. Denker, and E. M. Dianov, “Phosphate-core silica-clad Er/Yb-doped optical fiber and cladding pumped laser”, *Opt. Express* **22** (7), 2014, pp. 7632–7637.
- [Ehr10] T. Ehrenreich, R. Leveille, I. Majid, K. Tankala, G. Rines, and P. F. Moulton, “1-kW, all-glass Tm: fiber laser”, *Fiber Lasers VII: Technology, Systems, and Applications*, 2010.
- [Emo07] Y. Emori, K. Tanaka, C. Headley, and A. Fujisaki, “High-power cascaded Raman fiber laser with 41-W output power at 1480-nm band”, *CLEO 2007*, OSA Technical Digest Series (CD), paper CFI2, 2007.
- [Fed95] M. Federighi and F. DiPasquale, “The effect of pair-induced energy transfer on the performance of silica waveguide amplifiers with high Er³⁺/Yb³⁺ concentrations”, *IEEE Photon. Technol. Lett.* **7** (3), 1995, pp. 303–305.
- [For12] V. Fortin, M. Bernier, D. Faucher, J. Carrier, and R. Vallée, “3.7 W fluoride glass Raman fiber laser operating at 2231 nm”, *Opt. Express* **20** (17), 2012, pp. 19412–19419.
- [Fot08] A. Fotiadi, O. Antipov, and P. Mégret, “Dynamics of pump-induced refractive index changes in single-mode Yb-doped optical fibers”, *Opt. Express* **16** (17), 2008, pp. 12658–12663.

- [Fot09] A. Fotiadi, N. Zakharov, O. Antipov, and P. Mégret, “All-fiber coherent combining of Er-doped amplifiers through refractive index control in Yb-doped fibers”, *Opt. Lett.* **34** (22), 2009, pp. 3574–3576.
- [Fre07] M. Frede, B. Schulz, R. Wilhelm, P. Kwee, F. Seifert, B. Willke, and D. Kracht, “Fundamental mode, single-frequency laser amplifier for gravitational wave detectors”, *Opt. Express* **15** (2), 2007, pp. 459–465.
- [Gal04] A. Galvanauskas, “High power fiber lasers”, *Optics and Photonics News* **15** (7), 2004, pp. 42–47.
- [Goo09] G. D. Goodno, L. D. Book, and J. E. Rothenberg, “Low phase noise, single frequency single mode 608 W thulium fiber amplifier”, *Opt. Lett.* **34** (8), 2009, pp. 1204–1206.
- [Gu14] G. Gu, *private communication*, 2014.
- [Gu13] G. Gu, F. Kong, T. W. Hawkins, P. Foy, K. Wei, B. Samson, and L. Dong, “Impact of fiber outer boundaries on leaky mode losses in leakage channel fibers”, *Opt. Express* **21** (20), 2013, pp. 24039–24048.
- [Guy09] J. E. Guyer, D. Wheeler, and J. A. Warren, “FiPy: partial differential equations with Python”, *Comput. Sci. Eng.* **11** (3), 2009, pp. 6–15.
- [Hag07] J. Hagen, R. Engelbrecht, O. Welzel, A. Siekiera, and B. Schmauss, “Numerical modeling of intracavity spectral broadening of Raman fiber lasers”, *IEEE Photon. Technol. Lett.* **19** (21), 2007, pp. 1759–1761.
- [Han15] Q. Han, Y. Yao, Y. Chen, F. Liu, T. Liu, and H. Xiao, “Highly efficient Er/Yb-codoped fiber amplifier with an Yb-band fiber Bragg grating”, *Opt. Lett.* **40** (11), 2015, pp. 2634–2636.
- [Han11] Q. Han, Y. He, Z. Sheng, W. Zhang, J. Ning, and H. Xiao, “Numerical characterization of Yb-signal-aided cladding-pumped Er:Yb-codoped fiber amplifiers”, *Opt. Lett.* **36** (9), 2011, pp. 1599–1601.
- [Han10] Q. Han, J. Ning, and S. Zhaoxia, “Numerical investigation of the ASE and power scaling of cladding-pumped Er-Yb codoped fiber amplifiers”, *IEEE J. Quant. Electron.* **46** (11), 2010, pp. 1535–1541.
- [Hem14] A. Hemming, N. Simakov, A. Davidson, S. Bennetts, M. Hughes, N. Carmody, P. Davies, L. Corena, D. Stepanov, J. Haub, R. Swain, and A. Carter, “A monolithic cladding pumped holmium-doped fiber laser”, *CLEO 2014*, OSA Technical Digest (online), paper CW1M.1, 2014.

- [Hin09] G. Hinshaw et al., “Five-year wilkinson microwave anisotropy probe observations: data processing, sky maps, and basic results”, *The Astrophysical Journal Supplement* **180** (2), 2009, pp. 225–245.
- [Hor97] N. Horowitz, A. R. Chraplyvy, R. W. Tkach, and J. L. Zyskind, “Broadband transmitted intensity noise induced by Stokes and anti-Stokes Brillouin scattering in single-mode fibers”, *IEEE Photon. Technol. Lett.* **9** (1), 1997, pp. 124–126.
- [Hu01] Y. Hu, S. Jiang, T. Luo, K. Seneschal, M. Morrell, F. Smektala, S. Honkanen, J. Lucas, and N. Peyghambarian, “Performance of high-concentration Er^{3+} - Yb^{3+} -codoped phosphate fiber amplifiers”, *IEEE Photon. Technol. Lett.* **13** (7), 2001, pp. 657–659.
- [Jac04] S. D. Jackson, “Cross relaxation and energy transfer upconversion processes relevant to the functioning of $2\ \mu\text{m}$ Tm^{3+} -doped silica fibre lasers”, *Opt. Commun.* **230** (1), 2004, pp. 197–203.
- [Jac01] S. D. Jackson and P. H. Muir, “Theory and numerical simulation of nth-order cascaded Raman fiber lasers”, *J. Opt. Soc. Am. B* **18** (9), 2001, pp. 1297–1306.
- [Jas09] J. C. Jasapara, M. J. Andrejco, A. DeSantolo, A. D. Yablon, Z. Várallyay, J. W. Nicholson, J. M. Fini, D. J. DiGiovanni, C. Headley, E. Monberg, and F. V. DiMarcello, “Diffraction-limited fundamental mode operation of core-pumped very-large-mode-area Er fiber amplifiers”, *IEEE J. Quant. Electron.* **15** (1), 2009, pp. 3–11.
- [Jau11] C. Jauregui, T. Eidam, J. Limpert, and A. Tünnermann, “Impact of modal interference on the beam quality of high-power fiber amplifiers”, *Opt. Express* **19** (4), 2011, pp. 3258–3271.
- [Jeb14] M. A. Jebali, J. N. Maran, and S. LaRochelle, “264 W output power at 1585 nm in Er-Yb codoped fiber laser using in-band pumping”, *Opt. Lett.* **39** (13), 2014, pp. 3974–3977.
- [Jeo05] Y. Jeong, J. K. Sahu, D. B. S. Soh, C. A. Codemard, and J. Nilsson, “High-power tunable single-frequency single-mode Erbium:Ytterbium codoped large-core fiber master-oscillator power amplifier source”, *Opt. Lett.* **30** (22), 2005, pp. 2997–2999.

- [Jeo07] Y. Jeong, S. Yoo, C. Codemard, J. Nilsson, J. Sahu, D. Payne, R. Horley, P. Turner, L. Hickey, A. Harker, M. Lovelady, and A. Piper., “Erbium:Ytterbium codoped large-core fiber laser with 297-W continuous-wave output power”, *IEEE J. Sel. Top. Quantum Electron.* **13** (3), 2007, pp. 573–579.
- [Jia03] S. Jiang, “Erbium-doped phosphate fiber amplifiers”, *Proc. SPIE 5246, Active and Passive Optical Components for WDM Communications III*, 2003.
- [Jol13] C. Jollivet, K. Wei, B. Samson, and A. Schulzgen, “Low-loss, single-mode propagation in large-mode-area leakage channel fiber from 1 to 2 μm ”, *CLEO 2013*, OSA Technical Digest (online), paper CM3I.4, 2013.
- [Kar97] M. Karásek, “Optimum design of Er^{3+} - Yb^{3+} codoped fibers for large-signal high-pump-power applications”, *IEEE J. Quant. Electron.* **33** (10), 1997, pp. 1699–1705.
- [Kar13a] M. Karow, “ TEM_{00} mode power scaling in specialty fibers”, PhD thesis, Gottfried Wilhelm Leibniz Universität Hannover, 2013.
- [Kar12a] M. Karow, C. Basu, D. Kracht, J. Neumann, and P. Weßels, “ TEM_{00} mode content of a two stage single-frequency Yb-doped PCF MOPA with 246 W of output power”, *Opt. Express* **20** (5), 2012, pp. 5319–5324.
- [Kar12b] M. Karow, J. Neumann, D. Kracht, and P. Weßels, “ TEM_{00} mode content measurements on a large core passive CCC fiber”, *5th EPS-QEOD Europhoton Conference on Solid-State, Fiber and Waveguide Coherent Light Sources*, paper TuP.27, 2012.
- [Kar13b] M. Karow, C. Zhu, D. Kracht, J. Neumann, A. Galvanauskas, and P. Weßels, “Fundamental gaussian mode content measurements on active large core CCC fibers”, *CLEO/Europe-EQEC 2013*, OSA Technical Digest (online), paper CJ_1_6, 2013.
- [Kar00] V. I. Karpov, W. R. Clements, E. M. Dianov, and S. B. Papernyi, “High-power 1.48 μm phosphoro-silicate-fiber-based laser pumped by laser diodes”, *Can. J. Phys.* **78** (5), 2000, pp. 407–413.
- [Kaw74] S. Kawakami and S. Nishida, “Characteristics of a doubly clad optical fiber with a low-index inner cladding”, *IEEE J. Quant. Electron.* **10** (12), 1974, pp. 879–887.

- [Kir15] N. V. Kiritchenko, L. V. Kotov, M. A. Melkumov, M. E. Likhachev, M. M. Bubnov, M. V. Yashkov, A. Y. Laptev, and A. N. Guryanov, “Effect of Ytterbium co-doping on Erbium clustering in silica-doped glass”, *Laser Phys.* **25** (2), 2015.
- [Kni96] J. C. Knight, T. A. Birks, P. S. J. Russell, and D. M. Atkin, “All-silica single-mode optical fiber with photonic crystal cladding”, *Opt. Lett.* **21** (19), 1996, pp. 1547–1549.
- [Kon13] F. Kong, G. Gu, T. W. Hawkins, J. Parsons, M. Jones, C. Dunn, M. T. Kalichevsky-Dong, K. Wei, B. Samson, and L. Dong, “Flat-top mode from a 50 μm -core Yb-doped leakage channel fiber”, *Opt. Express* **21** (26), 2013, pp. 32371–32376.
- [Kop00] J. P. Koplrow, D. A. V. Kliner, and L. Goldberg, “Single-mode operation of a coiled multimode fiber amplifier”, *Opt. Lett.* **25** (7), 2000, pp. 442–444.
- [Kot13] L. V. Kotov, M. E. Likhachev, M. M. Bubnov, O. I. Medvedkov, M. V. Yashkov, A. N. Guryanov, J. Lhermite, S. Février, and E. Cormier, “75 W 40 % efficiency single-mode all-fiber Erbium-doped laser cladding pumped at 976 nm”, *Opt. Lett.* **38** (13), 2013, pp. 2230–2232.
- [Kou02] D. Kouznetsov and J. V. Moloney, “Efficiency of pump absorption in doubleclad fiber amplifiers. II. Broken circular symmetry”, *J. Opt. Soc. Am. B* **19** (6), 2002, pp. 1259–1263.
- [Kou01] D. Kouznetsov, J. V. Moloney, and E. Wright, “Efficiency of pump absorption in double-clad fiber amplifiers. I. Fiber with circular symmetry”, *J. Opt. Soc. Am. B* **18** (6), 2001, pp. 743–749.
- [Kra06] M. Krause, S. Cierullies, H. Renner, and E. Brinkmeyer, “Pump-to-Stokes RIN transfer in Raman fiber lasers and its impact on the performance of co-pumped Raman amplifiers”, *Opt. Commun.* **260** (2), 2006, pp. 656–661.
- [Kra10] L. M. Krauss, S. Dodelson, and S. Meyer, “Primordial gravitational waves and cosmology”, *Science* **328** (5981), 2010, pp. 989–992.
- [Kro26] R. Kronig, “On the theory of dispersion of X-rays”, *Journal of the Optical Society of America and Review of Scientific Instruments* **12** (6), 1926, pp. 547–557.

- [Kub14] I. Kubat, C. R. Petersen, U. V. Møller, A. Seddon, T. Benson, L. Brilland, D. Méchin, P. M. Moselund, and O. Bang, “Thulium pumped mid-infrared 0.9–9 μm supercontinuum generation in concatenated fluoride and chalcogenide glass fibers”, *Opt. Express* **22** (4), 2014, pp. 3959–3967.
- [Kuh10a] V. Kuhn, D. Kracht, J. Neumann, and P. Weßels, “Dependence of Er:Yb-codoped 1.5 μm amplifier on wavelength-tuned auxiliary seed signal at 1 μm wavelength”, *Opt. Lett.* **35** (24), 2010, pp. 4105–4107.
- [Kuh11a] V. Kuhn, D. Kracht, J. Neumann, and P. Weßels, “67 W of output power from an Yb-free Er-doped fiber amplifier cladding pumped at 976 nm”, *IEEE Photon. Technol. Lett.* **23** (7), 2011, pp. 432–434.
- [Kuh11b] V. Kuhn, D. Kracht, J. Neumann, and P. Weßels, “Er-doped photonic crystal fiber amplifier with 70 W of output power”, *Opt. Lett.* **36** (16), 2011, pp. 3030–3032.
- [Kuh11c] V. Kuhn, D. Kracht, J. Neumann, and P. Weßels, “Yb-free Er-doped 980 nm pumped single-frequency fiber amplifier with output power of 54 W and near-diffraction limited beam quality”, *CLEO/Europe-EQEC 2011*, OSA Technical Digest (CD), paper CJ7_5., 2011.
- [Kuh10b] V. Kuhn, S. Unger, S. Jetschke, D. Kracht, J. Neumann, J. Kirchhof, and P. Weßels, “Experimental comparison of fundamental mode content in Er:Yb-codoped LMA fibers with multifilament- and pedestal-design cores”, *J. Light-wave Technol.* **28** (22), 2010, pp. 3212–3219.
- [Kuh09] V. Kuhn, P. Weßels, J. Neumann, and D. Kracht, “Stabilization and power scaling of cladding pumped Er:Yb-codoped fiber amplifier via auxiliary signal at 1064 nm”, *Opt. Express* **17** (20), 2009, pp. 18304–18311.
- [Kwe12] P. Kwee, C. Bogan, K. Danzmann, M. Frede, H. Kim, P. King, J. Poeld, O. Puncken, R. Savage, F. Seifert, P. Weßels, L. Winkelmann, and B. Willke, “Stabilized high-power laser system for the gravitational wave detector advanced LIGO”, *Opt. Express* **20** (10), 2012, pp. 10617–10634.
- [Kwe07] P. Kwee, F. Seifert, B. Willke, and K. Danzmann, “Laser beam quality and pointing measurement with an optical resonator”, *Rev. Sci. Instrum.* **78**, 2007, p. 073103.
- [Lab80] P. Labudde, H. P. Weber, and R. H. Stolen, “Bandwidth reduction in CW fiber Raman lasers”, *IEEE J. Quant. Electron.* **16** (2), 1980, pp. 115–117.

- [Lap07] P. Laperle, C. Paré, H. Zheng, and A. Croteau, “Yb-doped LMA triple-clad fiber for power amplifiers”, *Proc. SPIE 6453, Fiber Lasers IV: Technology, Systems, and Applications*, 2007.
- [Lap09] M. A. Lapointe, S. Chatigny, M. Piché, M. Cain-Skaff, and J. N. Maran, “Thermal effects in high-power CW fiber lasers”, *Proc. SPIE 7195, Fiber Lasers VI: Technology, Systems, and Applications*, 2009.
- [Lay77] C. B. Layne, W. H. Lowdermilk, and M. J. Weber, “Multiphonon relaxation of rare-earth ions in oxide glasses”, *Phys. Rev. B* **16** (10), 1977, pp. 10–17.
- [LIG13] "LIGO scientific collaboration", *Instrument science white paper*, tech. rep., 2013.
- [Lim12] E. Lim, S. Alam, and D. J. Richardson, “Optimizing the pumping configuration for the power scaling of in-band pumped Erbium doped fiber amplifiers”, *Opt. Express* **20** (13), 2012, pp. 13886–13895.
- [Lim05] J. Limpert, N. Deguil-Robin, I. Manek-Hoenninger, F. Salin, F. Roeser, A. Liem, T. Schreiber, S. Nolte, H. Zellmer, A. Tünnermann, J. Broeng, A. Petersson, and C. Jakobsen, “High-power rod-type photonic crystal fiber laser”, *Opt. Express* **13** (4), 2005, pp. 1055–1058.
- [Lim04] J. Limpert, A. Liem, M. Reich, T. Schreiber, S. Nolte, H. Zellmer, A. Tünnermann, J. Broeng, A. Petersson, and C. Jakobsen, “Low-nonlinearity single-transverse-mode Ytterbium-doped photonic crystal fiber amplifier”, *Opt. Express* **12** (7), 2004, pp. 1313–1319.
- [Liu14] J. Liu, H. Shi, K. Liu, Y. Hou, and P. Wang, “210 W single-frequency, single-polarization, thulium-doped all-fiber MOPA”, *Opt. Express* **22** (11), 2014, pp. 13572–13578.
- [Ma11] X. Ma, C. Liu, G. Chang, and A. Galvanauskas, “Angular-momentum coupled optical waves in chirally-coupled-core fibers”, *Opt. Express* **19** (27), 2011, pp. 26515–26528.
- [Mar91] D. Marcuse, *Theory of Dielectric Optical Waveguides*, Academic Press Inc., 1991.
- [Mar11] H. Martins, M. B. Marques, and O. Frazao, “300 km-ultralong Raman fiber lasers using a distributed mirror for sensing applications”, *Opt. Express* **19** (19), 2011, pp. 18149–18154.
- [Min91] W. Miniscalco, “Erbium-doped glasses for fiber amplifiers at 1500 nm”, *J. Lightwave Technol.* **19** (2), 1991, pp. 234–250.

- [Miy79] T. Miya, Y. Terunuma, T. Hosaka, and T. Miyashita, “Ultimate low-loss single mode fibre at 1.55 μm ”, *Electron. Lett.* **15** (4), 1979, pp. 106–108.
- [Mor07] B. Morasse, S. Agger, S. Chatigny, E. Gagnon, J. P. de Sandro, and C. Poulsen, “10 W ASE-free single mode high power double cladding Er^{3+} - Yb^{3+} amplifier”, *Proc. SPIE 6453, Fiber Lasers IV: Technology, Systems, and Applications*, 2007.
- [Mys97] P. Myslinski, D. Nguyen, and J. Chrostowski, “Effects of concentration on the performance of Erbium-doped fiber amplifiers”, *J. Lightwave Technol.* **15** (1), 1997, pp. 112–120.
- [Nag82] S. Nagel, J. B. MacChesney, and K. Walker, “An overview of the modified chemical vapor deposition (MCVD) process and performance”, *IEEE J. Quant. Electron.* **18** (4), 1982, pp. 459–476.
- [Nic12] J. W. Nicholson, J. M. Fini, A. M. DeSantolo, X. Liu, K. Feder, P. S. Westbrook, V. R. Supradeepa, E. Monberg, F. DiMarcello, R. Ortiz, C. Headley, and D. J. DiGiovanni, “Scaling the effective area of higher-order-mode Erbium-doped fiber amplifiers”, *Opt. Express* **20** (22), 2012, pp. 24575–24584.
- [Nic08] J. W. Nicholson, A. D. Yablon, S. Ramachandran, and S. Ghalmi, “Spatially and spectrally resolved imaging of modal content in large-mode-area fibers”, *Opt. Express* **16** (10), 2008, pp. 7233–7243.
- [Nog85] K. Noguchi, N. Shibata, N. Uesugi, and Y. Negishi, “Loss increase for optical fibers exposed to hydrogen atmosphere”, *J. Lightwave Technol.* **3** (2), 1985, pp. 236–243.
- [Nov02a] S. Novak and R. Gieske, “SIMULINK model for EDFA dynamics applied to gain modulation”, *J. Lightwave Technol.* **20** (6), 2002, pp. 986–992.
- [Nov02b] S. Novak and A. Moesle, “Analytic model for gain modulation in EDFAs”, *J. Lightwave Technol.* **20** (2), 2002, pp. 975–985.
- [Oth99] A. Othonos and K. Kalli, *Fiber Bragg Gratings*, Artech House, Inc., 1999.
- [Ouy14] D. Ouyang, C. Guo, S. Ruan, P. Yan, H. Wei, and J. Luo, “Yb band parasitic lasing suppression in Er/Yb-co-doped pulsed fiber amplifier based on all-solid photonic bandgap fiber”, *Appl. Phys. B* **114**, 2014, pp. 585–590.
- [Po89] H. Po, E. Snitzer, R. Tumminelli, L. Zenteno, F. Hakimi, N. M. Cho, and T. Haw, “Double clad high brightness Nd fiber laser pumped by GaAlAs phased array”, *Optical Fiber Communication Conference*, Vol. 5 of 1989 OSA Technical Digest Series, paper PD7, 1989.

- [Pun10] M. Punturo et al., “The third generation of gravitational wave observatories and their science reach”, *Class. Quantum Grav.* **27**, 2010, p. 084007.
- [Rap10] P. Rapagnani, “Gravitational wave detectors on the earth”, *Class. Quantum Grav.* **27**, 2010, p. 194001.
- [Rob14] C. Robin, I. Dajani, B. Pulford, and C. Vergien, “Single-frequency Yb-doped photonic crystal fiber amplifier with 800 W output power”, *Proc. SPIE 8961, Fiber Lasers XI: Technology, Systems, and Applications*, 2014.
- [Sal12] J. Salvatier, *scikits.bvp_solver 1.1*, 2012, URL: https://pypi.python.org/pypi/scikits.bvp%5C_solver.
- [Sch04] A. Schlatter, S. C. Zeller, R. Grange, R. Paschotta, and U. Keller, “Pulse-energy dynamics of passively mode-locked solid state lasers above the Q-switching threshold”, *J. Opt. Soc. Am. B* **21** (8), 2004, pp. 1469–1478.
- [Sch99] B. F. Schutz, “Gravitational wave astronomy”, *Class. Quantum Grav.* **16** (12A), 1999, A131–A156.
- [Sef04] G. A. Sefler, W. D. Mack, G. C. Valley, and T. S. Rose, “Secondary energy transfer and nonparticipatory Yb³⁺ ions in Er³⁺-Yb³⁺ high-power amplifier fibers”, *J. Opt. Soc. Am. B* **21** (10), 2004, pp. 1740–1748.
- [Sen05] K. Seneschal, F. Smektala, B. Bureau, M. LeFloch, S. Jiang, T. Luo, J. Lucas, and N. Peyghambarian, “Properties and structure of high Erbium doped phosphate glass for short optical fibers amplifiers”, *Materials Research Bulletin* **40** (9), 2005, pp. 1433–1442.
- [Ser00] S. V. Sergeyev and B. Jaskorzynska, “Statistical model for energy-transfer-induced up-conversion in Er³⁺-doped glasses”, *Phys. Rev. B* **62** (23), 2000, pp. 15628–15633.
- [Ser07] S. V. Sergeyev and S. Popov, “Excitation back transfer in a statistical model for upconversion in Er-doped fibres”, *Journal of the European Optical Society: Rapid Publications* **2**, 2007, pp. 070271–070276.
- [Sha06] L. F. Shampine, P. H. Muir, and H. Xu, “A user-friendly Fortran BVP solver”, *SIAM J. Numer. Anal.* **1** (2), 2006, pp. 201–217.
- [Shi08] A. Shirakawa, H. Suzuki, M. Tanisho, and K. Ueda, “Yb-ASE-free Er amplification in short-wavelength filtered Er:Yb photonic-crystal fiber”, *Conference on Optical Fiber communication/National Fiber Optic Engineers Conference (OFC/NFOEC)*, paper OThN2, 2008.

- [Sie86] A. E. Siegman, *Lasers*, University Science Books, 1986.
- [Sli13] D. Sliwinska, P. Kaczmarek, G. Sobon, and K. M. Abramski, “Double-seeding of Er/Yb co-doped fiber amplifiers for controlling of Yb-ASE”, *J. Lightwave Technol.* **31** (21), 2013, pp. 3381–3386.
- [Sni65] E. Snitzer and R. Woodcock, “Yb³⁺-Er³⁺ glass laser”, *Appl. Phys. Lett.* **6** (3), 1965, pp. 45–46.
- [Sob14] G. Sobon, D. Sliwinska, K. M. Abramski, and P. Kaczmarek, “10 W single-mode Er/Yb co-doped all-fiber amplifier with suppressed Yb-ASE”, *Laser Physics Letters* **11** (2), 2014, p. 025103.
- [Sob12a] G. Sobon, P. Kaczmarek, and K. M. Abramski, “Erbium-Ytterbium co-doped fiber amplifier operating at 1550 nm with stimulated lasing at 1064 nm”, *Opt. Commun.* **285** (7), 2012, pp. 1929–1933.
- [Sob11] G. Sobon, P. Kaczmarek, A. Antonczak, J. Sotor, and K. M. Abramski, “Controlling the 1 μ m spontaneous emission in Er/Yb co-doped fiber amplifiers”, *Opt. Express* **19** (20), 2011, pp. 19104–19113.
- [Sob12b] G. Sobon, D. Sliwinska, P. Kaczmarek, and K. M. Abramski, “Er/Yb co-doped fiber amplifier with wavelength-tuned Yb-band ring resonator”, *Opt. Commun.* **285** (18), 2012, pp. 3816–3819.
- [Ste14] M. Steinke, A. Croteau, C. Paré, H. Zheng, P. Laperle, A. Proulx, J. Neumann, D. Kracht, and P. Weßels, “Co-seeded Er³⁺:Yb³⁺ single frequency fiber amplifier with 60 W output power and over 90 % TEM₀₀ content”, *Opt. Express* **22** (14), 2014, pp. 16722–16730.
- [Ste15a] M. Steinke, J. Neumann, D. Kracht, and P. Weßels, “Gain dynamics in Er³⁺:Yb³⁺ co-doped fiber amplifiers”, *Opt. Express* **23** (11), 2015, pp. 14946–14959.
- [Ste15b] M. Steinke, J. Neumann, D. Kracht, and P. Weßels, “Gain dynamics in Raman fiber lasers and passive pump-to-Stokes RIN suppression”, *Opt. Express* **23** (13), 2015, pp. 16823–16837.
- [Ste15c] M. Steinke, H. Tünnermann, J. Neumann, D. Kracht, B. Samson, G. Gu, L. Dong, and P. Weßels, “TEM₀₀ mode content measurements on a passive leakage channel fiber”, *Opt. Lett.* **40** (3), 2015, pp. 383–386.
- [Sti09] E. Stiles, “New developments in IPG fiber laser technology”, *Proceedings of the 5th International Workshop on Fiber Lasers*, 2009.

- [Sun08a] G. Sun, D. Hwang, and Y. Chung, “Stabilization of the output power from a Raman fiber laser by generated-amplified spontaneous emission”, *Laser Phys.* **18** (10), 2008, pp. 1188–1191.
- [Sun08b] G. Sun, A. Lin, D. Hwang, W.-T. Han, and Y. Chung, “Gain-clamped discrete Raman amplifier with suppressed low-frequency relative intensity noise pump-to-signal transfer”, *Laser Phys.* **18** (10), 2008, pp. 1192–1195.
- [Sup12a] V. R. Supradeepa, J. W. Nicholson, and K. Feder, “Continuous wave Erbium-doped fiber laser with output power of >100 W at 1550 nm in-band core-pumped by a 1480 nm Raman fiber laser”, *CLEO 2012*, OSA Technical Digest (online), paper CM2N.8, 2012.
- [Sup13a] V. R. Supradeepa and J. W. Nicholson, “Power scaling of high-efficiency 1.5 μm cascaded Raman fiber lasers”, *Opt. Lett.* **38** (14), 2013, pp. 2538–2541.
- [Sup12b] V. R. Supradeepa, J. W. Nicholson, C. Headley, Y.-W. Lee, B. Palsdottir, and D. Jakobsen, “Cascaded Raman fiber laser at 1480 nm with output power of 104 W”, *Proc. SPIE 8237, Fiber Lasers IX: Technology, Systems, and Applications*, 2012.
- [Sup13b] V. R. Supradeepa, J. W. Nicholson, C. E. Headley, M. F. Yan, B. Palsdottir, and D. Jakobsen, “A high efficiency architecture for cascaded Raman fiber lasers”, *Opt. Express* **21** (6), 2013, pp. 7148–7155.
- [Tac98] S. Taccheo, P. Laporta, O. Svelto, and G. D. Geronimo, “Theoretical and experimental analysis of intensity noise in a codoped Erbium-Ytterbium glass laser”, *Appl. Phys. B* **66** (1), 1998, pp. 19–26.
- [Tan06a] F. Z. Tang, P. McNamara, G. W. Barton, and S. P. Ringer, “Nanoscale characterization of silica soots and aluminium solution doping in optical fibre fabrication”, *J. Non-Cryst. Solids* **352** (36), 2006, pp. 3799–3807.
- [Tan06b] K. Tankala, B. Samson, A. Carter, J. Farroni, D. Machewirth, N. Jacobson, U. Manyam, A. Sanchez, M.-Y. Cheng, A. Galvanauskas, W. Torruellas, and Y. Chen, “New developments in high power eye-safe LMA fibers”, *Proc. SPIE 6102, Fiber Lasers III: Technology, Systems, and Applications*, 2006.
- [Tar09] H. I. Tarman and H. Berberoğlu, “Efficient numerical algorithm for cascaded Raman fiber lasers using a spectral method”, *J. Lightwave Technol.* **27** (13), 2009, pp. 2289–2295.

- [Tay79] J. H. Taylor, L. A. Fowler, and P. M. McCulloch, “Measurements of general relativistic effects in the binary pulsar PSR1913+16”, *Nature* **277**, 1979, pp. 437–440.
- [The12a] T. Theeg, H. Sayinc, J. Neumann, and D. Kracht, “All-fiber counter-propagation pumped single frequency amplifier stage with 300 W output power”, *IEEE Photon. Technol. Lett.* **24** (20), 2012, pp. 1864–1867.
- [The12b] T. Theeg, H. Sayinc, J. Neumann, L. Overmeyer, and D. Kracht, “Pump and signal combiner for bi-directional pumping of all-fiber lasers and amplifiers”, *Opt. Express* **20** (27), 2012, pp. 28125–28141.
- [Tow87] J. E. Townsend, S. B. Poole, and D. N. Payne, “Solution-doping technique for fabrication of rare earth doped optical fibres”, *Electron. Lett.* **23** (7), 1987, pp. 329–331.
- [Tow91] J. Townsend, W. Barnes, K. Jedrzejewski, and S. Grubb, “Yb³⁺ sensitised Er³⁺ doped silica optical fibre with ultrahigh transfer efficiency and gain”, *Electron. Lett.* **27** (21), 1991, pp. 1958–1959.
- [Tün12a] H. Tünnermann, Y. Feng, J. Neumann, D. Kracht, and P. Weßels, “All-fiber coherent beam combining with phase stabilization via differential pump power control”, *Opt. Lett.* **37** (7), 2012, pp. 1202–1204.
- [Tün11] H. Tünnermann, J. Neumann, D. Kracht, and P. Weßels, “All-fiber phase actuator based on an Erbium-doped fiber amplifier for coherent beam combining at 1064 nm”, *Opt. Lett.* **36** (4), 2011, pp. 448–450.
- [Tün12b] H. Tünnermann, J. Neumann, D. Kracht, and P. Weßels, “Frequency resolved analysis of thermally induced refractive index changes in fiber amplifiers”, *Opt. Lett.* **37** (17), 2012, pp. 3597–3599.
- [Tün12c] H. Tünnermann, J. Neumann, D. Kracht, and P. Weßels, “Gain dynamics and refractive index changes in fiber amplifiers: a frequency domain approach”, *Opt. Express* **20** (12), 2012, pp. 13539–13550.
- [Val08] M. J. Valtonen et al., “A massive binary black-hole system in OJ 287 and a test of general relativity”, *Nature* **452**, 2008, pp. 851–853.
- [Wan14] L. Wang, D. He, S. Feng, C. Yu, L. Hu, J. Qiu, and D. Chen, “Yb/Er co-doped phosphate all-solid single-mode photonic crystal fiber”, *Scientific Reports* **4**, 2014.

- [Wan15] S. Wang, M. S. Mangir, and P. Nee, “Practical technique for improving all-fiber coherent combination of multistage high-power Ytterbium fiber amplifiers”, *Appl. Opt.* **54**, 2015, pp. 3150–3156.
- [Wei72] R. Weiss, “Electromagnetically coupled broadband gravitational antenna”, *Quarterly Progress Report, Research Laboratory of Electronics MIT*, 1972.
- [Wie07] S. Wielandy, “Implications of higher-order mode content in large mode area fibers with good beam quality”, *Opt. Express* **15** (23), 2007, pp. 15402–15409.
- [Win11] L. Winkelmann, O. Puncken, R. Kluzik, C. Veltkamp, P. Kwee, J. Poeld, C. Bogan, B. Willke, M. Frede, J. Neumann, P. Weßels, and D. Kracht, “Injection-locked single-frequency laser with an output power of 220 W”, *Appl. Phys. B* **102** (3), 2011, pp. 529–538.
- [Won05] W. S. Wong, X. Peng, J. M. McLaughlin, and L. Dong, “Breaking the limit of maximum effective area for robust single-mode propagation in optical fibers”, *Opt. Lett.* **30** (21), 2005, pp. 2855–2857.
- [Xio03] Z. Xiong, N. Moore, Z. G. Li, and G. C. Lim, “10-W Raman Fiber Lasers at 1248 nm Using Phosphosilicate Fibers”, *J. Lightwave Technol.* **21** (10), 2003, pp. 2377–381.
- [Yah03] E. Yahel and A. Hardy, “Efficiency optimization of high-power, Er^{3+} - Yb^{3+} -codoped fiber amplifiers for wavelength-division-multiplexing applications”, *J. Opt. Soc. Am. B* **20** (6), 2003, pp. 1189–1197.
- [Yus05] Y. Yusim, J. Barsalou, D. Gapontsev, N. S. Platonov, O. Shkurikhin, V. P. Gapontsev, Y. A. Barannikov, and F. Shcherbina, “100 Watt, single-mode, CW, linearly polarized all-fiber format 1.56 μm laser with suppression of parasitic lasing effects”, *Proc. SPIE 5709, Fiber Lasers II: Technology, Systems, and Applications*, 2005.
- [Zer14] M. N. Zervas and C. A. Codemard, “High power fiber lasers: a review”, *IEEE J. Sel. Top. Quantum Electron.* **20** (5), 2014.
- [Zha14a] H. Zhang, H. Xiao, P. Zhou, X. Wang, and X. Xu, “High power Yb-Raman combined nonlinear fiber amplifier”, *Opt. Express* **22** (9), 2014, pp. 10248–10255.
- [Zha11] J. Zhang, V. Fromzel, and M. Dubinskii, “Resonantly cladding-pumped Yb-free Er-doped LMA fiber laser with record high power and efficiency”, *Opt. Express* **19** (6), 2011, pp. 5574–5578.

- [Zha13] L. Zhang, S. Cui, J. Hu, L. Chen, and Y. Feng, “Power scaling of Raman fiber amplifier based source for laser guide star”, *Advanced Solid-State Lasers Congress*, OSA Technical Digest (online), paper JTh2A.38, 2013.
- [Zha14b] L. Zhang, H. Jiang, S. Cui, and Y. Feng, “Integrated Ytterbium-Raman fiber amplifier”, *Opt. Lett.* **39** (7), 2014, pp. 1933–1936.
- [Zha14c] L. Zhang, H. Jiang, S. Cui, J. Hu, L. Chen, and Y. Feng, “Over 50 W 589 nm single frequency laser by frequency doubling of single Raman fiber amplifier”, *CLEO 2014*, OSA Technical Digest (online), paper SW3N.7, 2014.
- [Zhu15] G. Zhu, L. Geng, X. Zhu, L. Li, Q. Chen, R. A. Norwood, T. Manzur, and N. Peyghambarian, “Towards ten-watt-level 3-5 μm Raman lasers using tellurite fiber”, *Opt. Express* **23** (6), 2015, pp. 7559–7573.
- [Zhu11] J. Zhu, P. Zhou, Y. Ma, X. Xu, and Z. Liu, “Power scaling analysis of tandem-pumped Yb-doped fiber lasers and amplifiers”, *Opt. Express* **19** (19), 2011, pp. 18645–18654.

Publications in Peer-Reviewed Journals

1. M. Steinke, H. Knoeckel, and E. Tiemann, “(X)1 $^1\sigma^+$ state of LiNa studied by Fourier-transform spectroscopy”, *Phys. Rev. A* **85**, 2012, p. 042720.
2. M. Steinke, A. Croteau, C. Paré, H. Zheng, P. Laperle, A. Proulx, J. Neumann, D. Kracht, and P. Weßels, “Co-seeded $\text{Er}^{3+}:\text{Yb}^{3+}$ single frequency fiber amplifier with 60 W output power and over 90 % TEM_{00} content”, *Opt. Express* **22** (14), 2014, pp. 16722–16730.
3. M. Steinke, J. Neumann, D. Kracht, and P. Weßels, “Gain dynamics in $\text{Er}^{3+}:\text{Yb}^{3+}$ co-doped fiber amplifiers”, *Opt. Express* **23** (11), 2015, pp. 14946–14959.
4. M. Steinke, J. Neumann, D. Kracht, and P. Weßels, “Gain dynamics in Raman fiber lasers and passive pump-to-Stokes RIN suppression”, *Opt. Express* **23** (13), 2015, pp. 16823–16837.
5. M. Steinke, H. Tünnermann, J. Neumann, D. Kracht, B. Samson, G. Gu, L. Dong, and P. Weßels, “ TEM_{00} mode content measurements on a passive leakage channel fiber”, *Opt. Letters* **40** (3), 2015, pp. 383–386.

Publications in Conference Proceedings

1. M. Steinke, D. Kracht, J. Neumann, and P. Weßels, “1.0 μm co-seeded Er:Yb fiber amplifier with 50 W output power at 1.5 μm ”, *Conference on Lasers and Electro-Optics (CLEO) 2013*, OSA Technical Digest (online) (Optical Society of America, 2013), paper CTu1K.7, 2013.
2. M. Steinke, E. Schreiber, D. Kracht, J. Neumann, and P. Weßels, “Development of a cascaded Raman fiber laser with 6.5W output power at 1480nm supported by detailed numerical simulations”, *Conference on Lasers and Electro-Optics (CLEO) / Europe and International Quantum Electronics Conference (EQEC) 2013*, (Optical Society of America, 2013), paper CJ_P_16, 2013.
3. M. Steinke, E. Schreiber, D. Kracht, J. Neumann, and P. Weßels, “Kaskadierter Raman-Faserlaser mit 5W Ausgangsleistung bei 1480nm”, *DPG Frühjahrstagung 2013*, paper Q57.2, 2013.
4. P. Weßels, M. Karow, V. Kuhn, M. Steinke, H. Tünnermann, D. Kracht, and J. Neumann, “Fiber Amplifiers for Gravitational Wave Detection”, *Conference on Lasers and Electro-Optics (Cleo) / Pacific Rim 2013*, (Optical Society of America, 2013), paper MA1_1, 2013.
5. P. Weßels, M. Karow, V. Kuhn, M. Steinke, H. Tünnermann, D. Kracht, and J. Neumann, “Single-Frequency Fiber Amplifiers for Gravitational Wave Detection”, *Conference on Lasers and Electro-Optics (CLEO) 2013*, OSA Technical Digest (online) (Optical Society of America, 2013), paper CW3M.5, 2013.
6. M. Steinke, D. Kracht, J. Neumann, and P. Weßels, “Gain dynamics in Er:Yb co-doped fiber amplifiers”, *Conference on Lasers and Electro-Optics (CLEO) 2014*, OSA Technical Digest (online) (Optical Society of America, 2014), paper JW2A.29, 2014.

7. M. Steinke, D. Kracht, J. Neumann, and P. Weßels, “Clustering and up-conversion effects in an $\text{Er}^{3+}:\text{Yb}^{3+}$ co-doped fused silica fibre: A comparison between experiment and models”, *Conference on Lasers and Electro-Optics (CLEO) / Europe and International Quantum Electronics Conference (EQEC) 2015*, (Optical Society of America, 2015), paper CJ-P.25, 2015.
8. M. Steinke, D. Kracht, J. Neumann, and P. Weßels, “Passive noise suppression in cascaded Raman fiber lasers”, *SPIE Photonics West 2015 - Nonlinear Frequency Generation and Conversion: Materials, Devices, and Applications XIV*, paper 9347-40, 2015.

Curriculum Vitae

Personal Data

Name Michael Steinke
Date of birth 08.03.1985
Family status married

Education

1992 - 1995 Grundschule am Castrum, Gehrden
1995 - 1998 Sophie Scholl Gesamtschule, Wennigsen
1998 - 2004 Matthias Claudius Gymnasium, Gehrden

University Education

2004 - 2011 Physics, Leibniz Universität Hannover
2011 Diploma
Title of thesis: Fourier-Transformations-Spektroskopie an NaLi und Na₂ sowie Bestimmung der Singulett-Grundzustandspotentiale
Group of Prof. Tiemann, Institut für Quantenoptik

Professional Affiliations

2012 – present Researcher
Laser development department
Solid state (formerly single-frequency) lasers group
Laser Zentrum Hannover e.V.

Acknowledgments

First of all, I am deeply thankful to Prof. Uwe Morgner for the supervision and the evaluation of this thesis. Furthermore, I'd also like to thank Prof. Karsten Danzmann for the evaluation of this thesis as a second examiner.

I acknowledge Dr. Dietmar Kracht for providing me the opportunity to carry out my research at the Laser Zentrum Hannover e.V. as the atmosphere throughout the whole institute was always very encouraging and motivating. In addition, I am very thankful to Dr. Jörg Neumann for the amendment of this thesis and my publications because his remarks increased the corresponding quality significantly. Furthermore, I'd like to thank Dr. Kracht and Dr. Neumann for giving me the opportunity to present my work at diverse scientific conferences and to represent the Laser Zentrum Hannover e.V. at the laser fair. Special thanks go to Peter Weßels for countless discussions about results, conclusions, and effects I was not aware of as well as for letting me the freedom and the time to investigate all the (stupid) things that came to my mind. Additional thanks go to the whole laser development department, in particular to Malte Karow and Henrik Tünnermann for helpful discussions and Katharina Hausmann and Christoph Ottenhues for their support with multiple fiber components.

I recognize everybody that was involved in accomplishing the promotion of the excellence cluster "Centre for Quantum Engineering and Space-Time Research". Part of the work presented in this thesis was carried out in the frame of this project. In addition, I'd like to thank André Croteau from INO for discussion about the $\text{Er}^{3+}:\text{Yb}^{3+}$ -codoped triple-clad fiber, Prof. Liang Dong from the Clemson University for providing the leakage channel fiber, Torsten Thiel from AOS for all the fiber Bragg gratings, and John Salvatier from the University of Washington for detailed discussions about boundary value problems and how to (not) solve them.

Last but not least I'd like to thank my family since we never gave up and stood together, no matter how hard the times were. Furthermore, I am very thankful to my wife Bianca for her never ending support and patience, in particular while I was writing this thesis.

